

## 6. AUTOMOTIVE METALS—CROSSCUTTING

### A. Magnesium Research and Technology Development

*Principal Investigator: Eric A. Nyberg*

*Pacific Northwest National Laboratory*

*P.O. Box 999, Richland, WA 99352*

*(509) 375-2103; fax: (509) 375-2766; e-mail: Eric.Nyberg@pnl.gov*

*Technology Area Development Manager: Joseph A. Carpenter*

*(202) 586-1022; fax: (202) 586-1600; e-mail: joseph.carpenter@ee.doe.gov*

*Field Technical Monitor: Mark T. Smith*

*(509) 375-4478; fax: (509) 375-4448; e-mail: mark.smith@pnl.gov*

---

*Contractor: Pacific Northwest National Laboratory (PNNL)*

*Contract No.: DE-AC06-76RL01830*

---

#### Objective

- Support the DOE-United States Automotive Materials Partnership (USAMP) Magnesium Front End Research and Development (MFERD) project (see report 6.C) in collaboration with China and Canada.
- Increase awareness and familiarity of magnesium (Mg) as a viable option for automotive applications.
- Compile, document and evaluate state-of-the-art research and development (R&D) in Mg research around the world as a resource to best determine where United States (U.S.) government resources should be directed.

#### Approach

- As MFERD Project Technical Committee (PTC) Cochair, provide the Project Steering Committee (PSC) member, who is the DOE Technology Area Development Manager, with relevant information as it relates to funding or significant technical developments and challenges of the MFERD project. Review the monthly U.S. MFERD Task Leaders' progress and note issues that may arise relevant to funding or DOE concern.
- Attend and evaluate both the semiannual and annual U.S. MFERD Task Leaders' review meetings and assess effectiveness of the nine U.S. tasks of the MFERD project. Attend and be cognizant of progress/issues with the associated USAMP front-end design project, Magnesium Front End Design and Development MFEDD (see report 6.B).
- Through quarterly teleconferences, collaborate with the Chinese and Canadian PTC Cochairs for the organization of the annual report and annual review meeting.
- Submit an updated report on the gaps in international research related to Mg R&D.
- Promote a consorted effort for international non-competitive Mg R&D.
- Develop and maintain the Mg R&D Bibliographic Database located at magnesium.pnl.gov.

#### Accomplishments

- **MFERD:** In fiscal year 2008, Eric Nyberg was the MFERD PTC Cochair responsible for the coordination of the quarterly PTC teleconferences, developing the agenda for the annual review and coordinating the U.S. portion of the annual report in both English/Chinese. It has been critical to maintain frequent and open

communication with PTC members in Canada and China. This has resulted in significant technical progress in a relatively short time. As a DOE-funded program, the U.S. tasks are driven by the USAMP representatives. Through monthly teleconferences, the USAMP Task Leaders were able to provide frequent updates to progress and issues. Specifically from the MFERD Cochair, activities have included the following.

- Coordinated and reviewed progress by the nine U.S. Task Leaders.
  - Participated in quarterly international conference calls with other PTC members from China and Canada.
  - Edited the 2008 U.S. and International Semi-Annual and Annual MFERD Project Reports.
  - Reviewed the U.S. Task Leaders' annual presentations held at USCAR headquarters on October 2007.
  - Established a central repository for electronic project files available to all project members.
  - Co-organized the annual Task Leaders' and PSC/PTC meeting held in Hangzhou, China.
  - Coauthored a paper with other PTC members published in the October 2008 issue of *Advanced Materials and Processes* titled "Magnesium for Future Autos: Magnesium-intensive vehicles and enabling technologies are under development through an international collaboration," which highlights a model for international collaborative success.
- Other Magnesium Research and Technology Development activities included the following.
    - Expanded the publicly available Mg bibliographic database located at [www.magnesium.pnl.gov](http://www.magnesium.pnl.gov) to over 1,700 publications and presentations on Mg R&D.
    - Served as the 2008–2009 The Minerals, Metals & Materials Society (TMS) Magnesium Committee Chairman organizing the 2009 Magnesium Technology Symposium and editing the associated technical proceeding.
    - Attended the 2008 International Materials Research Conference where Mr. Nyberg organized a meeting in Chongqing, China with over 20 leaders from the international Mg R&D community to discuss ways to increase international collaboration on basic, fundamental research of Mg in precompetitive areas.
    - Updated the 2007 research report "International Experience and Gaps in Magnesium Research and Development in the Automotive Industry."
    - Submitted a proposal for Mg composites in response to the DOE Energy Efficiency Renewable Energy research call on Nanomanufacturing for Energy Efficiency titled "Solidification processing and development of metal matrix nanocomposites fabricated by ultrasonic cavitation particle dispersion."
    - Served on the International Program Committee for the 8th International Conference on Magnesium Alloys and their Applications, Weimar, Germany, October 2009.

## Future Direction

- For the MFERD, coordinate the U.S. Year 2 annual report and evaluate Phase 1 progress. This evaluation will be used as part of the Phase 1 Gate Review to recommend when and if the second three-year phase of the project should commence.
- Develop collaboration with the U.S. Army, the National Science Foundation, and DOE on efforts for fundamental Mg R&D.
- Continue to evaluate and propose Mg R&D activities that are unique and necessary.
- Serve as the TMS Magnesium Light Metals Committee Chairman and Symposium organizer.

## Introduction

The primary purpose of this project is to support the Canada-China-U.S. collaborative project

entitled "Magnesium Front End Research and Development" (MFERD), the goal of which is to develop key enabling technologies for a

lightweight Mg front-end structure and other body applications. The MFERD project is developing enabling technologies in high-integrity casting, wrought Mg processing, Mg and dissimilar metal joining and corrosion, and in generating scientific understanding in corrosion science, crash-energy management, fatigue and noise, vibration and harshness (NVH) performance. The project also provides a platform for Mg research in collaboration with Canada, China, and the United States.

### **Background**

As mentioned above, the goal of the MFERD project is to develop key enabling technologies (body casting, extrusion, sheet and joining) and knowledge base (crashworthiness, NVH, durability and corrosion) for primary (load-path) body applications of Mg alloys. The following are some specific objectives.

- Define materials and develop manufacturing processes for Mg body castings, extrusions, sheet, and joining technologies.
- Develop knowledge base and define Mg body technical requirements in crashworthiness, NVH, durability, corrosion, and surface finishing.
- Enhance the infrastructure for integrated computational materials engineering for Mg applications, including alloy design/development, process optimization, and component manufacturing.
- Develop a total life-cycle analysis showing the net benefit of vehicle lightweighting using Mg vs energy consumption, emission, and pollution in Mg production.
- Promote high-quality professionals and students educated in materials science, engineering, and Mg R&D infrastructure in Canada, China, and the United States.
- Establish automotive original equipment manufacturer/supplier/academia collaboration in Mg body applications.

### **PNNL Approach to Supporting the MFERD Project and Database Development**

Eric Nyberg continues as the 2009 U.S. PTC Chairman as a liaison to the PSC representative at DOE. Through continued participation in all project-related meetings since the initial three-country meeting held in Dearborn, Michigan, in October 2005, a sense of continuity has developed. This enables frank and open communication with the other PTC members, especially those in China, where the professional relationship is critical to workable progress. This participation has made technical issues or cultural complexities less of a hindrance than otherwise might be. *During the annual review meeting, the PSC members expressed appreciation to the PTC and Task Leaders for work that has been completed during the project's relatively short existence.*

With the assistance of software engineers at Mississippi State University, Mr. Nyberg has developed a MFERD SharePoint website. At this site, the nonproprietary project information is collected at a central location/depository for the international task teams to access these documents easily. This type of coordination is an effort to make communication and sharing of information more efficient to all of the team members around the world.

The Mg bibliographic database was updated this year to include over 1,700 referenced papers and presentations. This database is linked at both the TMS Magnesium and the International Magnesium Association websites. This makes the database an increasingly available tool to researchers exploring state-of-the-art Mg R&D around the world.

At the 3rd International Conference on Magnesium at the June 2008 International Materials Research Conference in Chongqing, China, Mr. Nyberg organized the meeting for developing international collaboration on fundamental Mg R&D.

Highlights of the positive benefits and productive results of the three-country international MFERD

project are included in the October issue of *Advanced Materials and Processes*.

### **Current and Future Work**

For MFERD, future work will be to evaluate progress of the nine U.S. tasks, participate in Task Leader review meetings and PTC quarterly teleconferences, and report results/make recommendations to the U.S. PSC Chairman. The PTC is currently planning the 3rd Annual Task Leaders' meeting that will be held in Canada starting May 11, 2009, and will be followed by a joint PSC/PTC meeting. This will be an important review, as it is the intention of the PTC to provide a recommendation to the PSC on the future direction of the MFERD project.

Mg research opportunities inside and out of PNNL will be reviewed and proposed to DOE in consideration for future funding opportunities. In addition, we will continue to manage and update the publicly available Mg R&D Database at [www.magnesium.pnl.gov](http://www.magnesium.pnl.gov).

### **Conclusions**

This technical support project is aimed primarily at assisting the management of the U.S. portion of the three-country MFERD project. To date, the second full year of the MFERD project is nearly complete, and the annual report is being prepared for release at the annual meeting in May 2009.

Efforts continue to develop coordinated research between countries and among U.S. agencies (i.e., Army, National Science Foundation, and DOE).

### **Presentations/Publications/Patents**

1. Luo A., E. Nyberg, K. Sadayappan, and W. Shi. 2008. "Magnesium Front End Research and Development: A Canada-China-USA Collaboration," Magnesium Technology: Proceedings from the TMS 2008 Annual Meeting and Exhibition, New Orleans, Louisiana, March 9–13, pp. 3–10.
2. Nyberg E., A. Luo, K. Sadayappan, and W. Shi. 2008. "Magnesium for Future Autos: Magnesium-intensive vehicles and enabling technologies are under development through an international collaboration," *Advanced Materials and Processes*, October, pp. 35–37.
3. Nyberg, E. (PNNL), to J. Carpenter (DOE EERE), 2008. Research Report: International Experience and Gaps in Magnesium Research and Development in the Automotive Industry, Revision 1. October.

## B. Magnesium Front-End Design and Development (AMD603\*)

*Principal Investigator: Alan A. Luo*

*General Motors Research & Development Center*

*MC 480-106-212*

*30500 Mound Road*

*Warren, MI 48090-9055*

*(586) 986-8303; fax: (586) 986-9204; e-mail: alan.luo@gm.com*

*Program Technical Administrator: Robert C. McCune*

*Robert C. McCune and Associates, LLC*

*5451 S. Piccadilly Cir.*

*West Bloomfield, MI, 48322-1446*

*(248) 661-0085; fax: (248) 661-8718; robert.mccune@sbcglobal.net*

*Technology Area Development Manager: Joseph A. Carpenter*

*(202) 586-1022; fax: (202) 586-1600; e-mail: joseph.carpenter@ee.doe.gov*

*Field Project Officer: Aaron D. Yocum*

*(304) 285-4852; fax (304) 285-4403; email: aaron.yocum@netl.doe.gov*

---

*Contractor: United States Automotive Materials Partnership (USAMP)*

*Contract No.: FC26-02OR22910 through the National Energy Technology Laboratory*

---

### Objectives

- Engineering design, computer-aided analysis, and technical cost modeling of exemplary magnesium-intensive front-end structures for selected “unibody” and body-on-frame (BOF) vehicle architectures having the following design stretch targets.
  - Mass reduction target: 60% lighter than comparator steel baseline structures and 35% lighter than comparator aluminum (Al) structures for mid-size passenger car, with comparable strength and crashworthiness.
  - Vehicle mass distribution: Shift the front-to-rear mass ratio by -1/+1 toward 50/50 for the rear-wheel drive, unibody donor architecture.
  - Demonstration via technical cost modeling of a maximum of \$8/kg (of mass saved) cost penalty (100,000 vehicles/year production volumes), via part consolidation using large magnesium (Mg) castings (e.g., dash panel, shotguns) and attractive pricing of Mg in world markets.
  - Matched or improved key performance characteristics such as stiffness, durability, and NVH (noise, vibration, and harshness) of the multi-material vehicle (MMV) “donor” vehicle via simulation.

### Approach

The organizational structure of AMD603 has been described in detail in the prior progress report [1]. The project consists of two tasks: (1) Design and (2) Technical Cost Modeling. The designs are predicated on two vehicle structural archetypes: a body-frame-integral (BFI, also known as a unibody), principally used for passenger vehicles, and a BOF, which incorporates a separate (presumably steel) frame to which the body structure is attached

---

\*Denotes Project 603 of the Automotive Materials Division (AMD) of the United States Automotive Materials Partnership (USAMP), one of the formal consortia of the United States Council for Automotive Research (USCAR) set up by Chrysler, Ford, and General Motors to conduct joint, precompetitive research and development (see [www.uscar.org](http://www.uscar.org)).

in final assembly. This latter structure is used primarily for light trucks and sport-utility vehicles (SUVs). Both tasks have been commissioned to contractors with design and manufacturing data made available from the original equipment manufacturers (OEMs) as required. There are no other supplier participants.

- Task 1. Design. The design task was originally divided into stages to incorporate data being simultaneously developed with regard to materials and processes as part of AMD604 (Magnesium Front End Research and Development). The initial (Phase 1) design was intended to utilize handbook properties of materials, and such general design information as was available at the outset from the relevant OEMs. Phase 2 was intended to incorporate refinements to material properties occurring through AMD604, and Phase 3 projects designs are to be predicated on optimized properties and manufacturing methods presumably having been developed throughout the course of AMD604. The design task also incorporates computer-aided engineering (CAE) techniques to explore such features as crashworthiness, modal analysis, and durability. These critical topics are amenable to computer modeling when knowledge of deformation characteristics of the materials, including their strain-rate behaviors, cyclic deformation characteristics, and fracture are understood.
- Task 2. Technical Cost Modeling. The approach uses process-based technical cost modeling [2] to provide the following deliverables for the two front-end designs (unibody and BOF):
  - Determine primary Mg production costs and market impact of the electrolytic vs. direct thermal reduction (Pidgeon) processes.
  - Provide a detailed cost analysis and report for all the components and assembly identified by the Design Task for both the unibody and BOF designs.
  - Assessment of current steel designs for both the unibody and BOF as comparators for weight and cost.

The cost-modeling task is also divided into phases. Phase 1 includes the primary Mg production analysis and the component cost of individual parts for each design. Phase 2 includes the assembly of the components to each other and to the remainder of the body structure. Phase 2 also incorporates any updates to the front-end design determined by design changes or information gathered by AMD604. The cost analysis includes part manufacture, corrosion protection treatment, as well as any surface finishing, machining, or any other process each component requires to allow it to be attached or integrated with the rest of the front-end assembly. The overall cost of the assembly including components is provided for each design as compared to the steel baseline.

## Accomplishments

- Phase 1 Final Design Review conducted on Dec. 10, 2007. Accomplishments included initial determination of piece part designs, vehicle stiffness, bill-of-materials, mass reductions, and estimate of concept-level (i.e., lacking complete physical model) crash assessments. Ongoing design reviews (Phase 1 addenda and Phase 2) conducted during 2008.
- Phase 2 Progress: Evolving mechanical property data and manufacturing technology information have been transmitted to the Design contractor (Cosma Engineering, Troy, Michigan) by the various AMD604 U.S. Task Teams. The contractor has participated in many Task Team functions and worked with suppliers to gain firsthand knowledge useful in the design process (e.g., joining, part fabrication, and surface treatment).
- Mechanical Property Status: To date, the projected processing methods for vacuum die casting show that while the ultimate tensile strength of 220 MPa for AM60B is attainable, as is desirable elongation minimum of 6%, that the initial designs based on the anticipated yield strength of 140 MPa are not aligned with presently measured yield strength values of 125 MPa from the advanced die-casting processes. Studies are underway to determine if minor alloy modification of AM60B may permit higher yield strength to be achieved, or alternately that designs may require modification in section thickness (and concurrent mass) based on lower yield strengths actually measured.
- Cost Modeling Review: A comprehensive review of the initial component cost model was conducted by the contractor, Camanoe Associates (Cambridge, Massachusetts) as part of the yearly project review on October 21, 2008. The extractive metallurgy models are still under development; however, the models for basic part fabrication using die casting (both high-vacuum and Thixoforming processes), sheet fabrication, and extrusion were presented at that review.

- The status of specific design targets includes the following.
  - Part count reduction: 57 pieces (42 Mg front end (MFE) vs 99 steel baseline—or 58%).
  - Mass reduction: 45 kg (47%) (with equivalent global body stiffness to the steel baseline, but prior to meeting full requirements of crash, NVH, and durability performance).
  - Materials technologies: 15 castings, 3 extrusions, 15 formed Mg sheets, and 9 Al stampings.
  - Initial joining strategy developed include friction stir welding, metal inert gas (MIG) welding, self-piercing rivets (SPRs), tungsten inert gas (TIG)/laser welding, and adhesive bonding.
  - Crashworthiness: Using the latest material properties (including cracking), the crash performance of the current MFE design falls short of the steel baseline vehicle in Insurance Institute for Highway Safety (IIHS) Deformable Barrier and the New Car Assessment Program (NCAP) 35 mph full frontal impact.
  - Modal analysis: Full body, structure-only modes occur at higher frequencies than the baseline, indicating generally greater structural stiffness. However, some of the local front-end stiffness metrics and some of the engine-cradle attachment point stiffness metrics of the Mg design are currently below the baseline steel vehicle.
  - Assembly sequence has been identified for the initial design, permitting prospective plant layout and more focused cost modeling.
  - The preliminary corrosion prevention strategy is to precoat all the parts, join the parts into the front-end assembly, and further coat the entire assembly before the paint shop.
  
- Specific progress in the Technical Cost Modeling project includes the following.
  - Completed preliminary technical cost models for Thixomolding, super vacuum die casting (SVDC), extrusion, and modifications to the previously developed warm-forming model.
  - Preliminary results, based on available information, indicated that while Thixomolding and SVDC have different process parameters, the end costs are similar within the fidelity of the preliminary models.
  - Determined preliminary piece cost for Mg-designed components. This information was used to identify high-cost components which are in the process of being redesigned for alternate manufacturing technologies.
  - Determined cost-sensitive process parameters for individual technologies such as extrusion rate, lubricant type and heat-treatment requirements. Task teams are refining these numbers using manufacturing trials.
  - Developed framework for primary Mg production cost models.

## Future Direction

- Crashworthiness: Validation of CAE methods used to predict crash behavior, including use of computer codes such as LS-DYNA, is progressing via Task 1.1 in AMD604. In particular, this parallel task seeks to establish validation of crash performance of the materials and processes of interest (castings, extrusions, and sheet parts) when Mg is fabricated into a generic rail structure, viz. the “double top hat” which is amenable to both computer analysis and experimental validation. Such analysis is intended to incorporate the materials in such states as would actually be manufactured in practice (e.g., vacuum die casting). Once crashworthiness validation is completed in AMD604, the front-end design will be modified to match the crash performance of the baseline steel vehicle.
- To date, strain-rate effects for the various forms of Mg are less problematic than deformation anisotropy associated with wrought Mg materials. This material property dependence on local manufacturing directions (i.e., longitudinal direction for extrusion and rolling direction for sheet) presents a challenge for incorporating the most accurate material descriptions in the finite-element analytical methods.
- Manufacturing: While an initial build sequence has been proposed by the contractor, certain specifics such as corrosion protection surface treatment and joining methodologies have not been fully developed and included as specifics and continue to emerge from the AMD604 research and development project. This development is expected to continue throughout Phase 2.
- Cost Modeling: Conclude comparative analysis of primary production processes.

- Refinement of the process cost models and interaction between the design team and technical cost modeling team will continue to provide insight and direction to the front-end design to improve the component and assembly costs.
  - Refine manufacturing type for projected piece parts to reflect knowledge of process limitations and cost structures (e.g., sheet parts become castings; press size limitations on castings).
  - Continue to seek weight-reduction opportunities through down-gauging, part consolidation, or other means to more closely approach design stretch target.

## **Introduction**

Background for AMD603, Magnesium Front End Design and Development (MFEDD), has been provided in a prior annual progress report [1]. MFEDD is complementary to both AMD604, Magnesium Front End Research and Development, and the USAMP MMV. Whereas AMD604 is predicated on development of enabling Mg technologies via leveraging with Canadian and Chinese Mg experts on a collaborative basis, AMD603 is confined to the OEM partners of USAMP [i.e., Ford, General Motors (GM) and Chrysler] and two selected suppliers focused on design (Cosma Engineering, Troy, Michigan) and technical cost modeling (Camanoe Associates, Cambridge, Massachusetts).

The front-end structures envisioned as the objectives of the project include two structural archetypes: (1) a unibody (or BFI) structure as illustrated in Figure 1 and (2) a BOF approach as shown in Figure 2. The former structural type is associated with light passenger vehicles, whereas the latter is incorporated in light trucks and SUVs. The traditional unibody structure is assembled typically from individually stamped steel parts which are then joined together by resistance spot welding, and often incorporate adhesive bonding or “weld bonding” in combination with resistance welding for improved strength, stiffness, and performance. The attraction for use of Mg in the unibody structure arises from both weight reduction opportunity at comparable stiffness, and the prospects of combining individual piece parts into entire subassemblies, via large-scale die casting. Such large cast parts, of which present-day instrument panels and radiator supports are exemplary, have excellent dimensional properties and reduced costs over assemblies of steel stampings.

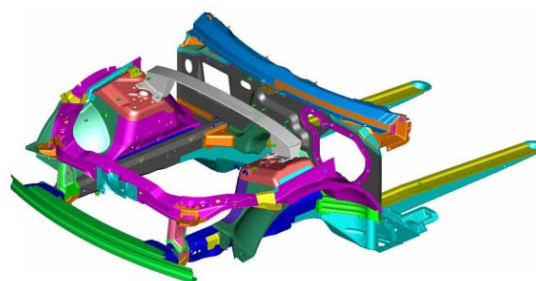


**Figure 1.** Unibody steel front-end baseline structure for the donor vehicle.

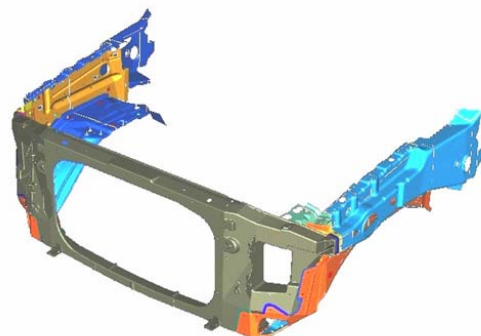


**Figure 2.** Baseline BOF donor vehicle steel structure with existing Mg radiator support.

Similarly, the baseline steel structure for the BOF donor vehicle is illustrated in Figure 2. The remainder of this report describes the status of the design exercise and generalized outcomes of the cost-modeling exercise.

## **Design Status**

The “design review” is a traditional mechanism among OEMs for presentation, analysis, and discussion of new or ongoing designs of vehicles and subsystems. The format of the design review discussions for the MFE follows the itemized agenda of Table 1.



**Table 1.** Design attributes for magnesium front end from the agenda for the design review process.

1. Design CAD – structural design to match specified envelope.
2. CAE – crash studies by LS-DYNA analysis, durability.
3. Bill of Materials – parts listing, manufacture method and drawings.
4. Mass and part count summary.
5. Vibration modal analysis and structural stiffness by CAE.
6. Frontal crash analysis for NCAP and IIHS protocols.
7. Typical cross sections of major structures and substructures.
8. Joining strategy for magnesium components.
9. Magnesium-to-steel interface strategy.
10. Manufacturing implications.
11. Assembly protocol.
12. Corrosion prevention strategy.
13. Stress/durability evaluation – static and dynamic loading of structure.

This section considers each of the major design attributes of Table 1 and provides a brief report of the status of that item. Most of the design effort in FY 2008 focused on the unibody design because of the complexity therein; however, progress was also made on the BOF, which relies more on several large-scale castings and less on part integration.

1. Computer-Aided Design. Front-end envelopes, including vehicle “hard points” and attachment points, are now implemented in physical designs and individual components for the Mg-intensive BOF and unibody designs of Figures 1 and 2. For the unibody, the original design envelope was expanded to include a multipiece Al floor pan and cowl extension brackets, also addressing item 9 regarding interfacing strategies to steel components. The unibody Mg-intensive design is indistinguishable from the baseline in terms of surfaces, cut-outs, and hard points.
2. Computer-Aided Engineering. Phase 1 material properties used for initial crash simulations and nodal analysis, and refined (Phase 2) properties incorporated in follow-on models indicating performance deficit in comparison to steel baseline (cf, item 6). Additional mass-reduction and nodal analysis studies were completed.
3. Bill of Materials. Unibody: Original design envelope extended to include floor pan and cowl extension brackets. BOF: No change.
4. Mass and Part Count. Unibody: Part count original (steel) is 99 with mass of 96.07 kg; Mg-intensive front end is 42 parts (58% reduction), and mass of 51 kg (47% reduction). BOF: 16 steel parts with mass of 70.7 kg, reduced to 3 castings with mass of 37.5 kg (81% part reduction; 47% mass reduction).
5. Vibration modal analysis and structural stiffness (Unibody). Current steel design structural modes are maintained for the entire body-in-white implemented with Mg-intensive front end. However, some of the front-end stiffness metrics and some of the engine-cradle attachment point stiffness metrics of the Mg design are currently below the baseline steel vehicle.
6. Frontal Crash (Unibody). NCAP 35 mph full frontal and IIHS deformable barrier. Initial projections using handbook mechanical properties, and absent any cracking (or material failure criteria) of the material (Phase 1), showed acceptable approximation to the baseline steel structure. However, upon incorporation of updated material properties measured in AMD604 and incorporation of the material-cracking criterion assumptions in LS-DYNA, the Mg-intensive design crash performance fell short of the baseline steel structure in both NCAP and IIHS protocols based on the current materials models and assumptions. Design updates and improvements in material properties and selection to attempt to bring the crashworthiness performance of the MFE to match that of the steel baseline are pending results from the research and development efforts in the companion project AMD604.
7. Typical Sections. All typical cross sections at various points on both structures are visible through the CAD programs and a compendium of such sections (unibody) has been generated for the design reviews.
8. Joining Strategy for Magnesium Components (Unibody). Structural adhesive bonding is called for at most joint lines, requiring metal pretreatment in advance of the assembly process and accommodation of in-place adhesive for any secondary joining processes (e.g., rivets, welds, etc.). SPRs were prescribed predominantly in Phase 1, although it appears that friction stir welds may be

utilized in some number of cases (to be determined). To date, a supplier for SPRs has not been enrolled to the AMD604 project. A more limited number of MIG or TIG fusion welds are indicated at several positions of the structure. A complete mapping of all joining processes and manufacturing scenario has been produced as a “bill of manufacture.”

9. Magnesium-to-Steel Body Interface Strategy. The bill of materials has been modified in the case of the unibody structure to permit a number of Al interface parts as isolators between the predominant MFE and the remainder of the steel unibody. Isolation through use of Al is a practice in the industry. Additionally, the design team has challenged the AMD604 Corrosion and Surface Treatment (Task 1.4) group to address the interface issue with alternatives to Al spacers such that part counts are kept low.
10. Manufacturing Implications (Unibody). Each component part has been assessed for manufacturing capability by the relevant AMD604 subteam, and recommendations were provided regarding optimal choice of process and capabilities. The BOF side support or “shotgun” structure has been the subject of a separate USAMP project on ultra-large castings and manufacturing considerations thereof. An exemplary “shotgun” structure implemented as a single Mg casting is illustrated in Figure 3.

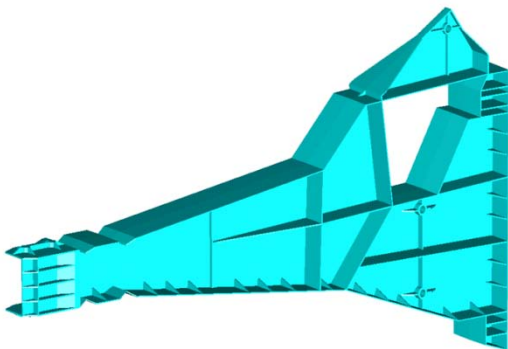


**Figure 3.** Structural Mg alloy shotgun structure designed for the Ford donor vehicle.

11. Assembly Protocol. An assembly sequence for the 42 component pieces of the unibody has been configured as part of the design and

includes relevant joining methods or any ancillary items (e.g., rivets). A hypothetical manufacturing layout has also been devised to permit factory floor plans and further cost modeling to be developed. Exemplary manufacturing cells were shown at the November 2008 design review.

12. Corrosion Prevention Strategy. The AMD604 Task 1.4 (Corrosion and Surface Treatment) team has provided much of the background for this activity. Current assumptions are based on requisite metal pretreatment for adhesive bonding and also for accommodation of any additional polymeric topcoats, either prior to or as part of the normal body and paint shop.
13. Stress/Durability Analysis (CAE). Relevant static load cases have now been provided to Cosma Engineering for the unibody structure and will become the basis for CAE analysis of applied loads to the structure.

**Cost Modeling Status**

Primary Mg Production. Figures 4 and 5 show schematizations from the literature [3] depicting the silicothermic reduction (i.e., Pidgeon) process and electrolytic extraction process respectively. Further development of the task relative to cost modeling of extraction will continue based on these process models.

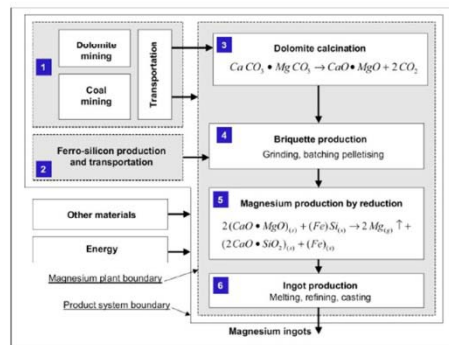


**Figure 4.** Block diagram of silicothermic reduction (Pidgeon) process after reference [3].

Magnesium Piece Part Cost Models. Each of the approximately 33 Mg pieces of the designed Mg-intensive front-end structure has been subjected to a process-based, technical cost model using one of

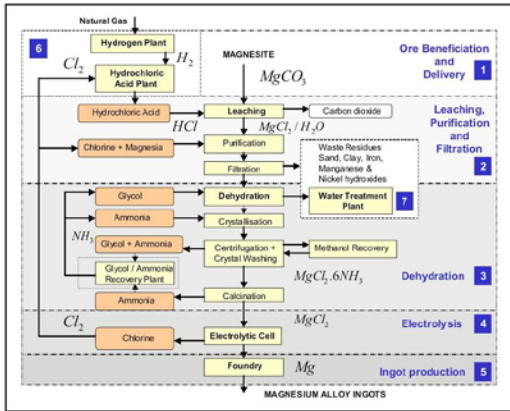


**Figure 5.** Block diagram of electrolytic extraction process for Mg after reference [3].

the candidate forming technologies (SVDC, warm sheet forming, or extrusion). Additionally, models were developed to permit comparison of SVDC and Thixomolding. A portion of the international research covered by AMD604 involves production of larger-scale parts using the Thixomolding process.

Each cost model and associated component is unique (with the exception of left- and right-hand versions of the same part), and the overall model accounts for the basic factors attributed for each aspect of the basic part fabrication, including: material, labor, equipment, tooling (unique to each part), and the category of “other,” which includes such items as energy, process-related materials (e.g., special lubricants), overhead, building costs, and maintenance.

While it is beyond the scope of this report to detail such cost models for all the componentry under consideration, Figure 6 shows an exemplary breakdown for the case of an arbitrary-shape Mg die casting.

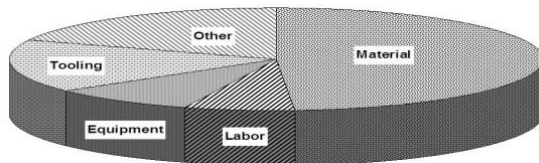


**Figure 6.** Approximate cost-element breakdown for a Mg casting of arbitrary shape.

In this particular instance, it can be seen that the cost of material represents the single largest element of the component cost. The individual models for each forming technology and each piece part are again different from each other, although several common features have begun to emerge: (1) a general tendency for the material cost to be among the largest single factors contributing to overall component cost and (2) a tendency for extrusion to show a generally lower cost of the individual forming tool, as is well-known for the comparable Al extrusion process.

It should be reiterated here that at this phase of the project, the cost models do not consider surface finishing of the as-formed part, joining, or final finish of the projected assembly.

**Conclusions**

At the end of the second fiscal year of its operation, the project has concluded a Phase 1 design based on handbook and anecdotal data and is midway through Phase 2, in which property values for the materials of consideration from the companion AMD604 project are included in the performance evaluations. The current design level must be improved and updated to have the performance of the MFE match the performance of the baseline steel vehicle. Piece-part technical cost models have been derived for SVDC, extrusion, and warm-sheet forming. The cost modeling results are influencing the design choices.

**Acknowledgments**

The success of this project is due to the dedicated efforts of team members at Chrysler, Ford, and GM, as well as the suppliers Cosma Engineering and Camanoe Associates. David Wagner of Ford, Theresa Lee of GM, and Steve Logan of Chrysler are specifically acknowledged for their significant contributions and tireless efforts. The continuing support of our respective organizations and the U.S. Department of Energy is gratefully acknowledged.

**References**

1. A. Luo, R. C. McCune, J. A. Carpenter, A. D. Yocum, and P. S. Sklad, “AMD603

- Magnesium Front End Design and Development,” FY 2007 Progress Report to DOE, (2008).
2. R. Kirchain and F. R. Field III, “Process-Based Cost Modeling: Understanding the Economics of Technical Decisions,” *Encyclopedia of Materials Science and Engineering* (2001).
  3. S. Ramakrishnan and P. Koltun, “A Comparison of the Greenhouse Impacts of Magnesium Produced by Electrolytic and Pidgeon Processes,” pp. 173-178, in A. A. Luo, et al , eds., *Magnesium Technology 2004*, TMS, Warrendale, Pennsylvania (2005).

## C. Magnesium Front End Research and Development (AMD604<sup>\*</sup>)

*Principal Investigator: Alan A. Luo*

*General Motors Research & Development Center*

*MC 480-106-212*

*30500 Mound Road*

*Warren, MI 48090-9055*

*(586) 986-8303; fax: (586) 986-9204; e-mail: alan.luo@gm.com*

*Program Technical Administrator: Robert C. McCune*

*Robert C. McCune and Associates, LLC*

*5451 S. Piccadilly Circle*

*West Bloomfield, MI, 48322-1446*

*(248) 661-0085; fax: (248) 661-8718; e-mail: robert.mccune@sbcglobal.net*

*Technology Area Development Manager: Joseph A. Carpenter*

*(202) 586-1022; fax: (202) 586-6100; e-mail: joseph.carpenter@ee.doe.gov*

*Field Project Officer: Aaron D. Yocum*

*(304) 285-4852; fax (304) 285-4403; email: aaron.yocum@netl.doe.gov*

---

*Contractor: United States Automotive Materials Partnership (USAMP)*

*Contract No.: DE-FC05-02OR22910 through the National Energy Technology Laboratory*

---

### Objective

- The concurrent development of key enabling materials and manufacturing technologies and the accompanying performance knowledge base to permit design and implementation of magnesium- (Mg-) intensive automotive-body front-end structures having greatly reduced mass, but with performance and cost comparable to sheet-steel baseline structures. Figure 1 illustrates an exemplary baseline unibody front-end structure implemented in sheet steel, which then serves as the design envelope for the proposed Mg-intensive structure. A second vehicle structure using a “body-on-frame” archetype of many light trucks is also under consideration by the project. The following two aspects of this project are unique within USAMP.
  - The focus is on entire front-end structures as the developmental object, in contrast to individual components, thereby offering critical vehicle-level benefits in terms of mass distribution and performance while challenging the technical community to devise materials and manufacturing approaches to permit mass production of such structures at reasonable cost.
  - Implementation of an international effort enlisting the best scientific and engineering expertise in Mg technology from the United States, Canada, and China in a first-of-its-kind, global collaboration.

### Approach

- Organization and Administration: Establishment of organizational and technical steering committees and systematic management of information and activities in a global environment including web-based platforms.
- Partitioning of Projects: Separation of the design function into a separate USAMP project (AMD603) as well as Integrated Computational Materials Engineering—ICME (AMD702 and 703)—to facilitate handling of original

---

<sup>\*</sup>Denotes Project 604 of the Automotive Materials Division (AMD) of the United States Automotive Materials Partnership, one of the formal consortia of the United States Council for Automotive Research set up by Chrysler, Ford, and General Motors to conduct joint, precompetitive research and development (see [www.uscar.org](http://www.uscar.org)).

equipment manufacturer- (OEM-) sensitive design data and to permit a broader, more universal approach to ICME. The international project, additionally, has a task for life-cycle analysis, in which USAMP is not participating.

- **Enabling Technologies:** Assessment of the state-of-the-art and development of emerging technologies in primary forming, joining, and finishing that would permit the manufacture of the envisioned structures.
- **Knowledge Base:** Understand the current awareness and knowledge gaps with regard to materials and structural performance in the intended application, particularly with regard to crashworthiness, noise-vibration harshness (NVH), fatigue, and durability (including corrosion).
- **Technical Gateways:** Provide for rigorous assessment of progress against pre-determined metrics at sub-levels of the project assuring that functional targets are achieved or, alternatively, that further efforts are discontinued if required metrics cannot be achieved. Gateways exist for both the design stage and also for the enabling technologies, such that efforts for an envisioned prototype build (Phase 2) only occur upon successful accomplishment of Phase 1. Overall timing and conceptual flow for projects AMD603 and AMD604 are illustrated in Figure 2, which also illustrates the positioning of the ICME project AMD703.

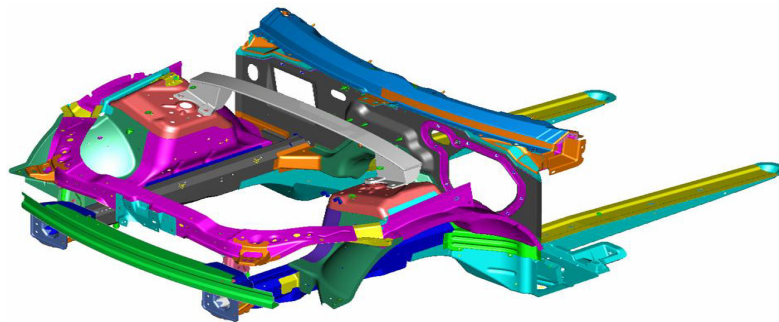


**Figure 1.** Exemplary unibody front-end design envelope as presently implemented in sheet steel.

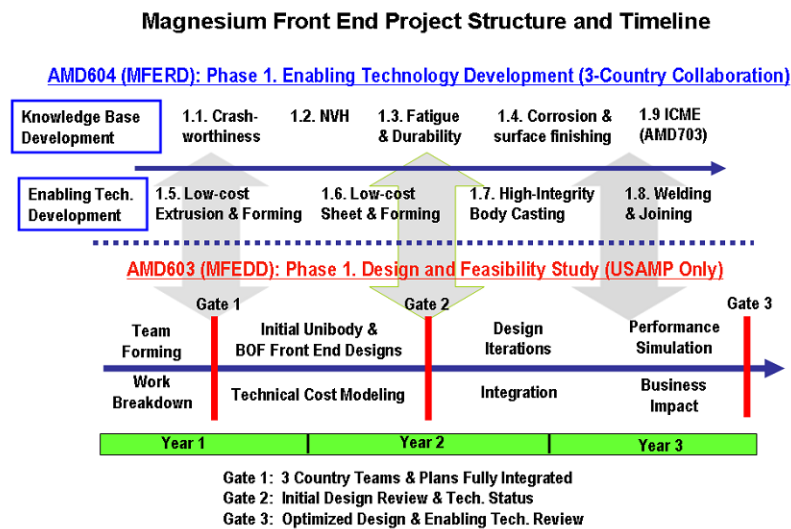


**Figure 2.** Schematization of AMD603 and AMD604 partitioning, timing, and technical gateways.

## Accomplishments

The relationship between activities of the individual task areas and overall project objectives is shown in the fishbone diagram of Figure 3. Targets for knowledge-based and enabling technologies are illustrated therein. General project accomplishments for FY 2008 are summarized below.

- Participated in 2nd International Review Conference held in Hangzhou, PRC, from April 1–4, 2008.
- Contributed to a 366 page proceedings volume detailing work on the project up to the review date.
- Conducted an agenda of individualized visits within the People’s Republic of China to specific institutions conducting task-related project work. Such visits included travel to Shanghai, Hangzhou, Chongqing, Xi’an, Louyang, Dalian, Shenyang, and Beijing.
- Conducted meetings of the Project Steering Committee (PSC) and Project Technical Committee (PTC) in conjunction with the review in Hangzhou. Additionally, PTC conference calls were held on July 30 and November 19, 2008.
- The Mississippi State University (MSST) “SharePoint” web site for project information sharing between international groups became operational in March 2008 and was rolled out at the Hangzhou meeting.
- The USAMP annual review of Project AMD604 was held on October 20, 2008, and participants from the Canadian and Chinese teams were in attendance. A group of U.S. participants attended the Canada annual review at the University of Sherbrooke, Quebec, on September 23–24.
- Conducted individual Task Team international conference calls at various times during the project year.
- The next annual international review meeting for the project will occur from May 11–13, 2009, at Niagara-on-the-Lake, Ontario, Canada.
- The USAMP AMD604 Project presented its “Gate 2” review to the AMD Board of Directors on July 18, 2008, and after some refinement of status reporting and metrics was given approval for continuation of Phase I.
- Thirty-six individual supplier companies or institutions have provided work plans and received USAMP contracts.
- USAMP AMD604 task area highlights are as follows.
  - Task 1.1 Crashworthiness—Acquisition and analysis of deformation characteristics of selected coupon materials over a range of agreed-upon strain rates and temperatures. Devised and manufactured standardized “box” crush sections for comparison of physical testing and computer simulation of deformation. Conducted initial simulations and deformations for the extruded and sheet formed box section structures.
  - Task 1.2 Noise, Vibration and Harshness (NVH)—Completed requisite documentation to enlist U.S. supplier (IAC) to support and complement Canadian and Chinese works and to provide two-layer panel samples. Reporting of initial transmission loss data from supplier IAC for exemplary Mg-intensive Chrysler prototype vehicle.
  - Task 1.3 Fatigue and Durability—Completed round-robin fatigue testing of extruded AM30 by all participants. Obtained initial fatigue data on AZ91D super vacuum die casting (SVDC) shock towers and AS31 sheet. Additional fatigue studies including piece fabrication and prototypical joint structure are underway.
  - Task 1.4 Corrosion and Surface Treatment—Prototype surface treatments received from China for analysis. First round of U.S.-based pretreatments concluded. Protocol for fastener galvanic corrosion established. Proposals for assessment of complete coating systems developed. Assembly protocol proposed to accommodate metal pretreatment prior to adhesive bonding.
  - Task 1.5 Extrusion—Conducted extrusion trials of AM30 and AZ61 alloys for the “double top hat” crush box prototype. Conducted texture measurement and mechanical properties of extruded AM30 to ascertain anisotropy of mechanical properties. Extrusion simulation studies conducted at Lehigh University. Coordination with ICME Extrusion task at MSST.
  - Task 1.6 Sheet Forming—Various AZ31 sheet materials show similar constitutive behaviors approximating the Sellars-Tegart model. For pan forming, the binder pressure was found to be critical to forming

- capability as well as temperature. Sheet interaction with lubricant and the tool surface was found to override microstructural differences among alloys evaluated. Exemplary continuous cast sheet material has now been received from China for evaluation.
- Task 1.7 High-Integrity Body Castings—Prototype shock tower castings were produced in both AZ91D and AM60B using the novel SVDC process. An alternative vertical vacuum die casting process was also used to produce coupon pieces for properties determination. Initial mechanical property data suggests superior elongations achievable with such processing and strength levels approaching, but not exceeding, the anticipated design levels.
  - Task 1.8 Joining—Completed guidelines for structural and nonstructural breakstem rivets. Completed assessment of the strength, durability, and corrosion performance of 10 pretreatments applied to AZ31 sheet, AM60B casting, and AM30 extruded Mg. Performed preliminary nondestructive evaluation (NDE) assessment of X-ray and ultrasonic evaluation of self-piercing rivet (SPR) joints.
  - Task 1.9 ICME—(International nomenclature) Reported separately as USAMP project AMD703.

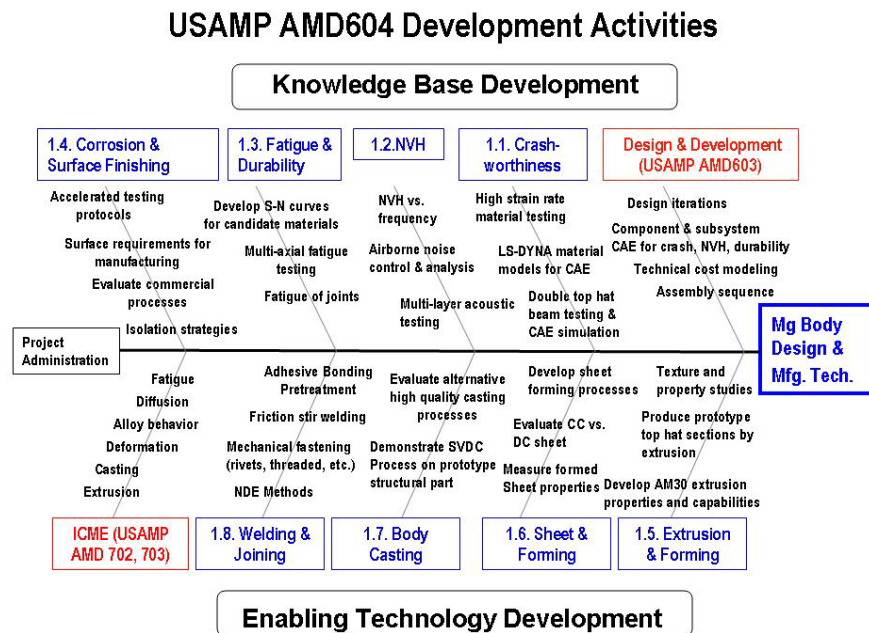


Figure 3. Magnesium front-end project/task structure fishbone diagram.

**Future Direction**

- Continuation of international discussions and progress reports via next annual meeting at Niagara-on-the-Lake, Ontario, Canada (May 11–13, 2009).
- U.S. Task Teams to provide updated physical property, material performance, and manufacturing recommendations to AMD603 Design Team as such data becomes available.
- Gate review and potential development of Phase II International project to be conducted prior to and during the next International Project Review meeting in Canada.
- “Knowledge-base” information to be collated and recorded in media accessible to the participants (e.g., via USCAR Vroom for U.S. or MSST SharePoint web site for international participants).

**Introduction**

Details of the AMD604 (MFERD) project, including its background and rationale, were

included in the prior annual reviews and are not repeated here for reasons of brevity [1]. This report emphasizes achievements of the second full



year of the project with a focus on those task items accomplished through the USAMP AMD604 Project. Accomplishments of the international partners during this period are detailed in a separate report [2]. The overarching objectives of the effort are (1) the development of a knowledge base for use in eventual design and (2) the realization of enabling manufacturing technologies for Mg componentry, as may be assembled into durable vehicle substructures. These broad objectives collectively support design and potential manufacture of Mg-intensive automotive structures such as the “front end” portrayed in Figure 1. Technical obstacles to the realization of structurally sound and durable Mg-intensive assemblies are well known and itemized in USAMP’s roadmap document for Mg technology [3]. The agenda for the various project tasks as detailed in Figure 3 support the overarching technical challenges of the project as a whole.

During FY 2008, substantial progress was made in all task areas, not only in the U.S., but in Canada and China as well, as had been demonstrated at both the international review in Hangzhou, and the Canadian annual meeting in Sherbrooke. Sample materials are now being distributed to the various laboratories and measurements are being reported through the international task teams. The “knowledge” tasks 1–4 are regularly reporting results and sharing sample materials as they become available. Some international task teams are also progressing to the point of regular international conference calls and web meetings to review status and discuss various results. The “SharePoint” web site, maintained by MSST, is being populated with project reports and data.

The overarching project philosophy, dating back to initial discussions of such an extensive collaborative effort, encompasses both a set of extraordinary opportunities in vehicle design and performance, and concomitantly, a set of grand challenges for the scientific and technological underpinnings of such a concept. The opportunities arise from the theoretical potential for an approximate 50% (or better) mass savings as compared to a mild steel baseline for components of comparable stiffness. Additionally, the die casting process, and its derivatives, for Mg alloys could readily permit considerable piece-part

consolidation and thereby systemic cost reduction. Design targets such as mass redistribution and mass-loss compounding are also realizable. The grand challenges derive principally from the basic materials science of Mg metal and its various commercial alloys: (a) exceedingly temperamental mechanical properties fundamentally attributable to its hexagonal close-packed crystal structure and (b) extraordinarily large electrochemical oxidation potential, rendering it anodic to virtually all other engineering materials to which it may be coupled. While scientific and technical approaches to these grand challenges exist, principally through alloying, microstructural control, thermomechanical processing, and protective surface treatments, it is not clear that any of the scientifically accepted remedies might become so commonplace as to be readily accepted into the automotive manufacturing environment where cost, availability, and performance are paramount.

ICME has the potential to address the grand challenges from the standpoint of orchestration of the basic physical metallurgy of Mg and its processing into a less formidable undertaking [4]. Mg alloys could be among the first engineering materials to benefit from ICME. The companion projects (AMD702 and 703) seek to take advantage of the ICME approach and worldwide community of practitioners.

The following sections describe key technical attributes of the project and accomplishments occurring during federal fiscal year (FY) 2008.

## **2008 Progress and Accomplishments**

**Project Management and Organization.** The project managerial structure as originally set forth is fully operational, and requisite meetings of the PSC and PTC are ongoing. All project documentation is received and archived. The second annual review meeting was held in Hangzhou, PRC, in April 2008, and a bound proceedings volume was concurrently published for use by team members [2]. All task area committees are functional and work flows are progressing according to the initial project work statement or amended versions as agreed upon by the task teams. The USAMP companion design project (AMD603) has generated a number of

outcomes, from which generalized design guidelines can flow into the relevant committee structures, short of actual complete design details. The next international review meeting is scheduled to occur at Niagara-on-the-Lake, Ontario, Canada, from May 11–13, 2009.

**Task 1.1—Crashworthiness.** The Crashworthiness task includes material testing, computer-aided engineering (CAE) analyses, and testing of beams in bending and axial compression. During 2008, approximately 85% of the material testing was completed on the five Mg alloys of interest: AM30 and AZ31 extrusions, AZ31 sheet, AM60 and AM50 die castings. AM30 extruded box-section beams were tested in slow four-point bend, slow axial compression, and fast axial compression. LS-DYNA models predicted beam response. The high speed axial crush test involves local corner and flat section buckling, local plastic deformation, high local strains, locally high strain rates, material cracking, and separation. The LS-DYNA model predicted a peak axial load 50 kN higher than the peak load measured in the six tests. The overprediction of the peak load and the overprediction of the continuing collapse load results in more than a 100% overprediction in the calculated energy absorbed during the first 200 mm of deformation. The initial LS-DYNA predictions did not include cracking. The tested parts all exhibited significant material cracking and fracture as shown in Figure 4.



**Figure 4.** Final deformed shape of the extruded Mg AM30 beam after an axial compression test.

Continuing efforts of the task are aimed at reconciling differences between predicted and observed crush behaviors, as well as extending the

measurements and calculations to the other materials of interest, once an acceptable CAE formalism has been determined.

**Task 1.2—NVH.** The U.S. team enlisted the participation of supplier company IAC, and acquired sound transmission loss (STL) data for 1 mm and 2 mm sheet Mg materials as employed in an exemplary Chrysler Mg-intensive vehicle dash structure. These data are shown in Figure 5, where it can be seen that the 2 mm material approximates loss values from 0.8 mm steel sheet. Additionally, IAC provided data for Mg sandwich structures employing structural foams as acoustic resistance between flat-panel elements. The U.S. team also supplied generic NVH materials information to support the CAE modeling activities internationally.

**Task 1.3—Fatigue and Durability.** Subtasks for this topic include the international round-robin fatigue testing of excised coupons from an extruded AM30 Mg structure, originally devised by one of the OEMs. Strain-life data from these coupons has now been collected and typical results from 0.3% and 0.6% strain are summarized in Figure 6.

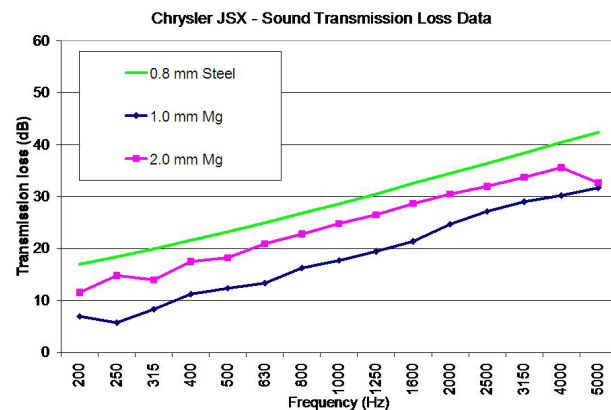


**Figure 5.** STL for 0.8 mm steel sheet and 1 mm and 2 mm Mg sheet as determined by IAC Corporation.

Monotonic stress-strain data collected to date from the particular AM30 extruded material show an average ultimate tensile strength of 245 MPa, yield strength of 170 MPa, and elongation in the

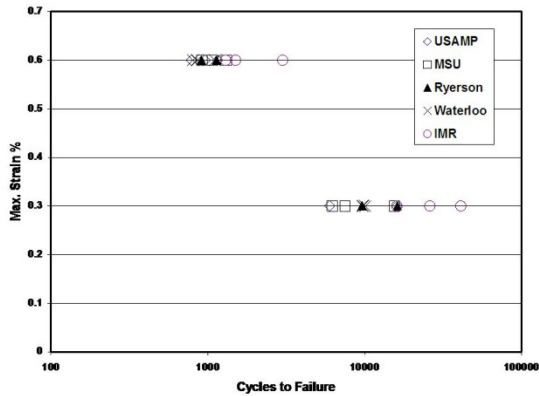


**Figure 6.** Strain-life data points from extruded AM30 structural piece by laboratory.

range of 15–20%. Fatigue testing to date has not taken into account the large plastic deformation anisotropy associated with extruded materials, and such data will eventually need to be obtained. The crush tube extrusions employed by the crashworthiness task, however, have wall thicknesses too thin (ca 2 mm) for idealized fatigue test geometries. MSST has provided recommendations for specific joint geometries for fatigue testing of weldments.

**Task 1.4—Corrosion and Surface Treatment.** The Task 1.4 Team assessed various pretreatments including conversion type treatments and anodized surfaces for application with both paint and adhesive overlayers. Additionally, a statistically designed experiment (DOE) was conducted to evaluate sensitivities for a proposed VDA-based protocol for measuring the resistance of coatings on steel fasteners to galvanic coupling to adjacent Mg alloy structures. An experimental approach to the assessment of completed coating systems including metal pretreatment and polymeric topcoat layers was developed by Eastern Michigan University. This methodology, known as AC/DC/AC, utilizes electrochemical impedance spectroscopy (EIS) as the primary measurement technique, with provision for a cathodic direct current stress applied to the specimen to force undercut corrosion of the polymer layer, as is expected to occur with Mg. Typical results from this approach are illustrated in Figure 7, which shows initial Bode plots (modulus vs frequency)

for the AZ31 sheet and AM60B die casting and subsequent plots revealing a more severe degradation of the coating system for the AZ31 sheet in comparison to the AM60B die casting. The approach greatly reduces the time required to make an assessment of the total coating system by approximately a factor of ten. The international team has also discussed the matrix of expected test protocols for the various situations as may exist on a hypothetical front-end structure, ranging from coating durability and corrosion resistance to fastener studies and evaluation of environmentally-assisted fractures, either stress-corrosion crack or corrosion fatigue.

**Task 1.5—Low-Cost Extrusion.** Although the initial conceptual design for the unibody front-end structure suggests a relatively small number of extrusions, these components are crucial insofar as providing among the higher specific strengths observed for structural Mg alloys and expectation of use in critical positions such as bumper beams and crush rails. The traditional limitation to greater use of Mg extrusions is the generally high cost of manufacture, dictated in part by the relatively low rate of production due to the intrinsically poor formability of the material. An emerging concern is also the large degree of mechanical property anisotropy (in particular, yield strength) being observed for shapes such as the crush tube for Task 1.1 as illustrated in Figure 8. Efforts underway include expanded use of modeling software such as DEFORM 3-D to predict and optimize extrusion behavior for specific cross-sections. The Institute for Metal Forming of Lehigh University has conducted modeling and microstructural evaluations of the extrusion process. The topic is similarly linked to AMD702 (ICME) efforts at MSST to understand the influence of microstructure on the extrusion process. First-year results also include initial measurement of crystallographic textures of extruded shapes at key locations. A major U.S. supplier of extrusions, Timminco Inc., has been enlisted to produce experimental shapes as shown above for the project in both AM30 and AZ61 alloys. Extruded tubes of alloys AM30, AZ31, and AZ61 from China have been chemically analyzed and material properties determined.

### AC/DC/AC Method

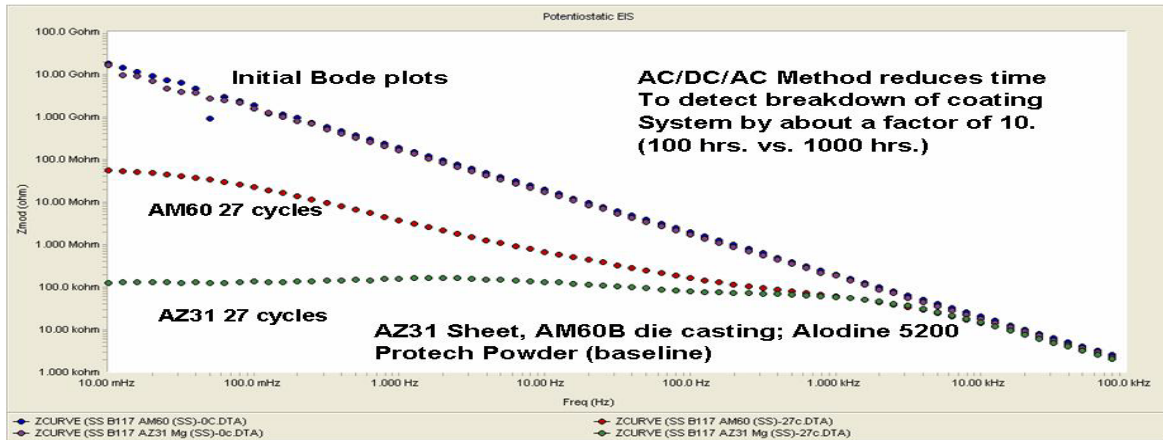


Figure 7. Before and after EIS evaluation of AZ31sheet and AM60B die casting with comparable surface treatments.

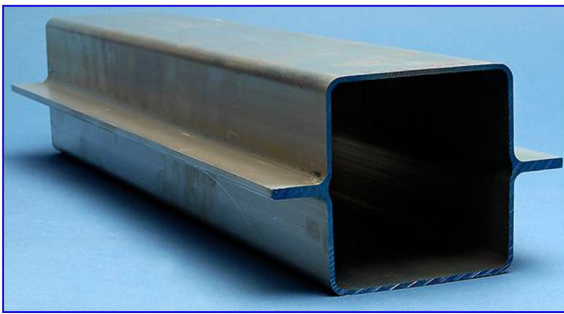


Figure 8. AM30 alloy extruded as a “crush tube” for crashworthiness and mechanical property studies of deformation anisotropy.

**Task 1.6—Low-Cost Sheet and Forming.** Efforts on low-cost sheet forming of Mg are incorporated in USAMP project AMD602, and only differentials requisite for the “front end” structure are considered here. To date, a variety of commercially available sheet materials of both direct chill and continuous cast materials are available and comparative sheet forming results were obtained. The various sheet materials all showed similar deformation behavior, generally capable of constitutive modeling using the Sellars-Tegart equation [5]. In “pan” forming (which has been the principal approach of AMD602), binder pressure is critical for forming deeper pans without wrinkling. The interaction of the sheet material with the lubricant and die surface tends to override any microstructural differences in the

starting materials. The lowest temperature for successful pan forming was found to be 275°C. Figure 9 illustrates the acceptable forming regime plotted as number of acceptable “corners” of the pan, in terms of binder pressure and forming temperature.

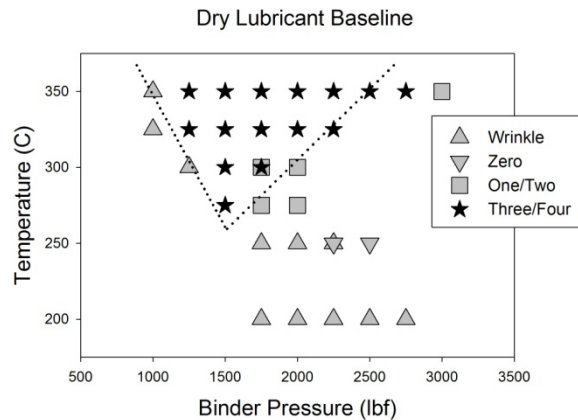


Figure 9. Regime of acceptable forming of a pan structure from AZ31 sheet, in terms of sheet preheat temperature and binder pressure.

**Task 1.7—High-Integrity Body Castings.** The companion design project (USAMP AMD603) suggests a strong reliance on large Mg alloy castings which simultaneously achieve both weight reduction and part integration, contributing to lowering of manufacturing cost. The casting process also permits adjustment of section thickness at various locations in the component,

which is generally not achievable in sheet forming processes. The traditional high-pressure die casting process, presently used to form large structures in Mg, can suffer from substantial reductions in localized strength and elongation when compared to the maximum theoretical values for the material. These variations are primarily due to incorporation and distribution of porosity resulting from the turbulent nature of the die-casting process itself. ICME is expected to play a major role in addressing those physical attributes of the metal flow and solidification which can lead to improved properties. Vacuum-based processes have also been found to reduce the quantity of entrained gas and permit generally improved metal flows into the die cavity. International efforts are aimed at exploring alternative casting processes [e.g. Thixoforming (Canada), squeeze casting (China)] as remedies to challenge at hand. Additionally, heat treatments may be a remedy to improve performance of the as-cast structures.

In FY 2008, initial trials have been conducted with two vacuum processes, including a horizontal process (SVDC—Contech, LLC) and vertical (Gibbs Die Casting) approaches. Figure 10 illustrates a shock tower component of a front-end structure as implemented in SVDC.



**Figure 10.** AM60B shock tower produced by the horizontal SVDC process.

Although yield strengths of excised coupons appear marginally below isolated coupon or handbook values, improvement may be possible through minor alloy modifications. Elongation,

indicative of the influence of porosity, is markedly improved by the vacuum processes.

**Task 1.8—Joining:** The U.S. Task 1.8 team is focused on the following subtask areas: (a) adhesive bonding, including pretreatment and degradation; (b) NDE of all joint types; (c) friction stir welding; and (d) fasteners, including threaded fasteners, breakstem rivets, and SPRs. Hitachi America was enlisted as a project participant in 2008 to provide developmental friction-stir welding of both spot and linear welds. A supplier is still being sought for development of SPR technology as this technology is expected to have substantial use in manufacture of unibody Mg front-end structures.

A major achievement in 2008 was the assessment of various metal pretreatments available either developmentally or in the marketplace, including several representative treatments from participating organizations in China. Several key design factors surround the selection and performance of metal pretreatments: (a) current design considerations for the unibody assembly suggest widespread use of adhesive bonding in concert with other techniques, hence the requirement that metal surfaces receive some form of pretreatment prior to the build process, (b) corrosion undercutting of the adhesive is an undesirable failure mode of the bond, and also a concern for painted surface degradation in other areas of the structure, and (c) design for durability must take into account any degradation of adhesively bonded joints with regard to structural integrity in service.

Figure 11 shows adhesive bond fracture appearance and strength degradation data obtained from lap-shear tensile pull testing of pretreated, bonded, and corrosion-exposed joints. Comparative before/after strength values for two different metal pretreatments (denoted “A” and “B”) and resultant fracture paths after 30 cycles of a standardized cyclic corrosion test (Ford APGE) are shown. For pretreatment “A” the fracture is characterized by complete undercutting of the bond and substantial loss in lap-shear strength, while in “B” the joint was seen to fail through the adhesive material as is desirable for adhesive bonding. Similar measurements were conducted

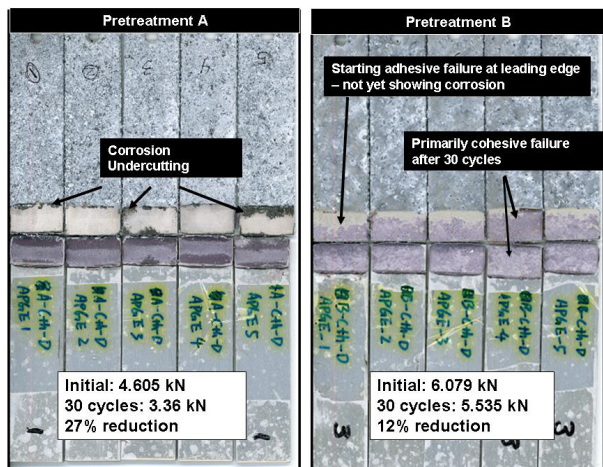


**Figure 11.** Typical locus of fracture experiment results for tensile lap-shear coupons for comparative assessment of pretreatment durability.

over a matrix of 10 different pretreatments, permitting levels of acceptance to be established. Assessment of general corrosion resistance of the same pretreatments was also undertaken by Task 1.4 (Corrosion).

**Conclusions**

At the end of its second full year, AMD604 continues to demonstrate progress toward objectives for all of the individual task areas, with considerable challenges remaining in many of them. The organizational framework, both nationally and internationally, is functional; despite impediments of time, space, and language, the collaborative approach is proving to be both scientifically and culturally gratifying to the participants. Materials, data, and discussions are regularly transcending the obstacles once imagined. New friendships and networks are developing.

The pivotal milestone of FY 2009 will be the collective decision by the participants regarding the future of the project. Factors both scientific and otherwise will surely make this discussion both exciting and challenging for those involved

**Presentations/Publications**

1. A. A. Luo, E. A. Nyberg, K. Sadayappan, and W. Shi, “Magnesium Front End Research and Development: A Canada-China-USA

Collaboration,” pp 3–10 in M. O. Pekguleryuz, N. R. Neelameggham, R. S. Beals, and E. A. Nyberg, eds. *Magnesium Technology 2008*, TMS Annual Meeting, New Orleans, Louisiana, March 9–13, 2008, TMS, Warrendale, Pennsylvania (2008).

2. E. A. Nyberg, A. A. Luo, K. Sadayappan, and W. Shi, “Magnesium for Future Autos,” *Advanced Materials & Processes*, **166**(10), 35–37 (2008).

**Acknowledgments**

The success of this project is due to the dedicated efforts of a large number of team members at Chrysler, Ford, and General Motors; the various supplier organizations listed below; and the international counterparts in Canada and China. The current and past USAMP core team members, Steve Logan, Randy Beals, and Eric McCarty of Chrysler; John Allison, David Wagner, Mike Maj, Joy Hines Forsmark, and Jake Zindel of Ford; James Quinn, Dick Osborne, Larry Ouimet, Ravi Verma, and Theresa Lee of General Motors, are acknowledged for their significant contributions and tireless efforts. Continuing support from our respective organizations and DOE is gratefully acknowledged.

- |   |                                       |
|---|---------------------------------------|
| University of Dayton Research Institute | North Dakota State University         |
| Troy Tooling Technologies               | Luke Engineering & Mfg. Corp.         |
| Cosma Engineering                       | Technical Applications Group          |
| Contech U.S., LLC                       | Timminco Corporation                  |
| IAC Group North America                 | Lehigh University                     |
| Westmoreland Mech. Testing & Research   | Scientific Forming Technologies Corp. |
| Metokote Corporation                    | Magnesium Elektron North America      |
| Henkel Corporation                      | Contech Global, LLC                   |
| PPG Corporation                         | EKK Corporation                       |
| Chemetall-Oakite Corporation            | U.S. Magnesium                        |
| Keronite                                | North American Die Casting Assn.      |
| International Hardcoat Corporation      | Gibbs Die Casting                     |
| MacDermid, Incorporated                 | Hitachi                               |
| The Magni Group, Inc.                   | ATF                                   |
| Atotech Corporation                     | REMINC                                |
| Kamax LP                                | Visteon                               |
| Ohio State University                   | MNP Corp.                             |
| Eastern Michigan University             | Dow Automotive                        |
| University of Michigan - Dearborn       |                                       |

**References**

1. A. Luo, R. C. McCune, J. A. Carpenter, A. D. Yocum and P. S. Sklad, “Mg Front-End Research and Development (AMD604 ),” FY 2007 Progress Report, U.S. DOE, 2008.

2. A Canada-China-USA Collaborative Research and Development Project, "Magnesium Front End Research and Development (MFERD)," 2007 Annual Progress Reports, Project Technical Committee, Hangzhou, China, April 2008.
3. USAMP, "Mg Vision 2020: A North American Automotive Strategic Vision for Mg," Nov. 1, 2006.
4. "Integrated Computational Materials Engineering: A Transformational Discipline for Improved Competitiveness and National Security," Committee on Integrated Computational Materials Engineering, National Research Council, ISBN: 0-309-12000-4 (2008).
5. <http://www.nap.edu/catalog/12199.html>.
6. M. Sellars and W. J. Tegart, "Relationship between Strength and Structure in Deformation at Elevated Temperature," *Mem. Sci. Rev. Metall.* **63**, 731–745 (1967).

## **D. Nanotechnology-Based Self-Healing Coating System to Enable Use of Magnesium Alloys in Automotives**

*Principal Investigator: Dr. Jiong Liu*

*Alternate POCs: Mr. Shekhar Bafna and Dr. Ganesh Skandan, CEO*

*NEI Corporation*

*400 Apgar Drive, Suite E*

*Somerset, NJ 08873*

*732-868-3141; fax: 732-868-3143; E-Mail: JLiu@neicorporation.com; gskandan@neicorporation.com*

*Technology Area Development Manager: Joseph A. Carpenter*

*(202) 586-1022; fax: (202) 586-1600; e-mail: joseph.carpenter@ee.doe.gov*

---

*Contractor: NEI Corporation*

*Contract No.: DE-FG02-08ER85204 through the Small Business Innovation Research and Small Business Technology Transfer Program*

---

### **Objective**

- To develop chromate-free self-healing coating systems, including pretreatment and primer, which exhibit damage-responsive corrosion protection to magnesium substrates.

### **Approach**

- The pretreatment was based on a polymer which reacts with the magnesium cations formed under mildly acidic conditions. This reaction in turn leads to the formation of a thin and dense protective film on the metal surface.
- Nanoscale corrosion inhibitors added to the pretreatment matrix were based on a functionalized nanoparticle. Active components leach out from the nanoparticle and retard the cathodic corrosion reactions of magnesium by forming a dense protective film on the surface.
- Chromate-free corrosion inhibiting particles that can be added into primer formulations mimic the self-healing behavior of chromate-based corrosion inhibitors which can diffuse through the coating matrix to defect sites and transition from higher to lower valence state by undergoing reduction to form a protective and stable film on the metal surface.

### **Accomplishments**

- Demonstrated the ability of a waterborne inorganic-organic hybrid pretreatment (hereafter NEI pretreatment) containing functionalized nanoparticles to passivate the surface of AZ91D magnesium alloy. The NEI pretreatment forms a coherent barrier layer, with corrosion inhibition provided by the functionalized nanoparticles.
- Demonstrated that the NEI pretreatment is compatible with commercial automotive e-coat and powder coat, and that the coatings applied on the surface treated substrate do not have any defects.
- Demonstrated self-healing behavior of the NEI pretreatment through direct current (dc) polarization studies: the corrosion current of AZ91D was reduced and the corrosion potential was increased by the NEI pretreatment;
- Developed a novel, chromate-free corrosion-inhibiting particle based on a transition metal. Electrochemical tests showed the ability of this particle to result in a passivating film on AZ91D, mimicking that of a chromate pigment.
- Formulated a corrosion-inhibiting automotive epoxy primer and powder coat containing the newly developed chromate-free particle and demonstrated self-healing corrosion protection.



## Future Direction

- The Phase I project is complete.
- Phase II, if awarded, will be focusing on the development of a self-healing pretreatment and powder coat to mitigate galvanic and general corrosion of magnesium components.

## Introduction

This Phase I project was completed in April 2008. The overall purpose of this study was to search for effective chromate-free self-healing coating systems to protect lightweight magnesium die-cast alloys from corrosion.

NEI Corporation demonstrated self-healing characteristics in a newly developed pretreatment and primer applied on the most commonly used magnesium structural alloy, AZ91D. Corrosion tests showed that the pretreatment with nanoscale particles has the ability to provide damage-responsive corrosion protection to the magnesium substrate. A corrosion-inhibiting epoxy spray primer and powder coat were also formulated in the Phase I program. It was found that the corrosion-inhibitor particles have the ability to leach out from the coating to active corrosion sites on the magnesium substrate and provide self-healing. Hence, the combination of a corrosion-inhibiting pretreatment and powder coat has the potential to provide enhanced corrosion protection to magnesium compared to the current coatings. The coating formulations used in the Phase I program are significantly different from the state-of-the-art, and are enabled by nanotechnology. The pretreatment and primer formulations contain functionalized nanometer-sized particles (hereafter nanoparticles) with corrosion-inhibiting ions incorporated directly into a polymer matrix. These ions readily leach out and form a protective insoluble film at the active corrosion sites. Excellent adhesion and barrier properties are attributed to the formulation chemistry, which also enables efficient transport of the corrosion-inhibiting species. The formulations are stable suspensions and the coatings are homogeneous systems at the micro- and macro-scale, since they contain well-dispersed nanoparticles.

## Development of a Waterborne Pretreatment Formulation Containing Nanoparticle Corrosion Inhibitor

The NEI pretreatment formulation has a hybrid inorganic-organic matrix containing functionalized nanoscale particles. The hybrid matrix not only acts as an adhesive forming strong bonds with the metal surface, but also provides corrosion protection by forming an insoluble barrier film. The functionalized nanoparticles enable the corrosion inhibition of AZ91D alloy.

Figure 1 shows dc polarization curves of different commercial and NEI pretreatments on AZ91D alloy. The data show that the alloy has a high activity with an open-circuit potential of -1.5 V.

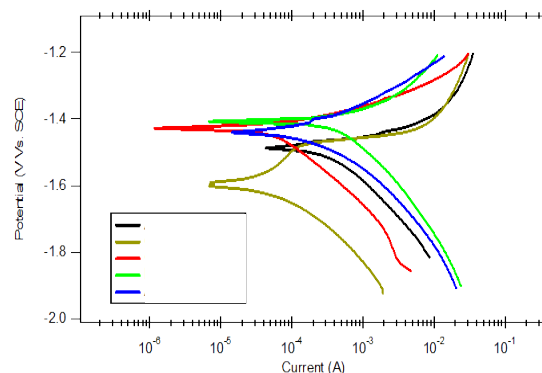


**Figure 1.** Polarization curves of different pretreatments on AZ91D in 3% salt-water solution.

Application of the NEI pretreatment, nonchromate II pretreatment and chromate conversion coating (Dow 7) shifts the polarization curve to a more noble value of about -1.4 V, indicative of a passivation coating which is less reactive to the salt solution compared to the

AZ91D alloy. The corrosion current of NEI pretreatment, non-chromate II pretreatment is lower by an order of magnitude compared to the AZ91D alloy, implying durability and protective properties of the pretreatments. With the NEI pretreatment, there is a positive shift in the  $E_{corr}$  similar to the chromate conversion coating (Dow 7).

### **Deposition of Commercial E-coat on Pretreated AZ91D Panels**

During the Phase I program, we performed e-coating of NEI and commercially pretreated AZ91D coupons at a commercial E-coat company who showed keen interest in our research efforts and allowed the use of their e-coating line for our panels at no charge. Panels were tested in the salt fog test to determine the corrosion resistance of the e-coat applied on NEI and other commercial pretreatments.

Figure 2 shows photographs of e-coats applied over untreated AZ91D panels and panels after NEI pretreatment with and without corrosion inhibitors. The photographs were taken after four weeks of salt fog testing. Untreated panels undergo severe delamination of the e-coat and corrosion products form along the scribe (Figure 2a). NEI pretreatment without nanoscale corrosion inhibitors showed significant improvement in the scribe creep indicating strong adhesive properties of the pretreatment (Figure 2b). Addition of functionalized nanoparticles into the pretreatment further decreased the scribe-creep and showed no corrosion along the scribe lines (Figure 2c). However, e-coat applied over NEI pretreatment containing nanoparticle corrosion inhibitors show some defects over the surface. This is presumably due to the aggregation of nanoparticles which led to defects on the coating surface. The Phase II effort will optimize the pretreatment formulation to eliminate these defects.

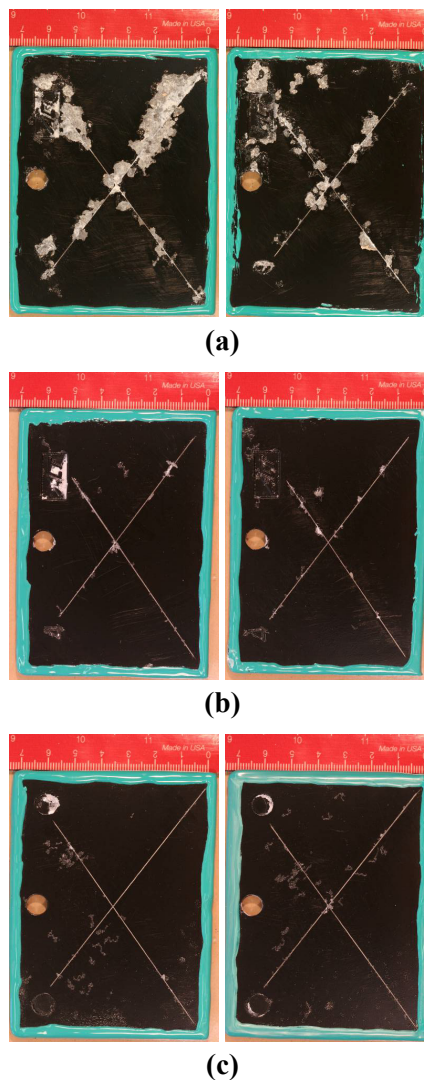


**Figure 2.** Photographs of epoxy e-coat applied over AZ91D panels having different pretreatments after 4 weeks of American Society for Testing and Materials B-117 salt fog test. (a) Untreated AZ91D, (b) NEI pretreatment without nanoparticle corrosion inhibitor, and (c) NEI pretreatment with nanoparticle corrosion inhibitor.

### **Synthesis of Chromate-Free Corrosion Inhibitor Particles for Powder Coat**

A new corrosion-inhibiting compound containing transition metal was synthesized. This particle mimics the self-healing behavior of chromate-based corrosion inhibitors which can diffuse through the coating matrix to defect sites and transition from higher- to lower-valence state by undergoing reduction to form a protective and stable oxide film on the metal surface. The ability of the chromate-free particle to change valence state was confirmed by X-ray photoelectron spectroscopy (XPS) and ultraviolet-visible (UV-Vis) spectroscopy. Figure 3 shows that the corrosion current is lowered by an order of magnitude by the NEI chromate-free particle compared to a blank AZ91D sample, indicating that the inhibitor particle led to the formation of a passivating film on the AZ91D surface.

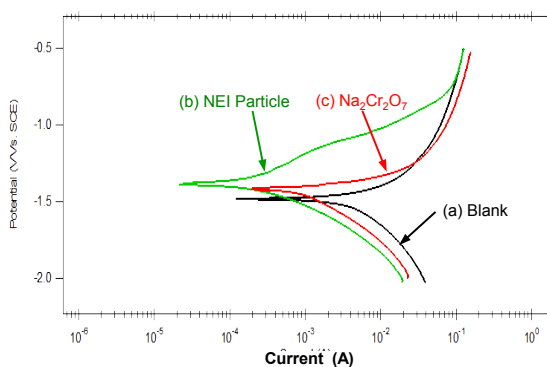


**Figure 3.** The dc polarization of AZ91D exposed to (a) 3% NaCl solution, (b) 3% NaCl + 0.2% NEI chromate-free particle solution, and (c) 3% NaCl solution + 0.2% sodium dichromate. Panels were exposed to the solutions for 3 hours before the anodic and cathodic scans were performed.

### **Development of Corrosion-Inhibiting Powder Coat and Liquid Epoxy Primers to Achieve “Self-healing” Corrosion Protection**

The newly developed, chromate-free particles were successfully incorporated into an epoxy powder coat and an automotive refinish epoxy primer with excellent dispersive properties (Figure 4). Figure 5 shows photographs of micrometer-sized artificial defects made in the epoxy primer before and after immersion in salt

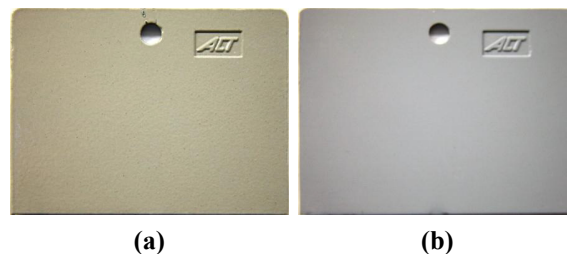


**Figure 4.** Photographs of (a) epoxy powder coat with 4 vol % NEI chromate-free inhibitor and (b) epoxy liquid spray primer with 5 vol % NEI chromate-free inhibitor.

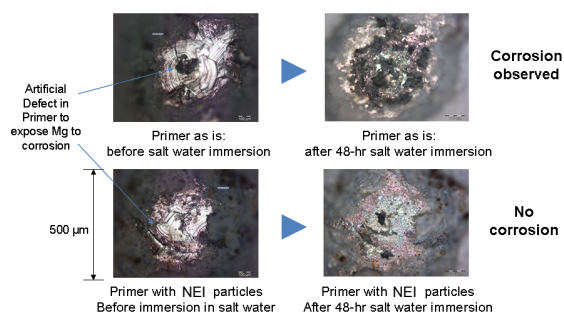


**Figure 5.** Optical micrographs of artificial defect made in epoxy primer with and without NEI chromate-free particles. AZ91D test coupons before immersion in 3 % NaCl solution and after 48 hours immersion are shown.

water for 48 hours. It demonstrates that the defect in the primer without NEI corrosion inhibitors is completely corroded indicating the high propensity of the Mg alloy to corrode. On the other hand, the defect in the primer containing 5 wt% NEI particles does not corrode and shows the appearance of a protective film on the surface.

### **Conclusions**

A self-healing pretreatment and a self-healing powder coat for corrosion protection of magnesium alloy AZ91D have been developed in Phase I. Electrochemical and salt-water immersion tests showed that an organic-inorganic hybrid pretreatment containing functionalized nanoparticle passivates AZ91D and lowers its rate of corrosion. A transition-metal-based corrosion-inhibiting particle was synthesized in the program. Preliminary tests in salt-water immersion and potentiodynamic polarization showed the ability of the inhibitor to mimic inhibiting properties of chromium salt. Further confirmation of inhibitive properties of the particles was detected by UV-Vis

spectroscopy and XPS. The Phase I program has demonstrated the feasibility of inhibiting corrosion of magnesium by the proposed pretreatment and primer/powder coat process.

### **Presentations/Publications/Patents**

1. J. Liu, S. Bafna, F. Allen, and G. Skandan, "Chromate-free Corrosion Resistant Nanocomposite Pretreatments for Structural Metals", Mega Rust Navy Corrosion Conference, Norfolk, Virginia, June 2009.
2. J. Liu, S. Bafna, F. Allen, and G. Skandan, "Chromate-free Corrosion Resistant Nanocomposite Pretreatments for Light-weight Metals", 215th ECS meeting, San Francisco, California, May 2009.
3. F. Allen, S. Bafna, J. Liu, and G. Skandan, "Corrosion Inhibiting Chromate-free Nanocomposite Pretreatments for Structural Metals", U.S. Army Corrosion Summit, Clearwater Beach, Florida, February 2009.
4. S. Bafna, J. Blair, and G. Skandan, "Corrosion Resistant Coatings for Light Metal Alloys", 236th ACS National Meeting, Philadelphia, Pennsylvania, August 2008.

## **E. High-Strain-Rate Characterization of Magnesium Alloys**

*Principal Investigator: Srdjan Simunovic*

*Oak Ridge National Laboratory*

*P.O. Box 2008, Oak Ridge, TN 37831-6164*

*(865) 241-3863; fax: (865) 241-0381; e-mail: simunovics@ornl.gov*

*Co-Principal Investigator: J. Michael Starbuck*

*Oak Ridge National Laboratory*

*P.O. Box 2009, Oak Ridge, TN 37831-8048*

*(865) 576-3633; fax: (865) 574-8257; e-mail: starbuckjm@ornl.gov*

*Co-Principal Investigator: Don Erdman*

*Oak Ridge National Laboratory*

*P.O. Box 2009, Oak Ridge, TN 37831-8048*

*(865) 576-4069; fax: (865) 574-0641; e-mail: erdmandl@ornl.gov*

*Technology Area Development Manager: Joseph A. Carpenter*

*(202) 586-1022; fax: (202) 586-1600; e-mail: Joseph.Carpenter@ee.doe.gov*

*Field Technical Monitor: C. David Warren*

*(865) 574-9693; fax: (865) 574-6098; e-mail: warrencd@ornl.gov*

---

*Contractor: Oak Ridge National Laboratory*

*Contract No.: DE-AC05-00OR22725*

---

### **Objectives**

- Characterize mechanical material properties of magnesium (Mg) alloys for automotive applications.
- Determine material model parameters for various constitutive models available in crash codes.
- Develop methods for interrupting strain-rate test at the prescribed strain.
- Experimentally determine evolution of material properties for various loading situations and strain rates.
- Formulate experimental findings into constitutive models based on continuum damage mechanics.
- Establish test and property database for automotive Mg alloys.

### **Accomplishments**

- Performed initial strain-rate test in tension for Mg AM60 alloy.
- Developed preliminary design of the fixture for interrupted strain-rate tests in tension
- Developed database for test data analysis.

### **Future Direction**

- Improve accuracy of strain measurements for Mg alloys.
  - Integrate faster high-speed video into measurement system.
  - Test and improve method for interrupted strain-rate tests.
-

## **Introduction**

The low density and excellent machinability of Mg alloys make them good candidates for light-weight construction of automotive components. However, they also exhibit much more complex mechanical behavior than more common automotive materials. The mechanical response of Mg alloys involves notable anisotropy, nonisotropic hardening, yield asymmetry, lower ductility than other automotive materials, and significant degradation of effective properties due to formation and evolution of microdefects.

Figure 1 shows a Mg alloy tube being crushed at 0.5 m/s. The intense fracturing is notably different behavior from the progressive folding observed in conventional automotive steel structures and requires in-depth material and structural understanding for automotive application.

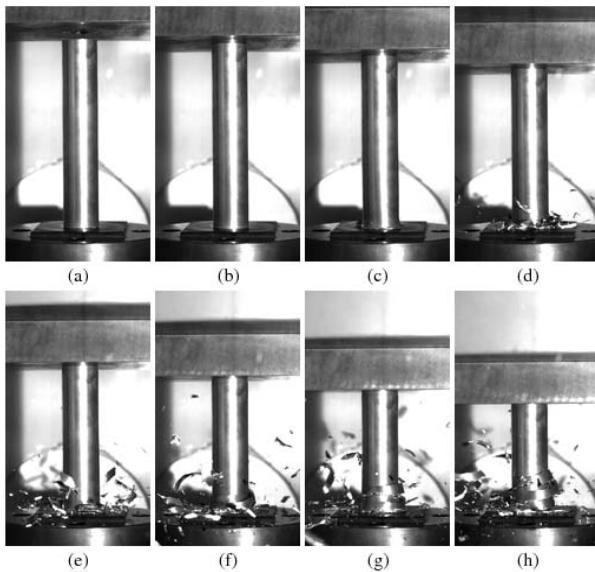


**Figure 1.** Crush of Mg alloy tube at 0.5 m/s.

Accordingly, the necessary characterization procedures and constitutive models are more complex than commonly used uniaxial tests and isotropic plasticity for steel. Another issue of concern for automotive designers is the strain-rate sensitivity of various properties of Mg alloys. Preliminary tests indicate there is significant strain-rate sensitivity in certain Mg alloys. In Mg alloys, strain-rate sensitivity is manifested by an increased hardening rate that is beneficial for diffusing and postponing the onset of localization and fracture. However, the lack of strain-rate

sensitivity information coupled with the lack of understanding of loading-induced property degradation for Mg alloys adds to the concerns typically associated with using a new material. The strain-rate sensitivity in Mg alloys is not only linked to yield strength but to other effective material properties such as effective elastic modulus, while internal structure evolution is important to the onset of ductile fracture. Experiments on several wrought and cast Mg alloys reported in the literature show the considerable effect of manufacturing conditions on alloy properties. Correlation of the properties of Mg alloys in manufactured parts with those of specimens made under optimal conditions is needed to avoid lengthy testing for numerous manufacturing situations.

## **Technical Approach**

In support of the U.S. Automotive Materials Partnership project AMD604, Magnesium Front End Research and Development, we are investigating rate-dependent properties of automotive Mg alloys. The results will be used in the framework of different modeling approaches such as continuum damage mechanics and mechanics of plastic voided solids. The experiments are conducted under various strain rates ranging from quasi-static to rates of 500/s on the same equipment. The main scientific and technical advances anticipated are (1) the development of detailed information about Mg alloy response to impact loading, (2) characterization of property degradation by the control of imparted strain for high strain rates that will allow for detailed investigation of evolution of internal state as a function of loading rate, (3) development of tightly controlled compressive and shear high-speed tests, and (4) correlation of manufactured and ideal material properties.

The deliverables for the project are the documented rate-sensitive properties for the selected Mg materials, microstructural characterization and damage data from the tests, and material model data for selected constitutive model formulations.

### High-Strain-Rate Experiments

During fiscal year 2008, we conducted several preliminary experiments and compiled them into an interactive database that is accessible over the World Wide Web ([http://thyme.ornl.gov/Mg\\_Main/description](http://thyme.ornl.gov/Mg_Main/description)). The home page for the database is shown in Figure 2.

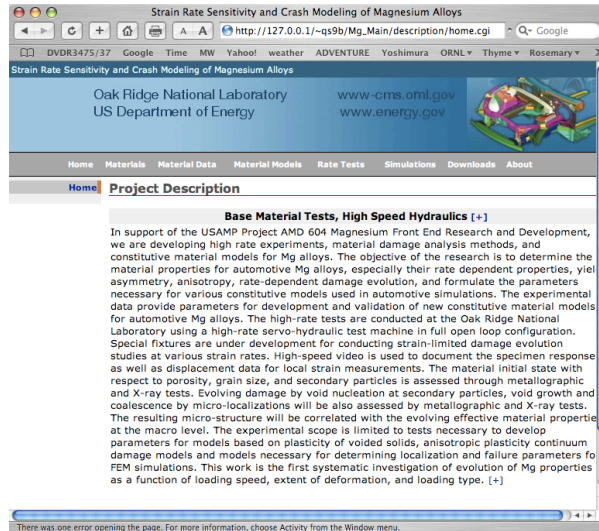


Figure 2. Home page for Mg alloy tests database.

The web interface allows for experimental data to be integrated with the other project components and provides mechanisms for data analysis and collaboration between project participants.

### Tensile High-Strain-Rate Tests on Hydraulic Equipment

For tensile loading, different variations of the dog-bone style tensile specimen configurations for sheet and solid materials are used (see specimens from laboratories labeled B and C from reference [2]). Specimens are machined to accommodate a strain gage attachment in the load measurement section for sheet specimens. A similar arrangement is used for testing bar specimens from cast samples. Figure 3 is a schematic for sheet tensile tests.

Tests are conducted at six actuator speeds to achieve strain rates of quasi-static (0.001/s), 0.1/s, 1/s, 10/s, 100/s, and maximum strain rates on the order of 500/s. At high loading speeds, specimen gage lengths are shortened to provide sufficient time for specimen equilibration under the highest

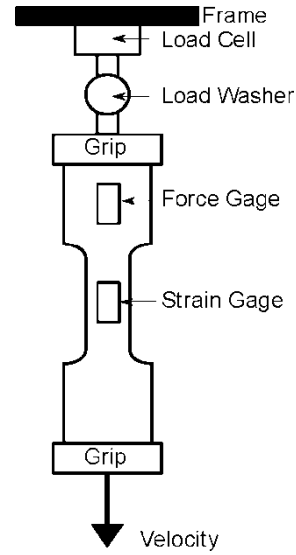


Figure 3. Tensile specimen configuration.

loading speeds [2, 3]. A slack adapter is incorporated in the load train and its initial position controlled to allow the actuator to reach constant velocity before the specimen is loaded. Also, low mass grip concepts are used to minimize inertia effects and machine resonance on the measured specimen response.

The instruments listed below are used for measurement of forces, displacements, stresses, and strains. Tests at rates higher than 1/s will be recorded with high-speed video. To ensure consistency among the various test rates, several lower-rate tests are recorded during the test development.

Forces are measured by the following.

1. Strain gage, full bridge DC load cell.
2. Piezoelectric load washer.
3. Calibrated strain gage on the specimen tab [3].

Strains are measured by the following.

1. Actuator displacement.
2. Optical measurements from high-speed video.
3. Strain gages located in the test gage region.

Multiple measurement of both forces and displacements allows for correlation of the results and verification of the methods.

## Characterization of Damage Evolution in Mg Alloys

For realistic description of the mechanical response of Mg alloys and to characterize the onset of failure it is essential to identify and understand the initiation and progression of damage leading to material property degradation, instability, and failure. To this end, test methods must be able to incrementally load specimens to intermediate levels on the stress-strain curve and evaluate the magnitude of the damage evolution at each level. To accomplish this task at high strain rates, novel test fixtures must be used to limit strain and/or load levels for a series of single specimens and evaluate the damage state using microscopy/metallographic techniques on the sectioned specimens.

Figure 4 schematically depicts the method to introduce a desired strain level at high rate [4] into a specimen by attaching a strengthened pull-rod to the bottom end of the specimen with a mechanical fuse. The pull-rod passes through a hole in the fixed plate and is attached to the test machine actuator. When the actuator moves downward, the specimen elongates until it contacts the fixed rigid plate and the mechanical fuse breaks and detaches from the specimen.

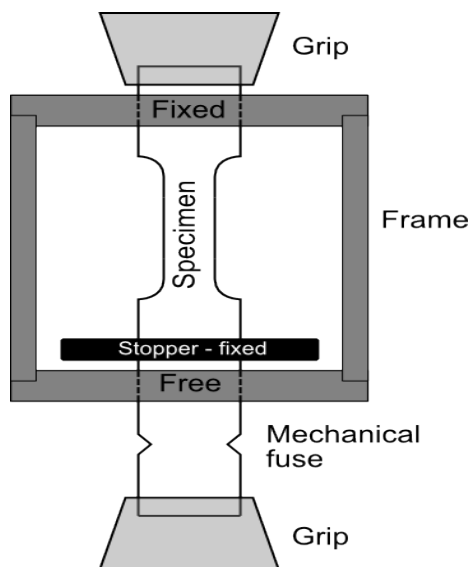


**Figure 4.** Strain-limiting fixture schematic.

We have designed a preliminary fixture based on the above idea and adapted it to the current high-speed testing setup. The fixture design will be further evolved as we conduct the tests and develop more experience with the process.

Material damage will be assessed through measurement of effective elastic modulus, and measurement of evolving microstructural features (e.g., void distribution and size) will be accomplished through a combination of metallographic and X-ray examinations. Evolving stages of damage (e.g., void nucleation, void growth, and void coalescence) will be characterized.

## Conclusions

A new project for characterization of strain-rate sensitivity of Mg alloys under automotive strain rates has been initiated. The test methods are being modified to account for characteristic Mg response under impact conditions. When fully developed, the tests will provide needed data for more effective design with Mg alloys and lightweight automotive designs.

## Future Work

Future project tasks include the following.

1. Specimen design for high-rate tests for Mg alloys.
2. Refinement of the interrupted strain-test method.
3. Development of high-strain-rate tests for compression and shear.
4. Measurement of material properties for Mg alloys.
5. Measurement of evolving damage in Mg alloys under loading.
6. Constitutive models for Mg alloys.

## References

1. E. A. Nyberg, A. A. Luo, and K. Sadayappan, "Magnesium for Future Autos, Advanced Materials, and Processes," ASM International, October 2008, pp. 35–37 (2008).
2. C. Wong, "IISI-AutoCo Round-Robin Dynamic Tensile Testing Project, International Iron and Steel Institute," 2005.



3. D. Matlock and J. Speer, "Constitutive Behavior of High Strength Multiphase Sheet Steels Under High Strain Rate Deformation," AISI/DOE Technology Roadmap Program, Report TRP 9904, 2005.
4. Choi et al., "Strain Control during High Speed Tensile Testing," *Journal of Testing and Evaluation*, **34**(5), pp. 1–4 (September 2006).

## **F. High-Rate Damage and Fracture, Experimentation, Simulation, and Visualization**

*Principal Investigator: Philip Gullett*

*Assistant Professor, Civil and Environmental Engineering  
Mississippi State University  
Walker Bldg., Rm. 235 M  
Mississippi State, MS 39762  
(662) 325-5486; fax: (662) 325-7189; e-mail: pmgullett@enr.msstate.edu*

*Co-Principal Investigator: Mark F. Horstemeyer*

*Center for Advanced Vehicular Systems Chair in Solid Mechanics and Professor, Mechanical Engineering,  
Mississippi State University  
206 Carpenter Bldg., PO Box ME  
Mississippi State, MS 39762  
(662) 325-7308; fax: (662) 325-7223; e-mail: mfhorst@me.msstate.edu*

*Co-Principal Investigator: Tomasz Haupt*

*Center for Advanced Vehicular Systems, Mississippi State University  
Box 5405  
Mississippi State, MS 39762  
(662) 325-4524; fax: (662) 325-5433; e-mail: haupt@cavs.msstate.edu*

*Research Associate II: David Oglesby*

*Center for Advanced Vehicular Systems, Mississippi State University  
200 Research Blvd.  
Mississippi State, MS 39762  
(662) 325-6854; fax: (662) 325-5433; e-mail: doglesby@cavs.msstate.edu*

*Co-Principal Investigator: Srdjan Simunovic*

*Oak Ridge National Laboratory  
P.O. Box 2008, Oak Ridge TN 37831-6164  
(865) 241-3863; fax: (865) 241-0381; e-mail: simunovics@ornl.gov*

*Co-Principal Investigator: J. Michael Starbuck*

*Oak Ridge National Laboratory  
P.O. Box 2008, Oak Ridge, TN 37831-6053  
(865) 576-3633; fax: (865) 574-8257; e-mail: starbuckjm@ornl.gov*

*Co-Principal Investigator: Don Erdman*

*Oak Ridge National Laboratory  
P.O. Box 2008, Oak Ridge, TN 37831-6091  
(865) 576-4069; fax: (865) 574-0641; e-mail: erdmandl@ornl.gov*

*Technology Area Development Manager: Joseph A. Carpenter*

*(202) 586-1022; fax: (202) 586-1600; e-mail: joseph.carpenter@ee.doe.gov*

*Field Technical Manager: Philip S. Sklad*

*(865) 574-5069; fax: (865) 576-4963; e-mail: skladps@ornl.gov*

---

Contractor: Mississippi State University (MSST)  
Contract No.: 4000054701

---

### **Objective**

- Evaluate the strain rate failure of AZ31 magnesium (Mg) for various stress states.
- Develop a damage model for stress-state dependence of dynamic damage evolution.
- Evaluate numerical procedures for the modeling of monotonic fracture of Mg.

### **Approach**

- Characterize material behavior using split-Hopkinson pressure bar (SHPB) experiments in compression, tension, and torsion.
- Characterize damage nucleation using molecular dynamics.
- Develop damage-evolution-based fracture.

### **Accomplishments**

- Examined anisotropic, high strain rate compression, metallurgical evaluation, of Mg AZ31.
- Evaluated the effects of grain orientation and stress states on void nucleation at triple junctions in aluminum (Al) using molecular dynamics.

### **Future Direction**

- Complete high strain rate torsion and tension testing of AZ31.
- Develop a void nucleation model based on nanoscale simulations.
- Implement microstructure-property damage-based fracture criteria in fracture-simulation code.

---

### **Introduction**

This report summarizes the state of the experimental and numerical simulation study of fracture mechanisms in metallic alloys at various size scales. This is a joint effort between Oak Ridge National Laboratory and MSST. The aim is an enhanced, multiscale microstructure-property model that can be implemented into commercial codes and be used in high-fidelity crash simulations for the design and optimization of structural Mg components. The development effort will focus on the AZ31 Mg alloy, and a complementary experimental effort will provide experimental data for other Mg alloys that can be used for the development of microstructure-property model parameters.

### **Experimental Results: Anisotropic Response of AZ31B**

The anisotropic response of AZ31B under high-rate compressive loading has been examined. To fully quantify the effect of the loading orientation and strain rate on the stress-strain behavior of AZ31B, compression tests at quasi-static and high strain rates were performed in all three directions as indicated by Figure 1. All of the specimens were tested to fracture. The specimens were obtained from an as-received 19.05 mm thick plate in the H24 condition. Tests under quasi-static conditions were performed using an Instron 5882 electromechanical machine under constant strain rate controlled at 0.001/s. The high strain rate tests were conducted using a maraging steel SHPB apparatus.

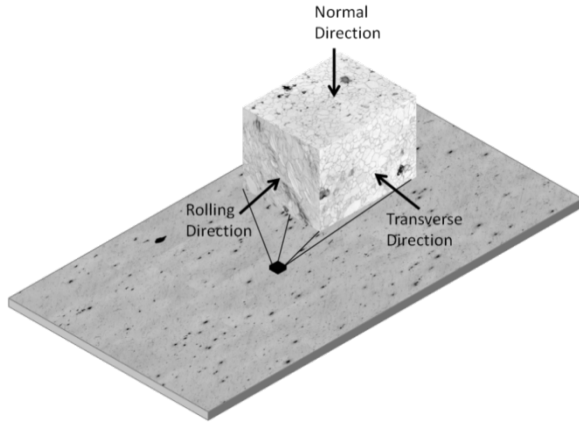


**Figure 1.** Orientations of testing and microstructural analysis relative to the as-received AZ31B plate.

Figure 2 shows the results of tests performed at quasi-static ( $10^{-3}$ /s) and high strain rates (3,400/s–4,300/s). When tested in the normal or short transverse direction, a strong rate dependence on the yield strength was evident. The initial hardening rate at high strain rate was similar to that at quasi-static rates, but the high strain rate specimen began to exhibit softening at a strain of approximately 0.08 which continued until the specimen fractured at a strain of approximately 0.18. This constituted a significant increase in the strain-to-failure compared to the quasi-static conditions and is likely due to either thermal softening or the onset of dynamic recrystallization during the adiabatic conditions of the high-rate test.

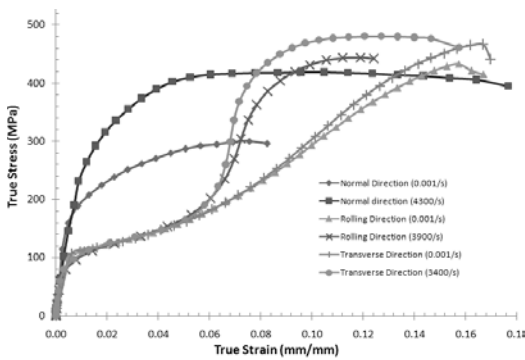
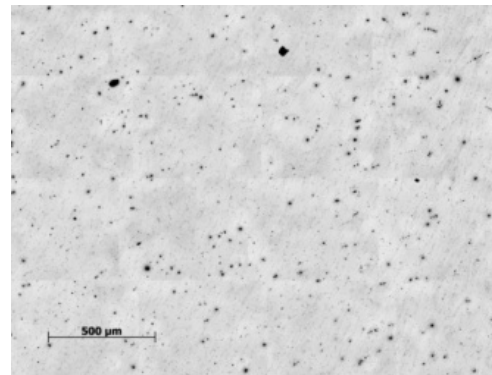


**Figure 2.** Compressive stress–strain behavior of AZ31B-H24 showing the anisotropic effects on the strain rate dependence.

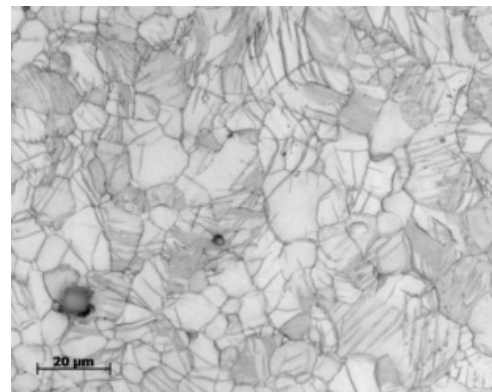
Microstructural analysis was conducted on the specimens before and after each test and image

analysis was conducted to calculate the particle-size distribution, the particle nearest-neighbor distance distribution, the aspect-ratio distribution, and the total particle area fraction. The number and percentage of fractured particles was also determined. Each specimen was then etched so that grain size and twin density analysis could be performed.

Figure 3 shows optical microscope images of the polished and etched specimens. This particular specimen was oriented in the normal direction and tested in quasi-static compression. Note that image 3(a) is a mosaic of 16 smaller images so that a representative area could be analyzed. The grain



(a)



(b)

**Figure 3.** Specimen images after quasi-static compression orientated in the normal direction. Figure 3(a) shows the specimen after polishing and before etching to allow for the characterization of the parameters related to the second-phase particles. Figure 3(b) shows the same specimen after etching with grain boundaries and deformation twins evident. Note the difference in scale.

size, particle information, and twin information were each averaged from a total of nine individual images that were separately analyzed. Analysis indicates that energy absorption increased with an increased strain rate in the normal direction while the energy absorption in the rolling and transverse directions was within the level of testing uncertainty. The level of strain-to-failure increased as the strain rate increased in the normal direction; however, the strain-to-failure slightly decreased in the rolling and transverse directions as the strain rate increased. The twin density and particle fracture density increased as the strain rate increased in all three orientations.

### **Nanoscale Simulation: Void Nucleation Modeling and Visualization**

Isolated triple junctions in Mg have been examined using molecular dynamics to determine the effects of grain orientation and stress states on void nucleation. A pseudo-two-dimensional system isolates a single triple junction and examines the factors controlling void nucleation. Each simulation consists of three grains in a simulation cell of  $40 \text{ nm} \times 40 \text{ nm} \times 2.3 \text{ nm}$  with  $\sim 250,000$  atoms (see Figure 4).

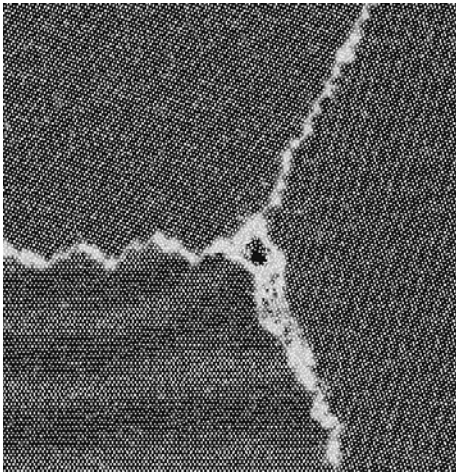


**Figure 4.** Atomic structure and centro-symmetry values of triple junction that nucleated a void.

The atoms comprising the exterior boundary are held fixed in the direction of the surface normal but are allowed to move in the direction of the thickness to accommodate Poisson effects. A total of 15 different initial structures are examined with

grain orientations incremented in  $15^\circ$  counter-clockwise rotations about the z-axis from the reference orientation,  $0^\circ$ , defined as  $x = (\bar{1}10)$ ,  $y = (010)$  and  $z = (110)$ . Since all grains will have a common  $(110)$  texture, each grain in effect is a columnar structure with four active slip systems capable of capturing the necessary plasticity for this length scale. The grains are loaded by applying a constant strain rate of  $10^{10}/\text{s}$  in the x and y directions. The modified embedded-atom method (MEAM) is used to determine the energetics of the Al-Al interaction.

The focus of this work is to study void nucleation; thus, we will begin with examining only biaxial loading since it has previously been shown that loading atomistic triple junctions uniaxially will result in significant plasticity and no void nucleation up to 30% strain. For all simulations loaded biaxially, voids begin to nucleate at stresses of  $\sigma_{xx} = \sigma_{yy} \approx 6\text{--}7 \text{ GPa}$  and strains of  $\epsilon_{xx} = \epsilon_{yy} \approx 6.7\text{--}7.8\%$ . Only 2 of the 15 simulations nucleate voids directly at the triple junctions and the others nucleate voids along one of the three grain boundaries. At this point there is no clear grain boundary characteristic that leads to the failure of one particular grain boundary over another. Yet for the case of adjacent grains with orientations of  $0^\circ$  and  $30^\circ$ , a  $(233)/(211)$  grain boundary forms and is always the location for void nucleation independent of the other two boundaries. This boundary is not a perfect  $(233)/(211)$  boundary as a result of the method used to generate the initial structures, but it does have similar characteristics. One characteristic of this particular grain boundary is that there is a larger amount of “free volume” located along the  $(233)/(211)$  boundary relative to the others.

The centro-symmetry parameter measures the degree of local shear and disorder, which is similar to the local volume increase associated with nonhydrostatic stresses. The centro-symmetry values further show that the grain boundaries that nucleate voids tend to have larger local free volumes relative to the other grain boundaries. This simple visual analysis requires more quantitative support, which will be performed soon.

While analysis of grain orientation on void nucleation is critical, the stress-state dependence is also very important. It is well documented that a critical factor of void nucleation and void growth is triaxiality. Here triaxiality is defined as the hydrostatic/mean stress divided by the von Mises/effective stress,

$$\chi = \sigma_m / \sigma_{eff} ,$$

for a perfect biaxial loading  $\chi = 0.67$  and approaches infinity for a perfectly hydrostatic loading.

To elucidate stress-state dependence a single simulation, which nucleated a void at the triple junction, is selected and deformed under several different stress states. The results of varying the stress triaxiality on the strain to failure, or the strain to nucleate a void, are shown in Figure 5. As expected, the strain to failure increases with decreasing triaxiality. For the (110) texture, at higher triaxiality slip is inhibited because of low shear stresses that do not activate the slip systems. Slip and dislocation activity is the natural form of dissipation in a metal; if critical tensile stress is necessary for void nucleation and dislocations reduce the stress in the system, some sort of hardening must occur at higher strains in order to reach the critical stresses necessary for void nucleation. For the highest triaxiality,  $\chi = 35$ , the remote hydrostatic stress is  $\sim 8$  GPa. This high triaxiality case has nearly homogenous stress throughout the simulation, which means this is most

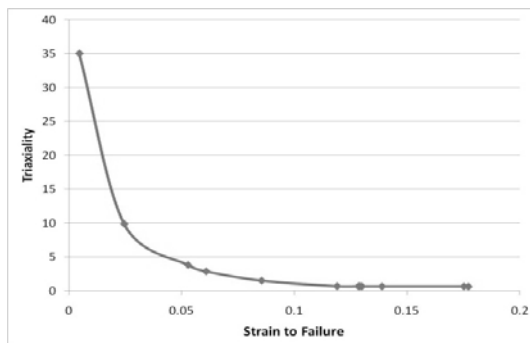


**Figure 5.** Graph of stress triaxiality vs the strain to failure or strain to void nucleation. The higher the triaxiality the lower the strain to failure and vice versa.

likely the critical hydrostatic stress necessary for void nucleation. In the cases with lower triaxiality, it is necessary to increase the local stress near the point of void nucleation.

To completely understand the void nucleation, an analytic model should be developed to describe the energetics of the system. This model will focus on the simulations that do not nucleate any dislocations before void generation,  $\chi > 0.5$ . The simplest system to study is the purely biaxial case,  $\chi = 0.67$ , beginning by analyzing the elastic response of this particular case. Since Al is fairly isotropic, the stress strain curves for all 15 grain orientations under biaxial stress lie relatively on top of each other up to failure. Since all of the stress strain curves are similar, the same orientation used in Section 2 is selected for analysis. The first step is to capture the elastic response under different stress states.

Applying Hooke's law reproduces the elastic regions of all the stress strain curves for varying triaxialities. Following the elastic analysis a yield/nucleation criterion must be developed. The yield/nucleation criterion has not been developed, yet, but is being considered.

### **Macroscale Modeling and Visualization**

Visualization of fracture propagation is complete. The previous visualization tool only allowed analysis of an individual step, while the revised implementation displays evolution of all field values throughout the simulation history. This was accomplished through integration with the visualization software EnSight, which was chosen due to its robustness and portability. The framework was established that will allow the user to view various entities as the simulation progresses.

This particular example is of a compact specimen with the properties of steel being pulled in the top hole upward and the bottom hole downward, each with the same amount of force (Figure 6). The top and bottom right corners of the specimen are fixed in the horizontal direction, and the midpoint of the right side is fixed in the vertical direction.

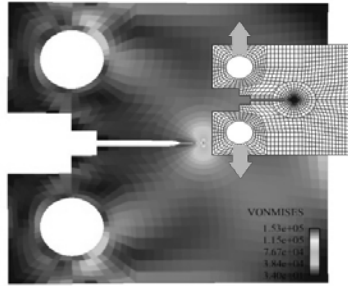
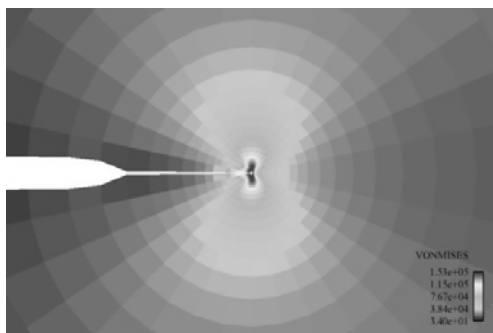
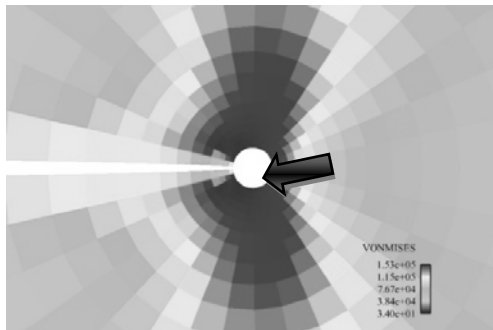


**Figure 6.** The loading of a compact tensile specimen is shown. Color variation reflects the von Mises stress level. Note the highly localized stress gradient near the region of the crack tip.

Figure 7 shows the von Mises stress levels near the crack tip. The steep stress gradients are resolved by a high resolution mesh that follows the crack as it grows through the specimen. At that tip of the crack [Figure 7(b)] is an “exclusion



(a)



(b)

**Figure 7.** Steep stress gradients are resolved by a high resolution mesh that follows the motion of the crack tip. The circular zone at the tip of the crack, called the “Exclusion Region,” is modeled independently, allowing for physically based fracture criteria, including lower scale simulations.

region” in which crack growth may be modeled using a variety of physically based models. Fracture modeling may be performed using a concurrent multiscale approach in which microstructural details are used to establish crack direction and extension. Information is passed between the exclusion region and the standard finite-element mesh by a weak momentum balance between the exclusion region and the surrounding finite elements. Current efforts are focused on implementation of the microstructure-property and damage model into the simulation frame work.

**Conclusions**

We have completed high-rate testing of AZ31 Mg in compression and have begun testing in torsion. Once testing is completed, modeling of the behavior will be incorporated into our existing multiscale, microstructure-property model. Simulations of void nucleation have provided detailed information related to the nucleation of voids at triple points. Data will be incorporated into the nucleation term of the damage model. The damage model is currently being incorporated into the fracture simulation code. Once this has been completed, fracture simulations will be evaluated against experimentally observed results.

**Presentations/Publications/Patents**

Matthew T. Tucker et al., “Anisotropic effects on the strain rate dependence of a wrought magnesium alloy,” *Scripta Materialia*, **60**(3), pp. 182–185 (2009).

## **G. Integrated Computational Materials Engineering for Magnesium in Body Applications (Mg ICME) (AMD702 and 703\*)**

*Principal Investigator: John E. Allison*  
*Ford Motor Company Research and Innovation Center*  
*Mail Drop 3182*  
*2101 Village Road*  
*Dearborn, MI 48124*  
*(313) 845-7224; fax: (313) 323-1129, e-mail: jalliso2@ford.com*

*Program Technical Administrator: Robert C. McCune*  
*Robert C. McCune and Associates, LLC*  
*5451 S. Piccadilly Cir.*  
*West Bloomfield, MI, 48322-1446*  
*(248) 661-0085, fax: (248) 661-8718, robert.mccune@sbcglobal.net*

*Technology Area Development Manager: Joseph A. Carpenter*  
*(202) 586-1022; fax: (202) 586-6100; e-mail: joseph.carpenter@ee.doe.gov*

*Field Project Officer: Aaron D. Yocum*  
*(304) 285-4852; fax (304) 285-4403; email: aaron.yocum@netl.doe.gov*

---

*Contractor: United States Automotive Materials Partnership (USAMP)*  
*Contract No.: FC26-02OR22910 through the National Energy Technology Laboratory*

---

### **Objectives**

The primary goal of this project is the development of an Integrated Computational Materials Engineering (ICME) infrastructure for optimization of magnesium (Mg) manufacturing processes and automotive body components and for Mg alloy development. This is a key enabling technology for future Mg applications, including the Mg front-end architectures of companion programs AMD603—Magnesium Front End Design and Development (MFEDD) and AMD604—Magnesium Front End Research and Development (MFERD). The following are specific objectives.

- Establishment of an international ICME infrastructure (including contributor network, knowledge-base, and cyberinfrastructure) for Mg alloys in automotive structural body applications, specifically:
  - Product and manufacturing process optimization (processes include extrusion, sheet forming, and high-pressure die casting)
  - Microstructural engineering
  - Future alloy development
- Development of a web-based cyberinfrastructure to serve as a hub for exchanging high quality data and models between global collaborators in academia and industry.
- Use ICME infrastructure for MFERD Phase II product and process optimization.
- Attract materials researchers into the Mg field and leverage their efforts by providing a collaborative, virtual workplace for coupling high-quality data and models.

---

\*Denote projects 702 and 703 of the Automotive Materials Division of the United States Automotive Materials Partnership, one of the formal consortia of the United States Council for Automotive Research set up by Chrysler, Ford, and General Motors to conduct joint, precompetitive research and development (see [www.uscar.org](http://www.uscar.org)).



- Advance scientific understanding in various aspects of Mg cast and wrought alloys for structural body applications including development of quantitative processing-structure-property relationships for crash energy management and fatigue performance as well as design optimization.
- Incorporate the contributions of high-quality professionals and students educated in materials science and engineering in the U.S., Canada, and China.

## Approach

The project is divided for contractual purposes into two separate projects, AMD702 and AMD703, within the Automotive Metals Division of USAMP. AMD703 is a conventional USAMP project, funded by the Automotive Lightweighting Materials technology area of DOE, and subject to the cooperative agreement between the organizations. In AMD702, work conducted by USAMP Original Equipment Manufacturer (OEM) companies is provided on an “in-kind” basis in support of a separate DOE cooperative agreement with Mississippi State University (MSST), wherein ICME is only one part of a broader research agenda. In addition, DOE is directly funding Mg diffusion research at Oak Ridge National Laboratory (ORNL). The overall ICME for Mg in Body Applications (Mg ICME) project is structurally linked to AMD604 which has a Phase 1 duration of 3 years; however, the initial projected duration of the Mg ICME Project is 5 years. The USAMP Mg ICME project is an integral component (Task 1.9) of the Three Countries (USA, China, Canada) Mg Front End Research and Development (MFERD) enabling technologies project. The plan of work is outlined as follows.

- Develop a web-based electronic “community of practice” allowing development and integration of multi-scale, physics-based, open-source materials models for selected properties and processes.
- Establish and verify a web-accessible, “first principles” and calculated phase diagram (CALPHAD)/diffusion database and computational infrastructure. Development of a user-friendly extensible, self-optimizing phase equilibrium program and graphical user interface (GUI) for a wide range of wrought and cast Mg alloys.
- Establish physics-based and/or empirical relationships for microstructural evolution and similarly-based relationships between microstructures and mechanical response of materials under stress in tension, compression (at varying strain rates), and fatigue loading. This formalism would apply to:
  - Extruded Mg components
  - Sheet Mg components
  - High-integrity, high-pressure die-cast Mg components
- Establish and demonstrate the capability for multi-attribute optimization. Demonstrate the capability to optimize Mg alloys, processes, and components for cost and performance on one or more extruded components. Extend such capability to MFERD Phase II efforts (should they occur).
- Coordination, information dissemination, and reporting. Establish overall coordinated work structure between AMD702, AMD703, AMD604 and Canadian and Chinese suppliers involved in the Three Countries MFERD Program.

## Accomplishments

USAMP AMD 702/703, Integrated Computational Materials Engineering for Mg in Body Applications, was approved by USAMP on February 14, 2007. Accomplishments for the included time period of this report (October 1, 2007–September 30, 2008) are summarized as follows.

- The project “kick-off” meeting was held at USCAR in Southfield, MI, January 29, 2008. Details of this meeting are posted on USCAR Vroom web site for USCAR partners.
- The first Project Review meeting was held August 27, 2008, at USCAR.
- Detailed program plans, work statements, and USAMP contracts for all participants were developed, including:
  - Three U.S. universities contributing specifically to AMD703 (Northwestern, University of Michigan, and University of Virginia)
  - Mississippi State University (MSST) via AMD702

- Four companies or other organizations contributing to AMD703 (MaterialsGenome, TMS (The Mining, Metals and Materials Society), Thermo-Calc, Magma Foundry Technologies)
- Legal agreement between USAMP and MSST was completed.
- Interdependent plans with Canadian and Chinese participants were developed via MFERD Task 1.9.
- Magnesium alloys were identified for ICME developments (AZ91D—casting, AM30—extrusion and AZ31—sheet).
- Materials for experimental work at various universities were obtained and distributed. (e.g., super vacuum die-cast “shock towers” for University of Michigan.)
- MSST SharePoint web site became operational (March 2008) and was announced at the Hangzhou meeting in China in April 2008.

### **Future Direction**

- Continue to define appropriate initial examples and populate the SharePoint web-based “cyberinfrastructure” platform at MSST.
- Provide high quality materials (e.g., super vacuum die castings, extrusions, sheet) for analysis.
- Demonstrate linkage between first-principles calculations, calculated phase diagrams, and microstructural evolution.
- Make significant progress in developing quantitative processing-structure-property relationships for Mg extrusions, sheet formed parts, and super vacuum die casting (SVDC) castings.
- Convene two review meetings of project participants in spring and late-summer 2009 time frame.
- Strengthen international collaboration via careful planning, frequent electronic networking, and next annual meeting at Niagara-on-the-Lake, Ontario, Canada (May 2009).

### **Introduction**

The background for the Mg ICME project was discussed in the 2007 Annual Report to DOE [1]. Additionally, a broader review of ICME principles and approach has recently been prepared by the National Research Council [2]. The focus of this progress report will be on the accomplishments of USAMP Projects AMD702 and AMD703 during the federal fiscal year 2008 period from October 2007 through September 2008.

In the sections that follow, the overall project status is first reviewed, followed by specific sections devoted to the accomplishments of the individual Task areas during the reporting interval.

### **General Project Accomplishments for the Reporting Period**

All organizational and contractual aspects of the project as pertain to the participants, suppliers, and relationship between USAMP and Mississippi State University (MSST) are now complete. The

working agreement with MSST was approved by all parties on February 27, 2008. The USAMP project “kick-off” was held at USCAR on January 29, 2008, and the first collective review meeting was held on August 27, 2008. Details of these meetings may be found either on the USCAR ‘Vroom’ web site (for USCAR and DOE partners only) or on the Mississippi State University SharePoint web site [3] for the three countries participants. An ICME project is also part of the U.S.-Canada-China MFERD project as international Task 1.9, and results of that work have been reported in the project annual review [4].

The following sections detail accomplishments in the various project tasks over the reporting period.

### **Task 1 Cyberinfrastructure**

#### **Mississippi State University**

MSST is responsible for establishment of the Mg ICME Cyberinfrastructure. MSST presently hosts

two independent portals: one for project information sharing for the overall Three Countries MFERD Project, and the other for specialized purposes of the Mg ICME task. The ICME portal will enable sharing scientific data and models between the project participants in the USA, Canada, and China. The MSST Cyberinfrastructure development leader attended the MFERD meeting in Hangzhou, China, and conducted discussions on the requirements for the Cyberinfrastructure for the overall MFERD project and for the ICME task. The SharePoint server at MSST has been filled with content, in collaboration with Eric Nyberg (PNNL) and Robert McCune (USAMP), who are managing the Web Sites for MFERD and ICME, respectively. Eventually, the server will provide a single point of access to all services rendered by the cyberinfrastructure, through the contents aggregation. The current and future activity focuses the maintenance of the servers. As of October 2008, the MFERD/ICME (<http://carload.hpc.msstate.edu>) portal has 100+ registered users from USA, Canada, and China.

Development of specific services supporting online repository of material properties, design optimizations, and multiscale simulations: A repository of material properties has been developed and made available to test users (both at MSST and ICME).

The repository is online at <http://cgg.hpc.msstate.edu/ccgportlets> and through the ICME site. The repository comprises a database of experimental data (stress-strain, strain-life, and microstructure images), a database of material constants (for damage and multistage fatigue models), and is seamlessly integrated with online tools (Damage Fit, Multistage Fatigue Fit, and Microstructure Analyzer) for extracting the material constants from experimental data. The seamless integration means a full support for searching experimental data directly from the tools interfaces, transferring analysis results from one tool to another (e.g., grain statistics to damage or fatigue model), and storing the analysis results into the material constants database so that they can be retrieved a latter time, perhaps by a different user, and formatted according to specification of a finite-

element analysis (FEA) application, such as the commercial program ABAQUS.

In summary, a basic infrastructure has been created that forms a solid foundation for creating the cyberinfrastructure for engineering virtual organizations. During 2008, the infrastructure has been used to develop and deploy two integrated applications: the repository of material properties and FAME (a system for adaptive metamodeling).

### **The Minerals, Metals and Materials Society (TMS)**

As a professional society, TMS is providing programming and a web-based portal to aid in the creation of a communications network among professionals dedicated to the subject matter of Mg science and technology and ICME. A special joint symposium with the American Physical Society regarding this topic was conducted at the 2008 TMS Annual Meeting [5]. The TMS website presently contains links to Mg and ICME [6].

### **Task 2 Calculated Phase Diagrams (CALPHAD), Diffusion Infrastructures and Database**

#### **Northwestern University**

The first-principles portion of this project focuses on phases relevant to precipitation in the AZ91 (Mg-Al-Zn) example system. Work to date has concentrated on phase stability, defects, and site substitution in the  $Mg_{17}Al_{12}$  ( $\beta$ ) phase, which is significant for this particular alloy. These calculations should aid in more predictive, physics-based CALPHAD thermodynamic database construction. Additionally, calculation of key unknown parameters related to Mg diffusion (e.g., solute-vacancy binding across a wide variety of solutes) is being conducted in order to help construct better diffusion databases for Mg alloys.

#### ***a. First-principles study of $\beta$ -Mg<sub>17</sub>Al<sub>12</sub> phase.***

Previous experimental observations have shown that the solubility of  $\beta$ -Mg<sub>17</sub>Al<sub>12</sub> extends to Mg-Al-Zn, thus Zn has to be introduced in the sublattice model within the CALPHAD framework. First-principles calculations of end-members in the  $\beta$ -phase for the Mg-Al binary system show good agreement with previous

CALPHAD databases (which were fit to first-principles data). However, in the Mg-Al-Zn system, the addition of Zn to the end-member energetic for  $\beta$  show that the most recent CALPHAD assessment needs to be further improved. Table 1 shows these end member energetics, and should be useful in constructing a new CALPHAD description of  $\beta$ .

**Table 1.** Comparison of formation enthalpies for selected end members of the  $\beta$ - phase as calculated by first principles and by CALPHAD

$\Delta H_f$ (end-members)	First-principles (J/mol)	CALPHAD (J/mol)	Difference (J/mol)
Mg <sub>17</sub> Zn <sub>12</sub> (Mg:Mg:Zn)	-8051	-5000	3051
Mg <sub>22</sub> (Mg:Mg:Mg)	4490	4602	112
Mg <sub>2</sub> Zn <sub>24</sub> (Mg:Zn:Zn)	-5879	10000	15879
Mg <sub>17</sub> Zn <sub>12</sub> (Mg:Zn:Mg)	1127	3000	1873

**b. Defects and off-stoichiometry of  $\beta$ -Mg<sub>17</sub>Al<sub>12</sub>.** Additionally, a calculation of off-stoichiometric defects of  $\beta$ -Mg<sub>17</sub>Al<sub>12</sub> in binary and ternary systems has been initiated. These defect energies will be used to understand the unusual asymmetry of the phase boundaries in Mg-Al, and will aid in future CALPHAD database construction. Native point defects, i.e., vacancy and anti-sites in  $\beta$ -Mg<sub>17</sub>Al<sub>12</sub>, have been calculated and are shown in Figure 1.

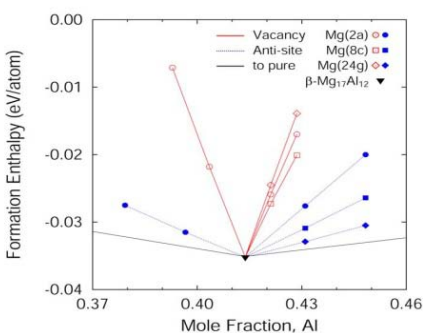


**Figure 1.** Calculated native point defects in  $\beta$ -Mg<sub>17</sub>Al<sub>12</sub>.

### MaterialsGenome, Inc.

During this reporting period, the data infrastructure for storing input data used for thermodynamic modeling and output data was established, and the feasibility of this data structure to be implemented by database software (e.g., SQL) was demonstrated. Figure 2 shows the

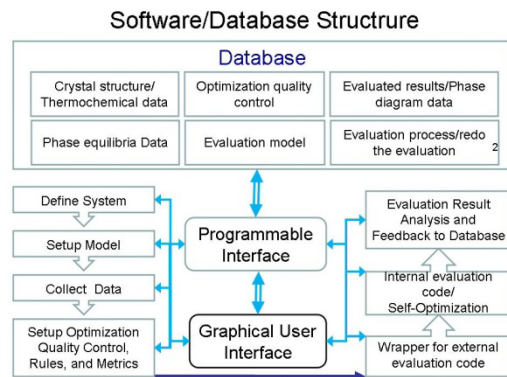


**Figure 2.** Organization of database structure for thermodynamic data.

overall structure of the software/database to be developed in this project. In the database, crystallographic, thermochemical, and phase-equilibrium data based on available measurements and predictions will be collected and stored. Additionally, the most common or frequently used thermodynamic models will be stored in the database. Secondly, rules for optimization quality control, e.g., the weight of each thermodynamic datum and the optimization order during thermodynamic modeling will be established. There rules are heuristic and will be treated as part of the database. Thirdly, the key data created in the optimization processes will also be saved in the database in order to redo or continue a selected thermodynamic model. Finally, the modeled results, i.e., the self-consistent thermodynamic functions, will be stored. In the GUI part, the user has the option to connect the whole database and change partial data through the database management. The GUI will let the user model a system (e.g., Al-Mg, Al-Mg-Zn, etc.) based on available thermodynamic and crystallographic data. As shown in Figure 2, the main steps to model a system will be as follows: (i) Define a new system or select an existing one to be studied, e.g., Al-Mg-Zn system. (ii) Select a thermodynamic model (or use the default sublattice model) to describe different phases. (iii) Collect available data needed for modeling from the database or user input. (iv) Set rules for optimization quality control suggested by software or selected by user. (v) The self-optimization procedure will work, and the final results will be generated. The last step (v) will not require interactions with the user; however, it will depend

on the internal-evaluation, self-optimization code (yet to be developed).

Additionally, MaterialsGenome has devised a number of the operational features and definitions that will become part of the developing software package. These features include a nomenclature system which will work in concert with the SQL database to determine the base metals and phases from established source identifications, and corresponding parameters (e.g. crystal structures). Additionally, a formalism has been established to name and identify parameters that would be employed by the user in setting up any particular analysis within using the software system.

### **ThermoCalc Software, Inc.**

Thermo-Calc Software provided technical support and advice to partnering organizations as needed, specifically, evaluation and use of thermodynamic data and use of CALPHAD-related tools including Thermo-Calc and DICTRA, both directly within the project and also in the context of a broader cyberinfrastructure. Thermo-Calc expects to support calculations made by OEM partners and also the development of a user-friendly, self-optimizing, phase equilibrium computer program and accompanying GUI for a wide range of wrought and cast Mg-based alloys; such an interface is being developed separately by MaterialsGenome, Inc. as part of this project.

During this reporting period, the supplier met with OEM partners to assess the current state-of-the-art, specifically for Al and Mg alloys, and to establish requirements for ultimately constructing a database, verifying and validating the same, and addressing challenges of automating this task and incorporating CALPHAD-type tools into a broader cyberinfrastructure. Additionally, calculations and comparisons were made using different commercially-available thermodynamic databases for Mg alloy AZ91D which demonstrated that there inadequacies in the present modeling of this alloy.

Thermo-Calc Software has cooperated with MaterialsGenome, Inc. regarding the automation of phase diagram assessments and the development of the software and graphical user

interface to make this task more accessible. The initial focus was on the general approach to automate the binary and ternary assessments and sharing experience of past attempts to accomplish this task. While the automation of binary assessments is novel, there has for many years been software tools built into applications such as Thermo-Calc that enable the expert to perform much of the numerical optimization associated with a thermodynamic assessment, directly within the code, in a semi-interactive/semi-automated manner. MaterialsGenome will take this fundamental approach further towards a novel, fully-automated methodology which also supports better archiving of the experimental data that is the foundation of the thermodynamic evaluation. There is a hurdle in going from a collection of binary and ternary assessed systems to a database that has been optimized and validated for specific alloys. Part of the development of such a database includes the validation of predictions (but not fitting of the data) to thermodynamic data available for higher-order commercial alloys. In situations where the fit is poor, the expert database developer will use their judgment to improve the data assessments and even apply estimated data required to improve the fit and accuracy of the database. It is the automation of this heuristic approach to thermodynamic modeling that presents the greatest challenge and opportunity. Incorporation of first principles 'ab initio' calculations of thermodynamic quantities, as being determined by the work at Northwestern University, is also expected to increase the accuracy models and improve the quality of estimations for unmeasured quantities.

### **Oak Ridge National Laboratory (direct DOE funding)**

This recently-initiated project is funded directly from DOE and, although it is not a formal part of the USAMP AMD703 project, is providing essential information for modeling microstructural evolution in Mg alloys. The ORNL project aims at developing a tracer diffusion database in Mg-based light material alloy systems. The safety issues that have hampered previous tracer diffusion measurements based on radioactive tracers are somewhat avoided in this project with the use of *stable isotopes* for most elements in this

study (except Al and manganese (Mn) for which radioactive isotopes are needed). Homogeneous single phase samples in the Mg-Al-Mn system will be prepared using conventional techniques; stable isotopes of these elements will be deposited in the form of thin films on these samples, and the measurement of isotopic diffusion profiles of stable isotopes in these samples after diffusion annealing will be conducted using automated secondary ion mass spectrometry (SIMS) facilities either at ORNL or University of Central Florida.. The combination of a tracer diffusion and thermodynamic database, which is being continually updated by other participants during the course of the Mg-ICME program, will provide the required interdiffusion information for the other modeling tasks in this program. The first year of this study will focus on isotopic diffusion measurements in the Mg-Al-Zn system which is the base system for commercial AZ alloys. Future work beyond these ternaries will include studies in Mg-Al-Zn and Mg-Al-Zn-Mn alloy systems. Additionally, various diffusion formalisms will be evaluated for the test Cu-Ni-Zn system (for which a tracer diffusion database already exists). The formalisms will be then evaluated for the Mg tracer diffusion database when completed.

The primary progress in 2008 centered on upgrades to the Secondary Ion Mass Spectrometry (SIMS) facility at ORNL. The SIMS instrument (Cameca ims4f ion microscope, Figure 3) is being upgraded for the high sample load of this project initially with hardware improvements, to be followed by method and automated software developments. Completed upgrades include improved pumping of the secondary ion source, permitting a vacuum of  $10^{-11}$  torr. This level of vacuum virtually eliminates interferences caused by formation of secondary ion hydrides, which in fact are the principle interferent in isotope ratio measurements. Pending upgrades include integration of optical and electronics microscopic systems with the secondary ion microscope systems of the Cameca. These upgrades will permit automated determination of exactly where on a sample measurements are being made at any given time.

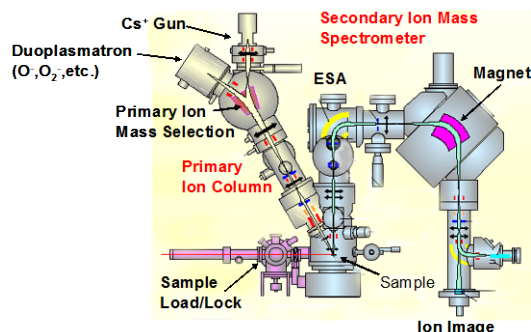


**Figure 3.** Schematic of ORNL Cameca ims-4f SIMS system that is ideally suited for isotope ratio diffusion depth profile measurements.

### **Task 3 Processing-Structure-Property Relationships for Extruded Magnesium Components**

The team has selected alloys AM30 and AZ61 as the model alloys for this task. Extrusions are being supplied by the AMD604 extrusion task team in the form of crush columns.

#### **Mississippi State University**

MSST is developing experimental characterization techniques and fundamental knowledge of the extrusion process for Mg alloys to understand their processing-structure-property relationship (see report 6.H). Particular alloys being studied are AZ61 and AM30. Main research activities are focused on performing microstructural / mechanical characterization of automotive components to build a material database for model development; carrying out lab-scale extrusion experiments to learn about the process and validate material and numerical models; developing a multiscale materials modeling approach using molecular dynamics, discrete dislocations, and crystal plasticity to generate a robust internal variable model for large scale simulations; and constructing experimentally validated finite element models of the extrusion process for process design and optimization.

Figure 4 presents results of the microstructural studies (texture and grain morphology) performed on an extruded component (GM crash rail, AM30). Besides being used for modeling purposes, such information helps to gain insights

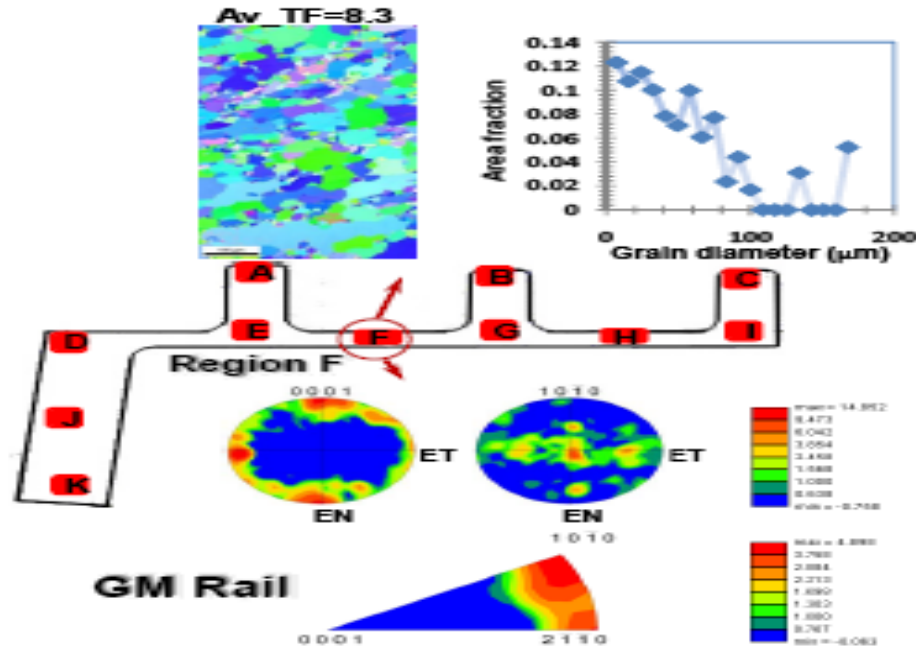


**Figure 4.** Microstructural characterization at specific locations of GM crash rail. The material is Mg alloy AM30.

into how the process parameters may relate to the extrudate mechanical properties (e.g., anisotropy), an aspect strongly linked to the product performance.

Figure 5 shows a preliminary finite-element model for the lab-scale extrusion experiments being designed and performed at MSST. There are a number of numerical issues that need to be addressed when modeling extrusion (e.g., finite-element formulation and numerical integration of material models). In particular, modeling the extrusion process with fully Eulerian and Arbitrary-Lagrangian-Eulerian finite-element formulations helps avoid the large mesh distortion problems typically exhibit by Lagrangian formulations.

Fractographic analyses on the strain-life specimens were completed. The *in-situ* scanning electron microscopy SEM fatigue specimens are being prepared so that the fatigue damage can be observed at microscale.

*Constitutive Modeling:* Progress has been made at all scales of simulation. MSST has developed a new nested internal state variable (ISV) theory that

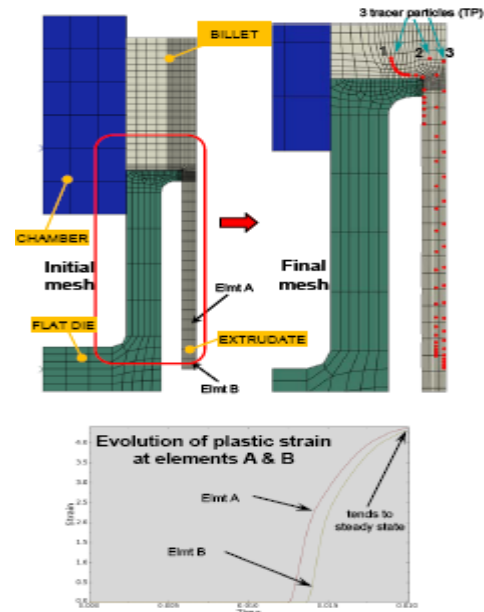


**Figure 5.** Finite-element model of preliminary lab-scale indirect extrusion experiments using ABAQUS.

physically and strongly couples deformation and internal defects. A methodology related to a higher order tensorial rank of damage for void nucleation and void growth has been developed. Uncertainty

related to material heterogeneities that facilitated new optimized material development has been quantified. With this new nested macroscale ISV theory, MSST is conducting some materials-processing studies that capture the structure-property relations in the model correlation and model validation stages. At lower scales, they have implemented and tested kinematics, kinetics, and hardening rules for twinning deformation in a crystal plasticity code. They analyzed dislocation/twin activities in a Mg single crystal under different loading conditions and used that information to identify the parameters of slip hardening rules. This multiscale material model of Mg alloys reproduced well the anisotropic responses reported in the literature.

### Lehigh University

Modeling of the extrusion process for Mg alloys of interest (e.g., AZ31, AM30 and AZ61) is a subtask of the AMD604 project, being conducted by Lehigh University and is closely aligned with objectives of the ICME project. MSST has also conducted modeling of the extrusion process as part of the ICME project, using alternative methodologies. Lehigh's current approach utilizes a "modified" Barrett flow-stress model for the deformation of magnesium as elevated temperature and various strain rates, incorporating an added contribution from dynamic recovery and recrystallization [7]. Agreement between theory and experiment for AZ31 at 350°C and 0.01 sec<sup>-1</sup> strain rate is shown in Figure 6.

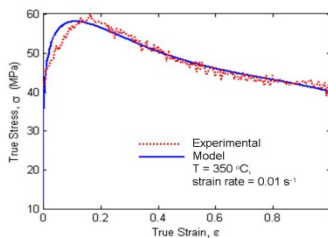


**Figure 6.** Agreement between theory and experiment for extrusion of AZ31 as determined by Lehigh University.

### Task 4 Processing-Structure-Property Relationships for Sheet Magnesium Components

The team has chosen alloy AZ31 as the model alloy for this task. The alloy will be provided in the form of a formed box sample and will be provided by the AMD602 Warm Forming of Mg project team (see report 2.B).

#### The University of Virginia

The University of Virginia is presently a participant in the AMD602 (Warm Forming of Magnesium) project, and its tasks under AMD703 are coordinated with those efforts, specifically with regard to modeling and the development of constitutive equations for the warm-forming of Mg sheet alloys (typically AZ31). One role in the AMD703 program is to provide guidance in model selection and parameter identification. Two basic approaches are being examined:

*a. Phenomenological/continuum approach.* A literature review of the models that have been developed to simulate the flow of metals (including Mg) undergoing dynamic recovery (DRV) and recrystallization (DRX) has now been completed. The relevant equations were identified and shared with the ICME team. Initial constitutive modeling focused on the pseudo steady-state viscoplastic response of the magnesium alloy, AZ31, at elevated temperatures. Results presented in Figure 7 show that the Sellars-Tegart [8] hyperbolic sine relation accurately models the flow stress at a fixed strain as function of strain rate and temperature within the regime of interest (i.e.,  $T = 150 - 350^{\circ}\text{C}$ ) for all four of the sheet materials examined within the AMD602 project (designated here as O, M, N, and X). The deformation condition is described by the temperature compensated strain rate parameter,  $Z = \dot{\epsilon} \exp(Q/RT)$ , where  $Q$  is an apparent activation energy, strain rate,  $R$  is the gas constant and  $T$  is temperature.

The technical partner at GM has used the derived Sellars-Tegart constitutive model for alloy O to perform sheet forming simulations at 200, 250,



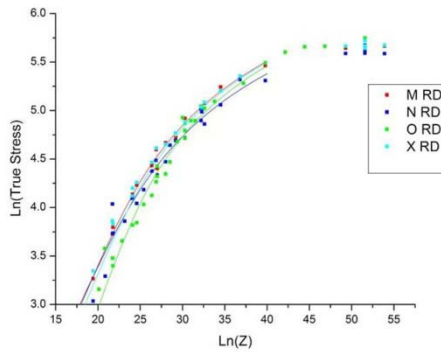


**Figure 7.** Best fits of the Sellars-Tegart relation [8] to the flow stresses at a strain of 0.1 of the four sheets (O,M,N,X) over a wide range of deformation conditions, Z (assuming  $Q = 140\text{kJ/mol}$ ).

and  $300^\circ\text{C}$  using the PAMSTAMP 2G computer code. The geometry and boundary conditions of the simulations were designed to conform to those of the warm forming trials being performed within the context of the AMD602 project. Figure 8 shows the results of the simulation performed at  $300^\circ\text{C}$ , which highlight the fact that the most sheet thinning occurs at the corners of the pan wall where actual failure was observed to occur during the forming trials.

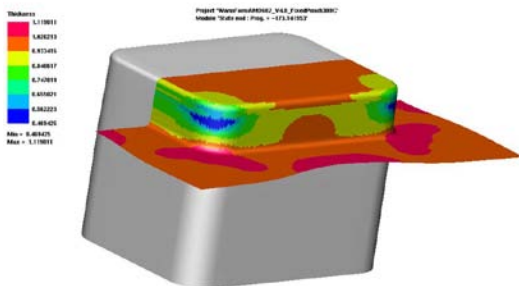


**Figure 8.** PAM-STAMP 2G simulation of warm forming of AZ31 material ‘O’ using constitutive model provided by the University of Virginia.

More recent modeling efforts have exploited the ICME network through collaboration with partners at MSST. They have made the GUI, DMGfit, available to us and provided guidance in how to develop an accurate parameter set for modeling not only the temperature and strain-rate dependence of the flow stress, but also the strain

hardening using an internal state variable model developed by Bammann, Chiesa, and Johnson [9]. While the actual strain hardening exhibited by the alloy AZ31 under conditions of adequate warm formability is marginal, the internal state variable modeling approach provides a platform upon which to develop the desired DRX modeling capacity. This is viewed as a critical goal of Task 4, since DRX is known to induce strain softening, which can have a negative impact upon the formability.

The advantage of the phenomenological approach outlined above has been the ability to quickly integrate within the finite-element modeling context. However, it is well known that the crystallographic texture of magnesium alloy sheets can render the material anisotropic and that the texture itself can evolve rapidly with strain, particularly in cases where mechanical twinning is active. Thus, a second, more fundamental approach based upon crystal plasticity, is also being investigated.

**b. Crystal plasticity/mechanistic approach.** This aspect of the project is very new. While polycrystal plasticity models exist, they have primarily been developed to describe room temperature flow of Mg alloy sheets. Although, various *ad hoc* approaches to incorporate temperature dependence have been explored, it has been concluded that a more rigorous approach incorporating the effects of “creep mechanisms” of climb and/or dynamic recrystallization must be developed. The University of Virginia team is presently examining viscoplastic creep models that activate the climb of dislocations using a modified version of the generalized Schmid law that is used to activate slip. Similarly, the effect of the nucleation of new grains during the process of dynamic recrystallization is being considered. The team believes that this may be another means by which lack of strong texture evolution during flow at elevated temperatures can be explained. Finally, prediction of forming limit curves (FLCs) and post-formed room temperature stress/strain properties will further serve to validate the models being considered. A crystal plasticity-based forming limit code was written during a prior project and will be used in simulations once the appropriate constitutive models are validated.

Inputs and outputs will be coordinated with companion USAMP projects.

**Task 5 Processing-Structure-Property Relationships for Die-cast Magnesium Components**

The team has selected alloy AZ91D as the model alloy for this task. Limited work may also be conducted in alloy AM50. Super vacuum die-cast shock towers from the AMD604 casting task team have been provided for use in this project Task.

**The University of Michigan**

The goal of this particular study is the development of experimentally-validated models that account for the influence of microstructure on monotonic tensile properties and low-cycle fatigue response of high-pressure die-cast Mg alloys. Seventy SVDC AZ91D shock tower castings have been received and a metallographic survey of five key casting regions (Figure 9) has been completed

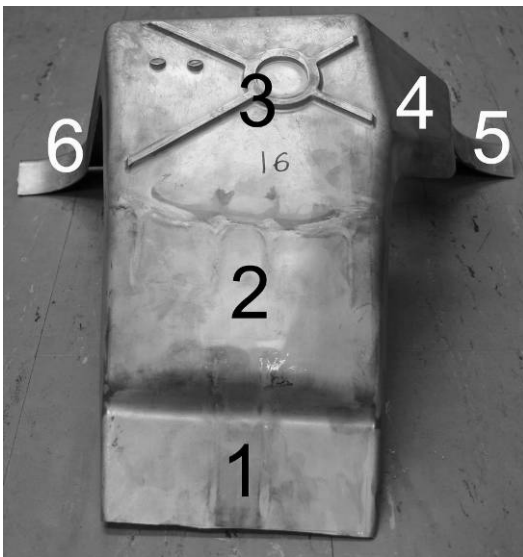


**Figure 9.** SVDC shock tower showing locations of microstructural and heat treatment studies.

to characterize variation in the as-cast microstructure with location and to provide a baseline for subsequent heat treatment and low cycle fatigue investigations. Vickers microhardness is being used as an indicator of mechanical properties as a function of aging treatment. The influence of aging time up to 500 hours and aging temperature (168 and 216°C),

as well as the influence of time (up to 25 hours) at the solution treatment temperature of 413°C have been examined. As-cast microhardness is shown for three locations in Figure 10, and the significant response to heat treatment is shown in Figure 11.

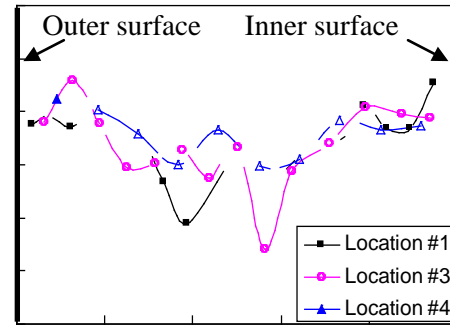


**Figure 10.** Baseline microhardness as a function of casting location showing variation across casting thickness.

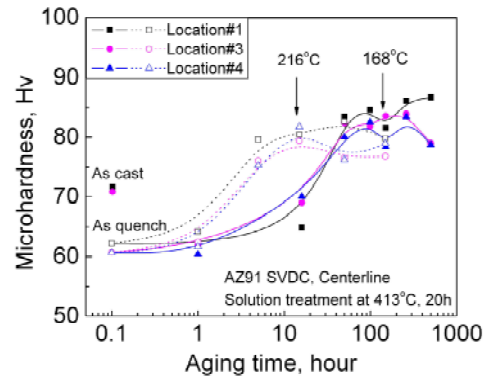


**Figure 11.** Response to heat treatment for three different locations in shock tower.

Tensile tests are ongoing and initial results are consistent with the results of the microhardness studies. X-Ray Powder Diffraction has been used to assess changes in phase fraction with heat treatment, and the variation of the fraction of  $\beta\text{-Mg}_{17}\text{Al}_{12}$  with aging time at 168°C is shown in Figure 12. This technique will be used to evaluate, to the extent possible, the kinetics of phase changes during heat treatment. Low-cycle fatigue tests are underway on as-cast sheet coupons extracted from specific locations in the SVDC shock towers, and the preliminary results are

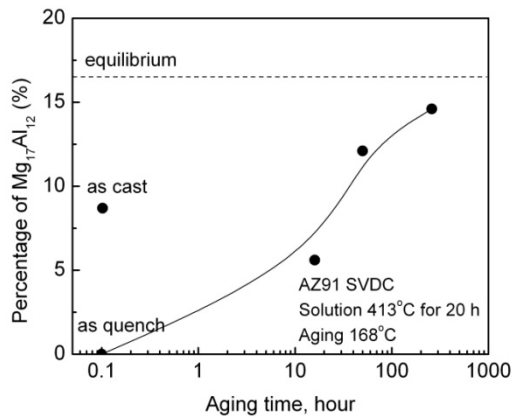


**Figure 12.** Variation of beta phase fraction with aging time determined by x-ray powder diffraction.

shown in Figure 13. Low-cycle fatigue work will continue in the coming year with tests on heat-treated materials.

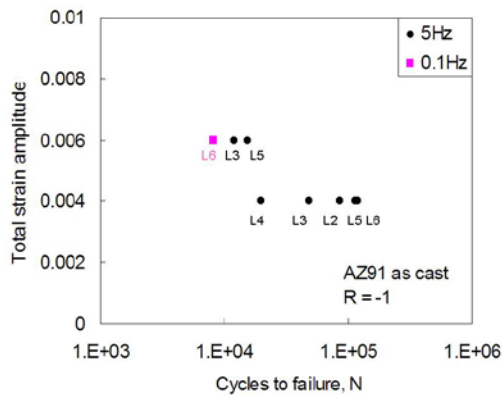


**Figure 13.** Fatigue life versus total strain range for different locations in SVDC shock towers in the as-cast condition.

**Magma Foundry Technologies, Inc.**

MAGMA Foundry Technologies, Inc. has participated in this project to aid in the development of computer mapping tools for the prediction of mechanical properties in large magnesium castings. MAGMA has focused on transferring information from the casting process simulation tool MAGMASOFT to finite-element meshes. Additional result transfers have been conducted to verify the transfer capabilities of different result files (i.e., temperatures and stress

distributions). The development of models to predict the microstructure of die-cast magnesium components is continuing. The main focus is now placed on the simulation of the filling and solidification of the demonstrator component and the comparison of the simulation results with observer/measured casting defects and properties to develop quality and property maps for Mg castings produced by the SVDC process. Figure 14 illustrates a typical calculation of residual stresses in the SVDC shock tower as shown in Figure 9.

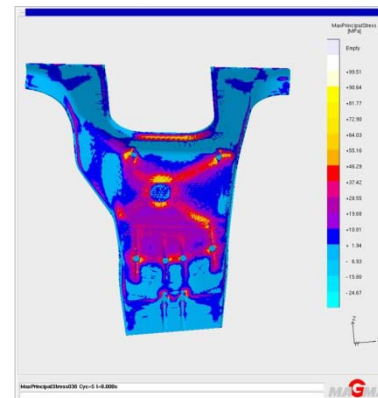


**Figure 14.** Residual stress pattern in SVDC magnesium shock tower (Figure 9) as determined by MAGMASOFT CAE simulation.

**Task 6 Multi-Attribute Design Optimization**

**Mississippi State University**

MSST developed a new technique based on optimum ensemble of metamodels, examined the performance of five different metamodeling techniques, and established a framework for Flexible Advanced Metamodel Estimator (FAME) with the code currently under development with the ICME Cyberinfrastructure. MSST investigated a single-level reliability-based design optimization (RBDO) methodology and its application to an automotive structural component (e.g., side rail). In collaboration with the MSST Multiscale Material Modeling group, they initiated this objective ahead of the original schedule. Using the available ABAQUS UMAT subroutine for A356 cast Al, they were able to integrate multiscale material modeling, uncertainty analysis, design optimization, and metamodeling technologies, and demonstrate the new capability in design

optimization of an automotive control arm. Work on this task is currently on hold pending development of the appropriate multi-scale modeling knowledge base for Mg alloys.

## Task 7 Fatigue

### **Mississippi State University**

MSST has also conducted literature surveys on fatigue and small-crack growth in Mg alloys. They developed a test matrix and test specimens for tensile and fatigue tests on the Mg alloys to determine material parameters for the multi-stage fatigue (MSF) and Small-Crack Theory models. In anticipation of receiving AM30 and AM61 extrusion, MSST acquired two AZ31D extrusions from GM. Monotonic tension and compression tests were conducted as well as uniaxial low cycle fatigue tests. The framework of MSF modeling was developed for AZ31 Mg alloy. Typical loading spectra for automotive applications were reviewed. FASTRAN was used to calculate the fatigue behavior using crack growth. The shape of the calculated strain-life curve was very similar to the test data (see Figure 15).

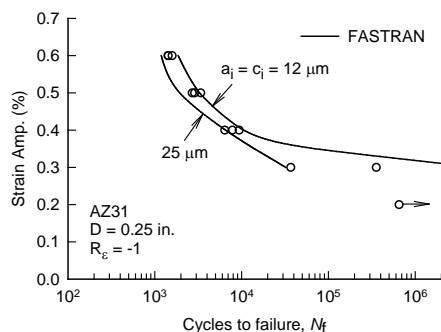


**Figure 15.** Strain-life curve for AZ31 magnesium alloy.

## Conclusions

The Integrated Computational Materials Engineering for Mg in Body Applications project was launched in 2007 and incorporates interfaces with the AMD604 project. All work plans have now been adopted, contracts issued and both “kick-off” and first review meetings conducted. Substantial progress has been made in all task areas as evidenced by the individual report areas. The TMS “Magnesium” and “ICME” web portals are operational.

## Acknowledgments

The success of this project is due to the dedicated efforts of team members at Chrysler, Ford, and General Motors, as well as The University of Michigan, The University of Virginia, Northwestern University, MaterialsGenome, Inc., Magma Foundry Technologies, Inc., ThermoCalc Software, Inc., and The Minerals, Metals and Materials Society (TMS). The project leadership also acknowledges the ongoing collaboration with colleagues at Mississippi State University. The USAMP ICME project management team is comprised of Randy Beals, Chrysler; Lou Hector, GM; John Allison, Ford; and Robert McCune, Project Administrator. The continuing support of our respective organizations and the US Department of Energy is gratefully acknowledged.

## References

1. Integrated Computational Materials Engineering, Annual Report to DOE, J.E. Allison, Principal Investigator, USAMP, 2007.
2. Integrated Computational Materials Engineering: A Transformational Discipline for Improved Competitiveness and National Security,” Committee on Integrated Computational Materials Engineering, National Research Council, ISBN: 0-309-12000-4 (2008).  
<http://www.nap.edu/catalog/12199.html>
3. [http://mferd.hpc.msstate.edu/\\_layouts/login.aspx](http://mferd.hpc.msstate.edu/_layouts/login.aspx)
4. A Canada-China-USA Collaborative Research and Development Project “Magnesium Front End Research and Development (MFERD)” 2007 Annual Progress Reports, Project Technical Committee, Hangzhou, China, April 2008.
5. Joint APS/TMS Symposium "Frontiers in Computational Materials: Session I" held in New Orleans, LA, TMS Annual Meeting, March 10, 2008.
6. <http://iweb.tms.org/forum/default.aspx?forumid=15>
7. M. Barnett, Z. Keshavarz, and X. Ma. “A Semianalytical Sachs Model for the Flow Stress of a Magnesium Alloy.” *Metallurgical*

- and Materials Transactions A*, 37(7), 2283–2293 (2006).
8. C. M. Sellars and W. J. Tegart, 1967. “Relationship between strength and structure in deformation at elevated temperature,” *Mem. Sci. Rev. Metall.* 63, 731–745.
  9. D. J. Bammann, M. L. Chiesa, and G. C. Johnson, “Modeling large deformation and failure in manufacturing processes,” pp. 359–376 in R. Tatsumi, E. Watanabe, and T. Kambe, eds., *Theoretical and Applied Mechanics*, London: Elsevier (1996).

## H. Multiscale Microstructure-Property Plasticity Considering Uncertainty

*Principal Investigator: Mark F. Horstemeyer*

*Chair in Solid Mechanics & Professor, Mechanical Engineering*

*Center for Advanced Vehicular Systems*

*Mississippi State University*

*206 Carpenter Bldg., P.O. Box ME*

*Mississippi State, MS 39762*

*(662) 325-7308; fax: (662) 325-7223; e-mail: mforst@me.msstate.edu*

*Co-Principal Investigator: Douglas J. Bammann*

*Professor, Mechanical Engineering*

*210 Carpenter Bldg.*

*Mississippi State, MS 39762*

*(662) 325-3260; Home: (662) 294-2585; fax: (662) 325-5433; e-mail: bammann@cavs.msstate.edu*

*Co-Principal Investigator: Esteban B. Marin*

*Senior Structural Analyst, Center for Advanced Vehicular Systems*

*Mississippi State University*

*200 Research Blvd.*

*Mississippi State, MS 39762*

*Office: (662) 325-6696; fax: (662) 325-5433; e-mail: ebmarin@cavs.msstate.edu*

*Co-Principal Investigator: Kiran Solanki*

*Research Associate, Center for Advanced Vehicular Systems*

*Mississippi State University*

*200 Research Blvd.*

*Mississippi State, MS 39762*

*Office: (662) 325-5454; fax: (662) 325-5433; e-mail: kns3@cavs.msstate.edu*

*Technology Area Development Manager: Joseph A. Carpenter*

*(202) 586-1022; fax: (202) 586-6100; e-mail: joseph.carpenter@ee.doe.gov*

*Field Project Officer: Aaron D. Yocum*

*(304) 285-4852; fax: (304) 285-4403; e-mail: aaron.yocum@netl.doe.gov*

*Contractor: Mississippi State University*

*Contract No.: 4000054701*

### Objective

- Develop a multiscale nested internal state variable (ISV) modeling methodology that includes statistical variations from the material microstructure for lightweighting designs, made of various structural alloys.

### Approach

- The approach is to quantify structure-property relations through multiscale modeling and multiscale experiments, so the macroscale ISVs can capture the lower length-scale effects. Once the cause-effect relations are quantified for various engineering metal alloys, then statistical methods can be used in the context of the ISVs and used for constitutive models in finite-element analysis (FEA). As such, the FEA can be used for a simulation-based design methodology as manufacturing processes and in-service life are accurately modeled.

## Accomplishments

- Progress has been made at all scales of simulation. In doing so, we have developed a new nested ISV theory that physically and strongly couples deformation and internal defects. We established a methodology related to a higher order tensorial rank of damage for void nucleation and void growth. We then developed and quantified uncertainty related to material heterogeneities which would facilitate the optimization of lightweight material development. With the newly developed macroscale ISV theory, we conducted some materials-processing studies that capture the structure-property relations in model correlation and validation stages.

### **Calibration, Validation, and Verification Including Uncertainty of an ISV Plasticity and Damage Model**

The rationale and motivation of this study are to understand the effect of material internal heterogeneity and boundary conditions on localized damage and its progression mechanism. The failure mechanism studied here is a result of void-nucleation, growth, and coalescences, which are modeled using a physically-based ISV form of microstructure-property model (Horstemeyer et al. 2000a), based from the plasticity of Bammann et al. (1993) and later modified to incorporate damage due to void-nucleation, growth and coalescences by Horstemeyer et al. (1999, 2000a). The overall procedure to study the effect of material microstructural variability and boundary conditions on the material response and failure mechanism can be outlined as depicted in Figure 1. First, the experimental uncertainties due to both systematic and bias are calculated along with uncertainties in the microstructure features in the model. Then, the microstructure features with their variability, the experimental stress-strain curves with their variability and the model-calibrating routine is used to calibrate material

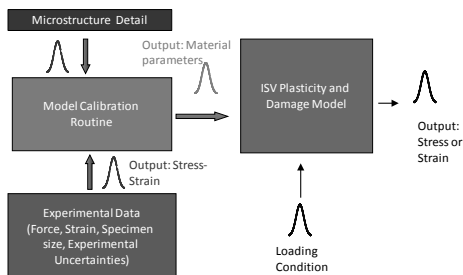


**Figure 1.** Procedure for studying the effect of material microstructure variability and loading conditions on material response and their failure mechanisms.

parameters along with their variability. The calibrating routine used here is a material point simulator. Finally, a user material subroutine is developed, implemented, and used to predict material mechanical responses and material failure mechanisms along with their respective uncertainties. One of the most important contributions the authors believe is to show how internal microstructural clustering affects strain to failure.

### **Material Mechanical Responses, Microstructure Characterizations, and Their Uncertainties**

The microstructure of a typical metallic material contains a large number of microdefects such as microcracks, dislocations, pores, and decohesions. Some of these defects are induced during the manufacturing process and are present before the material is subjected to mechanical loads and thermal fields. In general, these defects are small and distributed throughout most of the volume.

In this report, we focus on a wrought 7075-T651 aluminum (Al) alloy. The 7075-T651 aluminum is a wrought product with a relatively high yield strength and good ductility. As displayed by the triplanar optical micrographs of the plate concerned in the current investigation shown in Figure 2, the grains of this wrought alloy were found to be pancake shaped and aligned in the rolling direction of the wrought plate.

An optical microscope image of the wrought alloy, as shown in Figure 3, displays typical 7075-T651 aluminum microstructure in the untested condition. The alloy contains two main types of primary particles: iron (Fe)—rich particles,  $[Al_6(Fe,Mn), Al_3Fe, \alpha Al(Fe,Mn,Si)]$  and

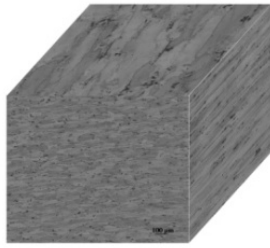


**Figure 2.** Triplanar optical micrograph illustrating the grain structure and orientation of 7075-T651 aluminum alloy.

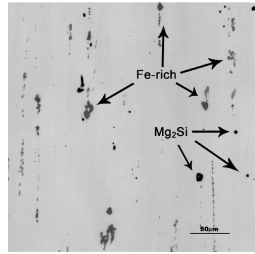


**Figure 3.** Microstructure of unstrained 7075-T651 aluminum alloy (Harris, 2006).

$Al_7Cu_2Fe$ ] and silicon (Si) compound particles  $Mg_2Si$ ). The iron-rich intermetallic particles are seen in the optical micrograph (Figure 3) as light grey particles, and the  $Mg_2Si$  intermetallics are shown as the dark particles. The particle size, nearest-neighbor distance and aspect ratio for the primary distributions for the iron-rich and  $Mg_2Si$  intermetallics in the untested condition were tabulated from a  $5.75\text{ mm}^2$  area of material for each of the orientations and are shown in Figure 4. Figure 4(a) displays the area size of the particles, Figure 4(b) displays the nearest neighbor distance of the particles and Figure 4(c) displays the aspect ratio distributions of the particles. The mean values of the particle area, area fraction, aspect ratio, and nearest neighbor distances are displayed in Table 1. In addition to the intermetallic particle stereography, the average grain size was determined by electron backscatter diffraction (EBSD) analysis taken in each of the directions and the results listed in Table 1. Figure 5 displays the grain morphology of the 7075-T651 aluminum alloy along with its orientation distributions (Figure 6).

To properly model the 7075-T651 alloy, standard monotonic experiments were performed (American Society for Testing and Materials [ASTM] E8). Three different types of monotonic experiments (tensile, compression and torsion) were performed along the longitudinal direction. All experimental specimens were machined 2.54 mm from the rolling surface of the plate. The tension, compression and torsion tests were performed with a strain rate of 0.001/sec in an ambient laboratory environment.

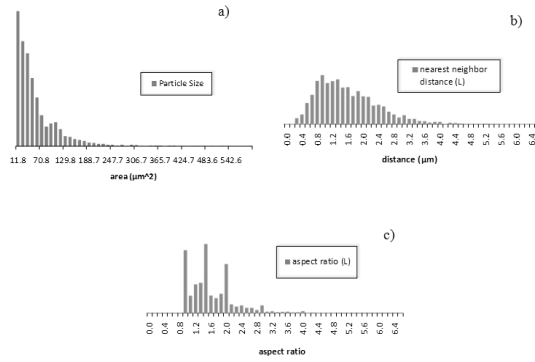


**Figure 4.** Stereological distributions of intermetallic particles (large) in the longitudinal (L) direction: (a) particle area, (b) nearest-neighbor distance, (c) aspect ratio.

**Table 1.** Metallographic analysis of virgin aluminum 7075-T651 alloy

Particle Area Fraction	Avg. Particle Size ( $\mu\text{m}^2$ )	Avg. Nearest Neighbor Distance ( $\mu\text{m}$ )	Avg. Grain Size ( $\mu\text{m}$ )
0.025	68.2	18.7	18.9

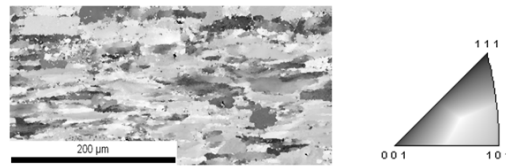


**Figure 5.** Microstructural grain orientation and size analysis for 7075-T651 aluminum alloy in the longitudinal direction.

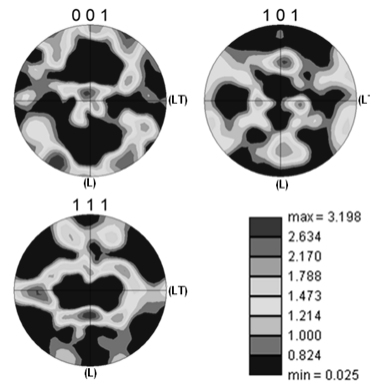


**Figure 6.** Crystal orientation of the wrought 7075-T651 alloy.



The experimental stress/strain curves were tabulated by taking load and strain values and by using the nominal cross-sectional area. In order to quantify random uncertainties of measured quantities, three specimens for each direction of the alloy were tested. Table 2 shows the accuracy related to different instruments used to measure load-strain curve. The experimental uncertainties are calculated based on systematic and random uncertainties in the measured quantities such as force, strain, and specimen sizes, Eqs. (1)–(3) (see Coleman and Steele, 1999).

$$U_E = \sqrt{U_r^2 + U_s^2} \tag{1}$$

where  $U_r$  is random uncertainty and  $U_s$  is systematic uncertainty.

**Table 2.** Accuracy of instruments used to measure load-strain in monotonic tension, compression, and torsion tests

	Accuracy
Load Cell	1%
Extensometer	1%
Micrometer	0.001 in
Data Acquisition Load Reading	0.25%
Data Acquisition Strain Reading	0.25%

The random uncertainty in experimentally measured quantities  $r_i$  (force and strain) for  $M$  different tests is given by

$$U_r = 2\sqrt{\frac{1}{M-1} \sum_{i=1}^M (r_i - r_{mean})^2} \tag{2}$$

The systematic uncertainty in experimentally measured quantities  $r_i$  (force and strain) for  $M$  different tests is given by

$$U_s = r_i \sqrt{U_L^2 + U_{daq}^2} \tag{3}$$

where  $U_L$  is uncertainty in the load cell or extensometer or strain gauges, and  $U_{daq}$  is the uncertainty in the data acquisition. The tensile tests were conducted using a Tinius Olson type tensile machine. The tests were conducted in constant cross-head control, with a speed of 5 inches per minute. An MTS knife-blade axial extensometer with a 2-inch gage length was used for the strain measurement and was set at a full

scale of 25% strain and calibrated to better than 0.25% through the full-scale range. The load cell was calibrated to within 0.25% error reading through the full-scale range. The stress-strain data were collected on a System 5000 Data Acquisition system. Similarly, compression and torsional tests were also performed. Figure 7 shows mechanical responses of wrought 7075 aluminum alloy under tension, compression, and torsional loadings with their variability from mechanical experiments. From experimentally measured mechanical response, it was found that the variations in elongation to failure are about  $\pm 5.2\%$ ,  $\pm 6.3\%$ , and  $\pm 6.5\%$  for torsion type loading, tensile loading, and compressive loading, respectively.

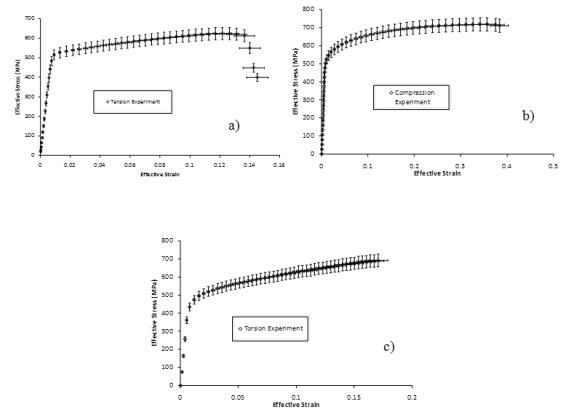


**Figure 7.** Material mechanical response under (a) tension, (b) compression, and (c) torsion loadings with their variability.

Additional tests were performed to further characterize the mechanical behavior (Bauschinger effects) of the wrought alloy. The Bauschinger effect is interpreted as anisotropic “yielding” that arises upon reverse loading from internal backstresses that are attributed to dislocations accumulating at obstacles. To quantify the Bauschinger effect, cylindrical low-cycle fatigue-type specimens with a uniform gage length based on ASTM standard E606 were used. Specimens with an outer diameter of 10.135 mm were used to test the 7075-T651 and were machined from the longitudinal direction of the two-inch-thick plate. The strain rate was 0.001/sec and the temperature was ambient. Two types of experiments to observe the Bauschinger effect were conducted. First, the cylindrical specimens were prestrained in tension and then uniaxially

reloaded in compression. The second type included a different set of specimens that were prestrained in compression and then uniaxially reloaded in tension. Figure 8 shows the Bauschinger behavior of the wrought 7075 aluminum alloy for tension followed by compression, and compression followed by tension with their variability from mechanical experiments.

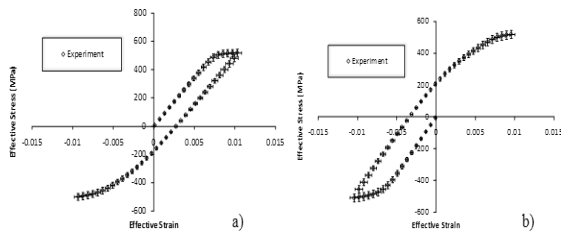


**Figure 8.** Material Bauschinger behavior under (a) tension followed by compression and (b) compression followed by tension with their variability.

Further experimental tests for the model calibration included interrupted tensile experiments in the longitudinal direction to determine the primary void nucleation rate and damage constants for the ISV model. As confirmed by Dighe et al. (2002), obtaining interrupted cracked or debonded sub-micron particles is not feasible and as such, the damage rate was assumed to be the same as the primary particles. Tensile specimens were loaded monotonically to pre-determined strain levels and sectioned for void and/or crack density quantification. The cracked and debonded primary particles were then quantified as a function of effective strain similar to Dighe et al. (2002).

### **Model Calibration, Validation, and Verification**

In this section, we develop a model calibration technique for the structure-property ISV model (Horstemeyer 2001), with its associated variabilities. The model calibration technique used here differs from the classical uncertainty calibration technique. Here model calibration means fitting model parameters using a material point simulator and calculating associated uncertainty using a Monte-Carlo technique with a

sample size of  $10^6$ . The material model will be calibrated with different stress states, Bauschinger effect and material microstructure details. Then the calibrated model will be implemented, using a user material model routine in commercially available finite element code ABAQUS. The verification simulations will be performed using ABAQUS and compared with the experimental data. Finally, a series of validation simulations will be performed for validation and prediction capability.

### **Model Calibration**

A nonlinear regression algorithm in conjunction with Monte-Carlo technique was used to calibrate the above mentioned microstructure-property ISV model, Eqs. (1) to (3). The internal state variable model was calibrated with experimentally-measured mechanical responses from tension, compression, torsion, tension followed by compression and compression followed by tension and their variabilities. Along with mechanical responses, the material microstructure characteristics (particle size, particle orientation, void size, void orientation, grain size, and nearest-neighbor distance) and their variability were also used in the model calibration process (see Figure 1). First, uncertainty in calibration data was calculated, then through Monte Carlo simulations with a sample size of  $10^6$  and a nonlinear regression algorithm, we calibrated the physically-motivated material model for a given set of mechanical responses and microstructural detail. The sampling distributions for microstructural features are shown in Figures 4 to 6. For mechanical responses, we used a normal distribution with three standard deviations derived from the uncertainty calculations using the propagation rule (see Coleman and Steele, 1999).

The microstructure-property-based ISV model includes plasticity material parameters related to the yield stress, kinematic hardening, isotropic hardening, and the shear and the bulk moduli, along with their temperature and strain-rate dependencies, all of which were calibrated using experimentally-measured mechanical responses and microstructural features, as shown in Table 3. It includes the damage progression, which is multiplicatively decomposed into void-nucleation,

**Table 3.** Microstructure-property (elastic-plastic) model parameters for 7075-T651 aluminum alloys

ID #	Constants (Units)	Mean	Constants		
			ID #	Mean	
1	$G$ (MPa)	26426	15	$C_{10}$ (°K)	5.0
2	$A$	1.0	16	$C_{11}$ (sec/MPa)	0.0
3	$K$ (MPa)	68915	17	$C_{12}$ (°K)	0.0
4	$B$	0.0	18	$C_{13}$ (1/MPa)	0.323
5	The melt temp (°K)	1400	19	$C_{14}$ (°K)	0.0
6	$C_1$ (MPa)	0.0	20	$C_{15}$ (MPa)	3625
7	$C_2$ (°K)	0.0	21	$C_{16}$ (°K)	12
8	$C_3$ (MPa)	360	22	$C_{17}$ (sec/MPa)	0.0
9	$C_4$ (°K)	110	23	$C_{18}$ (°K)	0.0
10	$C_5$ (1/MPa)	1.0	24	$C_a$	3.99
11	$C_6$ (°K)	0.0	25	$C_b$	-0.627
12	$C_7$ (1/MPa)	0.07581	26	init.temp (°K)	297
				heat gen.	
13	$C_8$ (°K)	0.0	27	Coeff.	0.0
14	$C_9$ (MPa)	2937			

void-growth, and void-coalescence variables. The microstructure characteristic parameters are calibrated in conjunction with plasticity parameters using mechanical response and microstructure features as shown in Table 4.

**Table 4.** Microstructure-property (damage) model parameters for 7075-T651 aluminum alloys

ID #	Constants (Units)	Mean
28	$M$	0.3
29	$R_o$ (mm)	0.00931
30	$an$	3.187e-7
31	$bn$	16737.2
32	$cn$	1250
33	$C_{coeff}$	0.00837
34	$K_{ic}$ MPa(m <sup>1/2</sup> )	29.
35	$d$ (mm)	0.00931
36	$F$	0.027598
37	cd1	0.108
38	cd2	0.93373
39	DCS0 (mm)	40
40	DCS (mm)	40
41	Z	0.01
	initial void volume	
42	fraction	0.0001
43	NTD	-850
44	CTD	-0.0172
45	NND	8.0E-5

The uncertainty distributions calculated during the calibration process using the Monte Carlo method related to the material and microstructural parameters of microstructure-property model are shown in Figures 9 to 15. Several observations can be drawn from these results. One can see that in almost every case the material mechanical

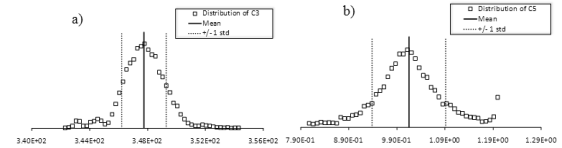


**Figure 9.** Uncertainty distribution of material parameters related to the yield stress (a) yield stress parameter which determines the rate independent yield stress and (b) yield stress parameter which determines the transition strain rate from rate independent to dependent.

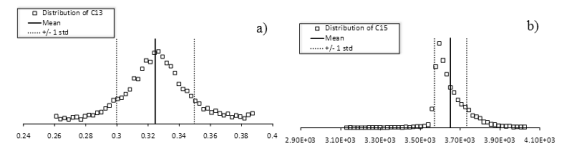


**Figure 10.** Uncertainty distribution of material parameters related to the isotropic hardening (a) isotropic hardening parameter which describes the isotropic dynamic recovery and (b) isotropic hardening parameter which describes the isotropic hardening modulus.

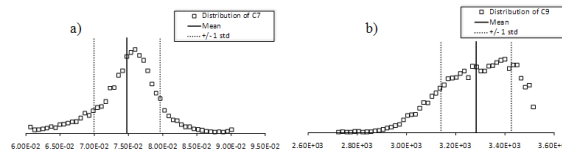


**Figure 11.** Uncertainty distribution of material parameters related to the kinematic hardening (a) kinematic hardening parameter which describes the kinematic dynamic recovery and (b) kinematic hardening parameter which describes the kinematic hardening modulus.

response and microstructural parameters have the same distribution shape (Gaussian), but different uncertainty levels (the spread of distribution). This could be due to the different sensitivity levels of each model parameter in the constitutive relationship for this material.

Having calibrated the model parameters and quantified the uncertainty associated with these parameters, comparisons were made of the stress evolution as a function of strain for different stress states to predict strain-to-failure and the work-hardening behavior. Figures 16–17 show the effective stress–strain response comparisons for different stress states and the associated

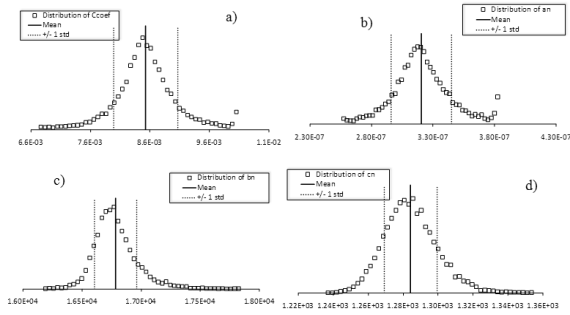


**Figure 12.** Uncertainty distribution of material parameters related to the void nucleation (a) void-nucleation exponent coefficient, (b) void-nucleation parameter which related nucleation density under torsion, and (c–d) are void-nucleation parameters related to tension and compression void nucleation densities.

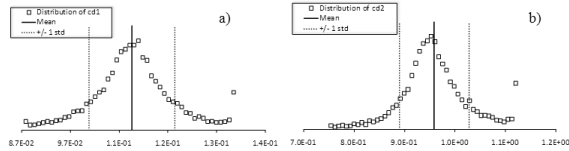


**Figure 13.** Uncertainty distribution of material parameters related to the void coalescence (a) void coalescence parameter related to void sheeting, and (b) void coalescence parameter related to void impingement.

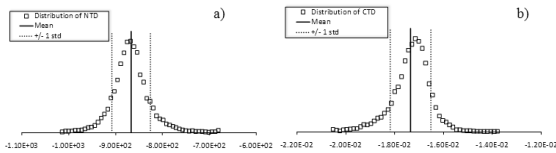


**Figure 14.** Uncertainty distribution of material parameters related to (a) the temperature dependency on the void nucleation, and (b) the temperature dependency on the void coalescence.

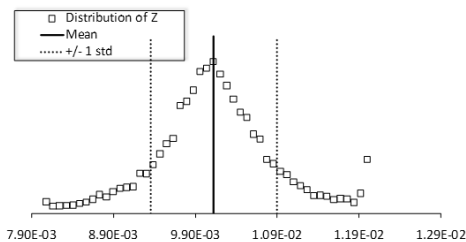


**Figure 15.** Uncertainty distribution of material parameters related to the material texture.

variability. As Figures 16–17 show, the model is able to compare/predict the elongation to failure with a given level of uncertainty in initial microstructural clustering. It was found that the variations in elongation-to-failure are about  $\pm 7.0\%$ ,  $\pm 8.1\%$ , and  $\pm 9.75\%$  for torsion loading, tensile loading, and compressive loading, respectively, due to initial material microstructural heterogeneities.

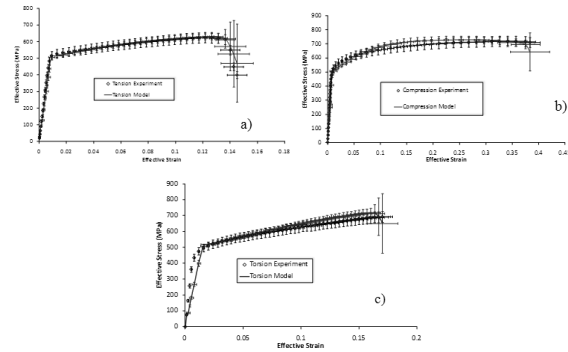


**Figure 16.** Comparison of experimental tension, compression and torsion data with a microstructure-property model under (a) tension, (b) compression, and (c) torsion loadings with their associated variability.

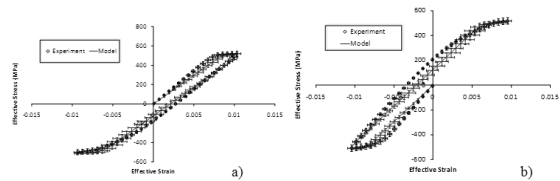


**Figure 17.** Comparison of experimental measure material Bauschinger behavior with a microstructure-property model under (a) tension followed by compression, and (b) compression followed by tension with their variability.

After good initial correlations with monotonic stress state responses, next the damage progression was plotted for different stress states, as shown in Figure 18. From Figure 18, we can observe that the rate of damage is higher for tension, followed by torsion, and then compression. This may be a material characteristic because with the same microstructure-property model, Horstemeyer et al. (1999) noted that for an A356 cast aluminum alloy, the damage rate was higher for torsion, followed by tension, and then compression. The evolution of damage distributions at different

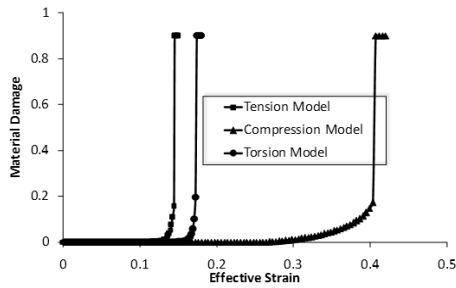


**Figure 18.** Damage progressions of aluminum alloy 7075-T651 for different stress states.

tensile strains are shown in Figure 19. It is interesting to note that initial isotropic damage (symmetric) evolved into an anisotropic form (asymmetric) as applied strain is increased. Another interesting observation is that as the applied strain is increased, the spread of evolution of damage distribution increased even though the uncertainty in the input microstructure remained the same.

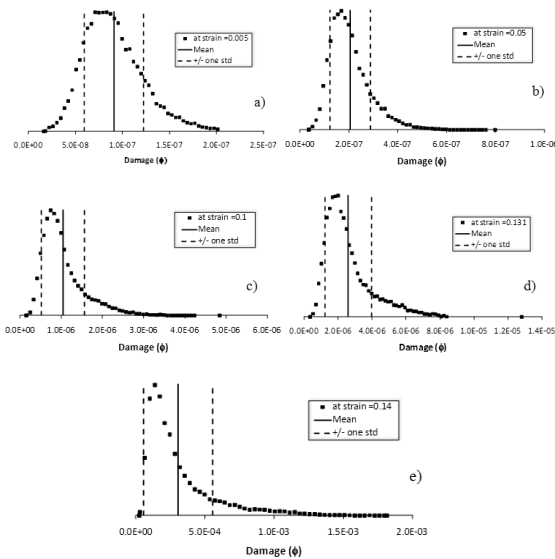


**Figure 19.** Evolution of damage distributions at different tensile strain: (a) at strain = 0.005, (b) at strain = 0.05, (c) at strain = 0.1, (d) at strain = 0.131, and (e) at strain = 0.14.

In the present study, the material damage was modeled through a multiplicative decomposition into void-nucleation, void-growth, and void-coalescence. It is important to understand why initially isotropic damage distributions evolved

into an anisotropic form. For that, we plotted nucleation density distribution evolutions for tensile strains as shown in Figure 20. It is interesting to remember that the initial microstructural distributions (for example, the particle size) are asymmetric and the particle aspect ratio is symmetric. Because the loading directions would be different along the short and long axis of the particles, the physical behavior observed by Jordon et al. (2008) showed an anisotropic response.

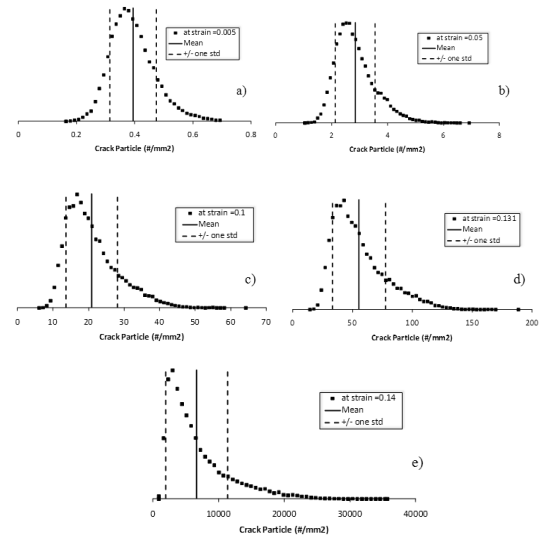


**Figure 20.** Evolution of nucleation density distributions at different tensile strain: (a) at strain = 0.005, (b) at strain = 0.05, (c) at strain = 0.1, (d) at strain = 0.131, and (e) at strain = 0.14.

Finally, it should be noted that the results presented here include initial distributions and correlation effects of material mechanical responses and microstructural parameters. The use of other probability distributions may have a strong effect on the quantitative values of the results, while the qualitative values still hold.

**Model Verification**

For model verification (ensuring that the model is implemented correctly in the finite element codes), simulations were performed using ABAQUS finite-element software under different loading conditions (tension, compression, torsion, tension followed by compression and compression followed by tension). Figures 21 and 22 show the stress-strain curves comparing the finite-element

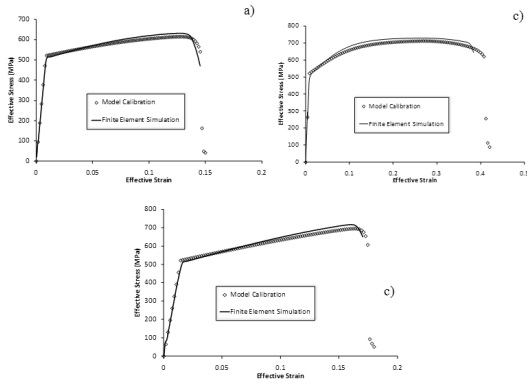


**Figure 21.** Comparison of finite element simulated mechanical responses under (a) tension, (b) compression, and (c) torsion.

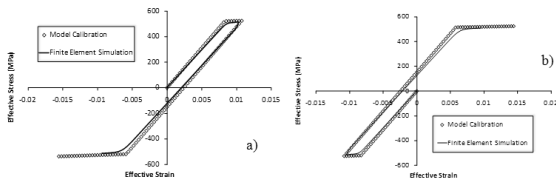


**Figure 22.** Comparison of finite element simulated Bauschinger under (a) tension followed by compression and (b) compression followed by tension.

simulations results to the results obtain through calibration processes at different stress states.

Figures 21 and 22 show good correlation and how the model captured the differences between the work-hardening rate in tension, compression, and torsion, which express the importance of a physically motivated internal state variable plasticity and damage continuum model for modeling microstructural details. The model is able to capture the history effects arising from the boundary conditions and load histories, the microstructural defects and progression of damage from these defects and microstructural features such as second- phase particles and intermetallics.

**Model Validation**

For model validation (ensuring that the model captures the correct physics/mechanics), notch tensile tests were conducted as shown in Figure 23. The stress triaxiality is the primary driving factor for damage in ductile materials. In a uniform material, the notch geometry induces a

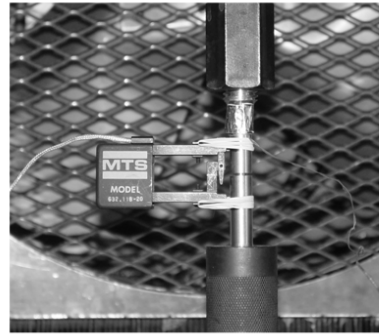


**Figure 23.** The 0.025-inch-radius notched Bridgman specimen made of AA7075-T651 shown with the 1-inch axial extensometer placed across the notch to measure displacement.

smooth stress triaxiality field with a maximum value near the center of the specimen. In a damaged medium, stress concentrations induced by the presence of pores may cause local regions of high stress triaxiality. The notch tests were conducted with constant cross-head speed of 5 inches per minute. However, a MTS knife-blade axial extensometer with a 1-inch gage length was used for the strain measurement and was set at a full scale of 25% strain and calibrated to better than 0.25% for the full scale range. The load cell was calibrated to within 0.25% error reading through the full-scale range. The data were collected on a System 5000 Data Acquisition system. Figure 24 shows a good comparison of notch specimen experiment data with finite-element simulation result.

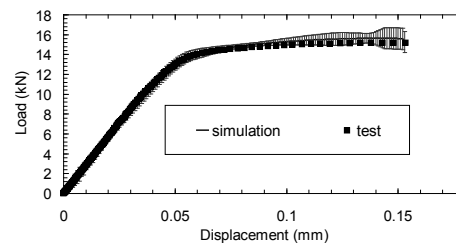


**Figure 24.** Comparison of experimental measured load-displacement response of aluminum alloy 7075-T651 with a calibrated microstructure-property model for a notch radius of 0.025 inch.

**Sensitivity of Damage Uncertainty at Different Strain Values**

In this section, we calculate the sensitivity of the damage uncertainty to multiscale material parameters. We measure the sensitivity of damage,  $S_i$ , to an input mechanical response and microstructural parameters (see Tables 3 to 4)  $X_i$  by using

$$S_i = \frac{\partial \phi}{\partial C_i} \frac{X_i}{\phi} \tag{4}$$

where  $C_i$  is the coefficient of variation of  $X_i$ . Notice that the second term is used for normalization purposes. Sensitivity of damage uncertainty to the uncertainties of the mechanical responses and microstructural parameters are depicted in Figure 25 for tension. For instance, Figure 25(a) shows that at the very beginning of the damage evolution the initial radius of a void,  $r_0$ , and nucleation coefficient are the most influential parameters. Figures 25(b-c), on the other hand, show that as damage progresses the initial temperature, the fracture toughness as the void started to nucleate and void growth are more important. Finally, Figure 25(d) displays the effect of coalescence and growth parameters on the last stages of damage progression. A similar observation was noted for the compressive and torsional loading case. The sensitivity plots are shown in Figure 25 for tension and are also consistent with the physics of the damage progression for this particular type of material. At

the very beginning, the initial defect size and number density of cracked particles are important. As the damage evolves, more voids nucleate and grow. Finally, voids combine with each other and coalescence becomes the main driver.

**Summary**

The rationale and motivation of this study are to understand the effect of material internal heterogeneity and boundary conditions on localized damage and its progression mechanism. We analyzed the effect of uncertainty in microstructural features (i.e., voids, cracks, inclusions), along with uncertainties in loading and boundary conditions on the mechanical response and damage evolution (or accumulation) of a wrought aluminum alloy. We first calibrated the microstructure-property relationship model with monotonic mechanical responses (tension, compression, torsion, tension followed by compression and compression followed by tension) and material microstructure features. Based on the calibration results, we quantified the influence of uncertainty of various material model parameters in the constitutive equations on uncertainty in damage. During the calibration process, we have also shown that a physically-motivated material model was necessary to understand and predict the stress states and damage states associated with rolled aluminum containing large intermetallics. The uncertainty distribution related to material parameters associated with the plasticity and microstructural features were also tabulated during the calibration processes and show that almost every material mechanical response and microstructural parameters have the same distribution shape (Gaussian), but different uncertainty level (the spread of distribution).

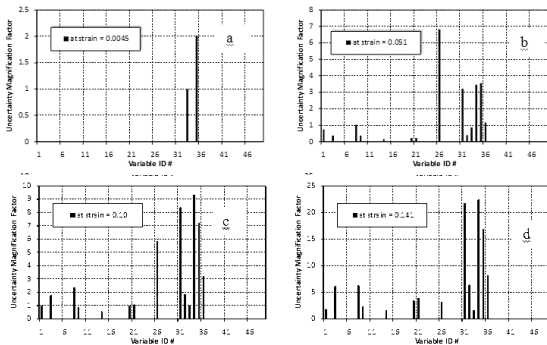


**Figure 25.** Sensitivity of uncertainty of damage under tension type loading to the uncertainties of the microstructure-property material model parameters: (a) at strain = 0.0045, (b) at strain = 0.051, (c) at strain = 0.1, and (d) at strain = 0.141.

Having calibrated the model with monotonic loadings, validation and verification simulations and tests were performed using different types of loading, geometrical, and boundary conditions. The modeling result shows good correlation with experimental data. This study demonstrates a method of calibrating, verifying, and validating a microstructure-property relationship based on an internal state variable form material model. However, this chapter’s important contribution is

the approach of modeling and quantifying uncertainties associated with the damage from particles. Thus, this approach could be used to model composites and other heterogeneous materials. The authors believe that the good correlation of the internal state variable plasticity and damage continuum model to the experimental results, along with sensitivity analysis, support the physically-based modeling of void nucleation, growth, and coalescence resulting from large and small particles.

The following conclusions are drawn from the results of this work.

- Better correlation with experimental compression, tension, and torsional stress-strain curve was demonstrated.
- Uncertainty calculations revealed that the distribution of material damage, void nucleation, and growth changes related to the applied strain path. It also revealed that small variations in experimental data could lead to significant variations in strain-to-failure.
- Uncertainty calculations revealed that the initial isotropic damage (symmetric) evolved into an anisotropic form (asymmetric) as applied strain is increased, consistent with experimentally-observed behavior for 7075 aluminum alloy in the literature.
- The spread of damage-evolution distribution increases with the applied strain, even though the uncertainties of initial microstructure distributions remain the same.
- The sensitivities of the uncertainty of damage to the uncertainties of the input material responses and microstructural parameters were found to be dependent on the strain values. As the strain value changed (that is, as the damage evolved), the importance of these material responses and microstructural parameters changed.
- The sensitivities were found to be consistent with the physics of the damage progression for this particular type of material. At the very beginning, the initial defect size and number density of cracked particles are important. As the damage evolves, more voids are nucleated and grow. Finally, voids combine with each other and coalescence becomes the main

driver. It also shows that the damage evolution equations provide an accurate representation of the damage progression due to large intermetallic particles.

- Finally, we have shown that the initial variation in the microstructure clustering lead to about  $\pm 7.0\%$ ,  $\pm 8.1\%$  and  $\pm 9.75\%$  variation in the elongation to failure strain for torsion, tension, and compression loading, respectively.

### **Magnesium Extrusion**

At present, our efforts are focused on developing a reliable experimental procedure for crystallographic data collections of extruded magnesium alloys. A sample-preparation procedure was developed that showed a good repeatability. Figures 27 and 28 display [0002], [1010] and [1120] pole and inverse pole figures together with ODF maps of a sample machined from the center of Section F of an extruded AM30 bumper beam. The entire section is schematized in Figure 26 with highlight on locations that will be analyzed for this component. In the pole figures, the normal direction coincides with the extrusion direction. The texture in Figure 27 was obtained from crystallographic data collected at  $0.1 \mu\text{m}$  step size, while in Figure 28 the step size was  $0.5 \mu\text{m}$ . The difference in step size was intended to reveal the effect of twinning on texture by modifying the statistical contribution of the associated disorientation. A typical width of a fully-grown twin in extruded AM30 alloy measures approximately  $2 \mu\text{m}$ .

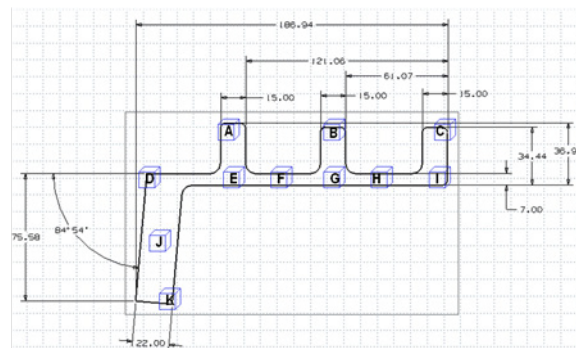


**Figure 26.** Cross-section of an AM30 bumper beam highlighting the sub-sections to be analyzed.



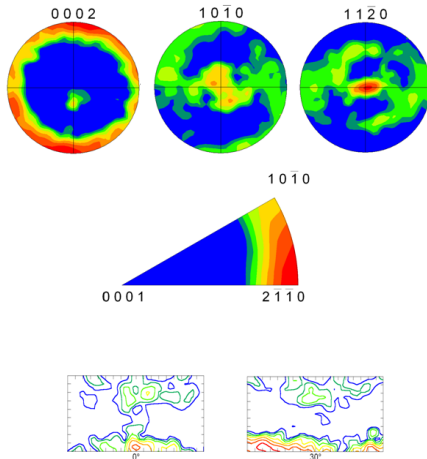


**Figure 27.** Extrusion texture at the center of Section F obtain after collection at 0.5 μm step-size showing, (a) [0002], [1010] and [1120] pole figures, (b) inverse pole figure of the extrusion axis, and (c) ODF in  $\phi_2$ -sections.

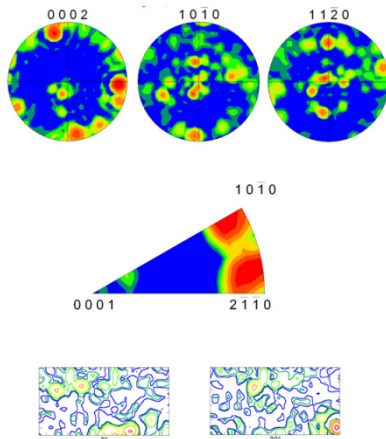


**Figure 28.** Extrusion texture at the center of Section F obtain after collection at 0.1 μm step-size showing, (a) [0002], [1010] and [1120] pole figures, (b) inverse pole figure of the extrusion axis, and (c) ODF in  $\phi_2$ -sections.

For both scans the extrusion axis tends to concentrate in the vicinity of the [1010] pole, which is typical for deformed hcp metals by mean of extrusion. This rod texture is sharper for the scan obtained at the larger step-size, where the basal pole [0002] rotated to scatter uniformly around the normal of the extrusion axis. In

contrast, for the scan with a smaller step-size, the texture develops secondary fibers that may be related to the [1010] peak through a twinning relationship. The formation of these secondary fibers is consistent with the increased statistical contribution of twinning expected for finer scans.

**Macro-Texture Analyses**

Texture analyses of the AM30 based bumper beam have been performed by means of X-ray diffraction using a Rigaku system. The pole figure data are being collected and the purchase of friendly commercial software for ODF calculation is being investigated.

**Metal Forming of Magnesium Sheet**

To represent the unusual stress-strain material responses of magnesium alloys compared with other conventional cubic crystalline metals, appropriate constitutive equations that reflect viscoplasticity, anisotropy, damage, strain sensitivity, temperature dependence, grain size, and twinning need to be developed. These mechanical properties are also needed to accurately predict strain-field evolution, thinning, and localization in the sheet-metal forming. Currently, an existing DMG microstructure-plasticity model is calibrated to the material responses of Mg AZ31 uniaxial tensile tests at different strain rates and temperatures (Figure 29). This model will be modified and extended to include the aforementioned mechanical responses. Also, a stress-integration algorithm that accounts for plane stress conditions needs to be developed

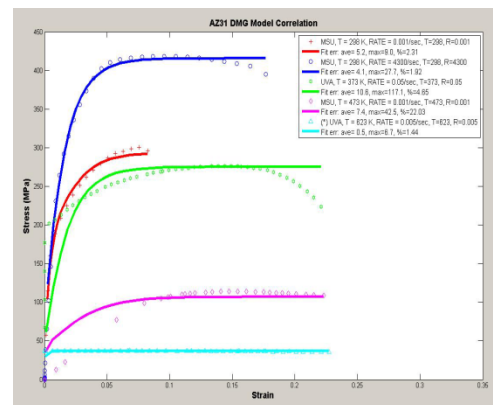


**Figure 29.** Material fitting of Mg AZ31-O with DMG model.

and implemented in a general finite-element code such as ABAQUS, in order to take advantage of the shell elements, which have been proven to be very time efficient compared to three-dimensional (3D) solid elements.

### Sheet-Metal Forming Simulations

The forming limit diagram depicts the maximum strains that can be sustained by sheet materials prior to the onset of localized necking, which is a common failure mode in metal forming. Generally, this failure process is controlled not only by external loading but also by internal microstructures. The major mechanical material properties controlling the formability (i.e., the forming limit diagram) of sheet metals are the work hardening, the rate sensitivity, and the plastic anisotropy of the sheet material. To evaluate the mechanical properties of Mg AZ31 magnesium alloys and study their formability, warm-forming finite-Element (FE) simulations of pan forming of magnesium sheets (Figure 30) are performed at various conditions (temperature, tool speed, friction, binder pressure, etc.) using the current version of the DMG model.

#### Pan Die Geometry

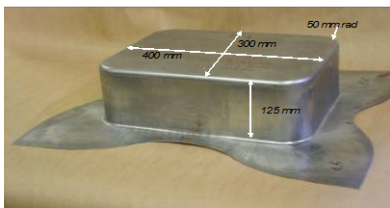


**Figure 30.** MgAZ31 warm-forming pan geometry for FE simulations.

In this analysis, the punch is assumed stationary, while the die moves down after the sheet is clamped with a given binder force and the sheet is then formed around the stationary punch. The coefficient of friction varies within a range of 0.16 and 0.20. The sheet and die temperatures are set to be equal, starting at 250°C, and the run simulations at 25°C increments to 350°C. Regarding the binder pressure, arbitrary values are chosen until data will be measured from the forming tests. Different results will be post-processed (Figure 31), and the prediction of

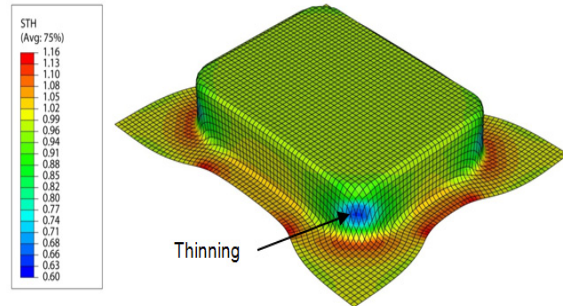


**Figure 31.** Thickness distribution after warm forming of a pan box.

forming limit curves and post-formed stress/strain properties will serve to validate the models.

### References

1. H. Agarwal, A. M. Gokhale, S. Graham, S., and M. F. Horstemeyer (2002), "Quantitative Characterization of Three-Dimensional Damage Evolution in a Wrought Al-Alloy under Tension and Compression," *Metallurgical and Materials Transactions A*, 33(8), 2599–2606.
2. D. J. Bammann, M. L. Chiesa, M. F. Horstemeyer, and L. I. Weingarten (1993), "Failure in Ductile Materials Using Finite Element Methods," eds. N. Jones and T. Weirzbicki, *Structural Crashworthiness and Failure*, Applied Science.
3. D. J. Bammann (2001), "A Model of Crystal Plasticity Containing A Natural Length Scale," *Mat. Sci. Engr.*, A309–310, 406–410.
4. Budiansky and O'Connell, (1976), "Elastic Moduli of a Cracked Solid," *Int. J. Solids Struct.*, 12, 81–97.
5. J. L. Chaboche (1993), "Development of Continuum Damage Mechanics for Elastic Solids Sustaining Anisotropic and Unilateral Damage," *Int. J. Damage Mech.*, 2 (4), 311–329.
6. B. D. Coleman and M. E. Gurtin (1967), "Thermodynamics with Internal State Variables," *J. Chem. Phys.*, 47, 59.
7. B. D. Coleman and W. Noll (1963), "The Thermodynamics of Elastic Materials with

- Heat Conduction and Viscosity,” *Arch. Ration. Mech. Anal.*, 13, 167–178.
8. H. W. Coleman and W. G. Steele (1999), “Experimentation and Uncertainty Analysis for Engineers,” 2nd Edition, John Wiley, New York, NY.
  9. J. P. Cordebois and F. Sidoroff (1979), “Damage Induced Elastic Anisotropy,” *Euromech 115*, Villard de Lens.
  10. Y. F. Dafalias (1985), “The Plastic Spin,” *Journal of Applied Mechanics*, 52 (44), 865–871.
  11. M. D. Dighe, A. M. Gokhale, and M. F. Horstemeyer (2002), “Effect of Strain Rate on Damage Evolution in a Cast Al-Si-Mg Base Alloy,” *Metall. Mat. Trans A*, 33A, 555–565.
  12. Gangalee and J. Gurland (1967), “On the Fracture of Silicon Particles in Aluminum–Silicon Alloys,” *Transactions of the Metallurgical Society of AIME*, 239, 269–272.
  13. W. M. Garrison Jr. and N. R. Moody (1987), “Ductile Fracture,” *J. of Physics and Chem. of Solids*, v 48 (11), 1035–1074.
  14. Y. Hammi and M. F. Horstemeyer (2007), “A Physically Motivated Anisotropic Tensorial Representation of Damage with Separate Functions for Void Nucleation, Growth, and Coalescence,” *Int. J. Plast.*, 23, 1641–1678.
  15. C. R. Harris (2006), “Particle Cracking Damage Evolution in 7075 Wrought Aluminum Alloy under Monotonic and Cyclic Loading Conditions,” M.S. Thesis, Georgia Institute of Technology.
  16. M. F. Horstemeyer, D. L. McDowell, and D. J. Bammann (1995), “Torsional Softening and the Forming Limit Diagram,” *SAE Tech. Ser.* 960599, ed. K. Chen, *Analysis of Autobody Stamping Technology*.
  17. M. D. Horstemeyer and A. M. Gokhale (1999), “A Void–Crack Nucleation Model for Ductile Metals,” *Int. J. Solids and Structures*, 36, 5029–5055.
  18. M. F. Horstemeyer, J. Lathrop, A. M. Gokhale, and M. Dighe (2000a), “Modeling Stress State Dependent Damage Evolution in A Cast Al-Si-Mg Aluminum Alloy,” *Theory and Appl. Fract. Mech.*, 33, 31–47.
  19. M. F. Horstemeyer and S. Ramaswamy (2000b), “On Factors Affecting Localization and Void Growth in Ductile Metals: A Parametric Study,” *Int. J. Damage Mech.*, 9, 6–28.
  20. M. F. Horstemeyer (2001), “From Atoms to Autos A New Design Paradigm Using Microstructure-Property Modeling, Part 1: Monotonic Loading Conditions,” Sandia National Laboratories, Sand2000-8662, March 2001.
  21. M. F. Horstemeyer and P. Wang (2003), “Cradle-to-Grave Simulation-Based Design Incorporating Multiscale Microstructure-Property Modeling: Reinvigorating Design with Science,” *Journal of Computer-Aided Materials Design*, 10, 13–34, 2003.
  22. L. M. Kachanov (1958), “Time of the Rupture Process under Creep Conditions,” *Izvestiya Akad. Nauk USSR, Otd. Tech. Nauk*, 8, 26–31.
  23. N. Kanetake, M. Nomura, and T. Choh (1995), “Continuous Observation of Microstructural Degradation During Tensile Loading of Particle Reinforced Aluminum Matrix Composites,” *Materials Science and Technology*, 11 (12), 1246–1252.
  24. J. Kratochvil and O. W. Dillon Jr. (1969), “Thermodynamics of Elastic-Plastic Materials as a Theory with Internal State Variables,” *J. Appl. Phys.*, 40, 3207.
  25. J. Lemaitre (1985), “Continuous Damage Mechanics Model for Ductile Fracture,” *Transactions of the ASME Journal of Engineering Materials*, 107, 83–89.
  26. M. P. Miller and D. L. McDowell (1992), “Stress State Dependence of Finite Strain Inelasticity,” *ASME Summer Applied Mechanics Meeting, Tucson, AZ, ASME AMD-Vol. 32, Microstructural Characterization in Constitutive Modeling of Metals and Granular Media*, 27–44.
  27. M. P. Miller, P. R. Dawson, and D. J. Bammann (1995), “Reflecting Microstructural

- Evolution in Hardening Models for Polycrystalline Metals,” *Simulation of Materials Processing: Theory, Methods, and Applications*, eds. Shen and Dawson, Balkema, Rotterdam.
28. S. Murakami (1988), “Mechanical Modeling of Material Damage,” *J. Appl. Mech.*, 55, 280–286.
  29. V. C. Prantil, J. T. Jenkins, and P. R. Dawson (1993), “An Analysis of Texture and Plastic Spin for Planar Polycrystals,” *Journal of the Mechanics and Physics of Solids*, 41 (8), 1357.
  30. T. Park and G. Z. Voyiadjis (1998), “Kinematic Description of Damage,” *J. Appl. Mech.*, 65, 93–98.
  31. M. Ortiz and E. P. Popov (1985), “Accuracy and Stability of Integration Algorithms for Elastoplastic Constitutive Relations,” *International Journal of Numerical Methods in Engineering*, 21, 1561–1576.
  32. J. Rice and D. M. Tracey (1969), “On the Ductile Enlargement of Voids in Triaxial Stress Fields,” *Journal Mechanics Physics Solids*, 17, 201–217.

## **I. Materials Design for Magnesium Alloys**

### ***Principal Investigator: Seong-Gon Kim***

*Associate Professor, Department of Physics and Astronomy*

*Mississippi State University*

*Hilburn Hall, Room 237, P.O. Box 5405*

*Mississippi State, MS 39762-5405*

*(662) 325-8031; fax: (662) 325-8898; email: kimsg@hpc.msstate.edu*

### ***Co-Principal Investigator: Mark F. Horstemeyer***

*Chair in Solid Mechanics and Professor, Department of Mechanical Engineering*

*Center for Advanced Vehicular Systems*

*Mississippi State University*

*206 Carpenter Bldg., P.O. Box ME*

*Mississippi State, MS 39762*

*(662) 325-7308; fax: (662) 325-7223; email: mfhorst@me.msstate.edu*

### ***Co-Principal Investigator: Hongjoo Rhee***

*Postdoctoral Associate*

*Center for Advanced Vehicular Systems*

*Mississippi State University*

*P.O. Box 5405*

*Mississippi State, MS 39762-5405*

*(662) 325-9221; fax: (662) 325-5433; email: hrhee@cavs.msstate.edu*

### ***Co-Principal Investigator: Sungho Kim***

*Postdoctoral Associate*

*Center for Advanced Vehicular Systems, CAVS 2182-C*

*Mississippi State University*

*Mississippi State, MS 39762-5405*

*(662) 325-9241; fax: (662) 325-5433; email: sk5@msstate.edu*

### ***Co-Principal Investigator: Shengjun (Dennis) Zhang***

*Postdoctoral Associate, Department of Material Science and Engineering*

*Robert R. McCormick School of Engineering and Applied Science*

*Northwestern University*

*2220 Campus Dr.*

*Evanston, Illinois 60208-3108, USA*

*(847) 491-5887; fax: (847) 491-7820; email: shengjun-zhang@northwestern.edu*

### ***Co-Principal Investigator: Greg Olson***

*Winson-Cook Chaired Professor in Engineering Design*

*The Steel Research Group at Northwestern*

*Department of Mechanical Engineering*

*Northwestern University*

*2145 Sheridan Road*

*Evanston, Illinois 60208-3111*

*(847) 491-2847; fax: (847) 491-7820; email: g-olson@northwestern.edu*

*Co-Principal Investigator: Qingyou Han*  
*Mechanical Engineering Technology Department*  
*Purdue University*  
*401 North Grant Street*  
*Knoy Hall, Room 107*  
*West Lafayette, Indiana 47907-2021*  
*(765) 494-7528; fax: (765) 494-6219; email: hanq@purdue.edu*

---

*Contractor: Mississippi State University*  
*Contract No.: 4000054701*

---

## **Objective**

- Investigate the effect of nanoscale precipitates and novel additives to the overall strength and ductility in magnesium (Mg) alloy systems.

## **Approach**

- In support of the collaborative materials design effort proposed here aimed at lightweight components for automotive applications, a systems approach to materials design [1] will be applied. Working within a multiscale hierarchy of microstructural subsystems governing desired property combinations for structural performance, key microstructural elements will be identified for the calibration, application, and validation of process/structure and structure/property design models defining key theoretical parameters and critical experiments enabling parametric design of novel alloy compositions.
- At the electronic level, quantum-mechanical first-principles simulations based on density functional theory (DFT) [2, 3] will be performed to elucidate the origin of the alloying effects. A fundamental understanding of solidification, dislocation, creep, fatigue, crack nucleation and failure of Mg-based alloy systems also requires accurate atomistic modeling of nanoscale systems containing up to hundreds of thousand atoms. We will perform large-scale atomistic simulations using efficient and reliable empirical interatomic potential methods such as the modified embedded-atom method (MEAM) [4, 5, 6] and force-matching-embedded-atom-method (FMEAM) potentials.
- Various state-of-the-art experimental techniques will also be employed in this project. Scanning electron microscopy (SEM) and transmission electron microscopy (TEM) will be used to obtain microscale as well as nanoscale structural information of Mg alloys. The structure and energies of dislocation cores and planar defects, including stacking faults and twin boundaries, determine the mechanical behavior of the Mg alloys. Electron backscatter diffraction (EBSD) and X-ray diffraction (XRD) measurements will be used to keep track of texture evolution during deformation. An in-situ chemical analysis and mapping of alloying elements can be used to keep track of these elements. Three-dimensional atom probe (3DAP) is capable of resolving the chemical identity and position of individual atoms in 3D with atomic resolution in the z-direction and sub-nanometer resolution in the lateral direction. Furthermore, fundamental thermo-mechanical experiments to measure creep resistance and ductility will be carried out under various loading conditions. Experimental failure analysis will be performed to understand the microstructure-driven mechanism of plasticity and damage growth under monotonic and cyclic loadings. X-ray computed tomography (CT) will be used to quantify the 3D morphological and topological evolutions of voids and microstructural features relevant to material damage. Depth-sensing microindenters and nanoindenters will also be used to evaluate the micromechanical properties of each microstructural phase present in the Mg alloys. These measurements will be used to validate and, in turn, guide the computational material design of new Mg alloys.

## Accomplishments

The objectives for the second year were met by accomplishing the following.

- Developed a new zinc (Zn) FMEAM potential using the multi-objective optimization method. The potential parameters and validation data have been compiled into a manuscript for publication (see reference 5 in the “presentations/publications/patents” section at the end of this report).
- Developed a new Mg-Zn FMEAM potential using the multi-objective optimization method. The potential is being applied to study the adsorption of Mg atoms on Zn surfaces and vice versa, and the data are being compiled into a manuscript to be submitted to a peer-reviewed journal (see reference 6 in the presentations/publications/patents section).
- Performed first-principles calculation of the crystal structure of  $\varphi$  phase in Mg-Zn-aluminum (Al) casting alloys. The results have been compiled into a manuscript for publication (see reference 7 in the presentations/publications/patents section).
- Performed materials/mechanical properties characterization on the die-cast base alloys (AZ91D, AM50A, AM60B, and AE44) to provide information for design and simulation efforts.
- Performed chemical analysis using a spectrometer, microstructure observation using optical and scanning electron microscopes, nanoindentation and microindentation tests, room temperature tensile tests at different strain rates, elevated temperature tensile tests, and creep tests by using Oak Ridge National Laboratory (ORNL) facilities.
- Investigated the strengthening precipitates in a Mg-7 wt % Zn-3 wt % Al alloy at peak hardness using 3DAP. The chemical compositions of the matrix and precipitates were measured by local-electrode atom probe spectrometry and compared with the results calculated by the Thermo-Calc software based on the COST2 database. Ternary nanosize precipitates have been found. The precipitates have compositions consistent with the ternary  $\varphi$  or  $\tau$  phase including its metastable extension. The equivalent sphere diameter of the precipitates at peak strengthening is measured as 20–50 nm, providing an important strength model calibration for materials design. The experimental results are available as a preprint (reference 3 in the presentation/publications/ patents section of this report).

## Future Direction

- Develop a new FMEAM potential for Al-Zn alloy systems to study Mg-Zn-Al ternary phases of Mg-based alloys.
- Validate Mg-Zn-Al FMEAM alloy potentials with DFT calculations.
- Perform quantum mechanical first-principles DFT calculation for Mg-Zn-Al casting alloys in the ternary  $\tau$  phase.
- Perform large-scale molecular dynamics (MD) simulations to study the effect of additive elements on material properties of Mg-based alloys using Mg-Zn-Al FMEAM alloy potentials.
- Carry out microstructure and mechanical properties characterization of new Mg-based alloys with novel additives.

---

## Introduction

Mg alloys are currently used in relatively small quantities for automotive components, generally limited to die castings. Two main barriers to wider use of Mg alloys in the automotive industry are poor creep resistance at temperatures above 150°C for powertrain applications and poor ductility for

structural body parts, engine components, engine cradles, and control arms.

To achieve the goal of improving the fuel efficiency of cars built in the future, the automobile industry needs to have lightweight, high-strength materials with better materials properties. We need to perform compositional design of Mg-based alloys in a manner that

increases creep resistance and ductility while keeping production costs low.

The future state of this technology will be the development of Mg-based alloys that have lower mass densities and increased strength compared to Al-based alloys, better creep resistance than that of AE44 grade Mg alloy, and costs comparable to that of AZ91D grade Mg alloy. The new Mg-based alloys should also exhibit sufficiently high ductility to allow conventional fabrication processes to be used, but generate adequate strength after the fabrication process.

### **Approach**

At the electronic level, quantum-mechanical, first-principles total-energy calculations are performed within DFT [2, 3] using Blöchl's all-electron projector augmented wave method [7] as implemented by Kresse et al. [8]. For the treatment of electron exchange and correlation, we use either local-density approximation [9, 10] or generalized gradient approximation [11] depending on the accuracy required. The Kohn-Sham equations are solved by using a preconditioned band-by-band conjugate-gradient minimization [12].

At the atomistic level, accurate atomistic simulations are performed using efficient and reliable empirical interatomic potentials such as MEAM [4, 5, 6] or FMEAM [13, 14] potentials. The interatomic potentials are constructed by optimizing the potential parameters to reproduce various experimental materials properties and atomic force data from DFT calculations.

Various state-of-the-art experimental techniques are used in this project. The chemical analysis is performed by using a spectrometer. Microstructures of the alloys are investigated by optical microscopy and SEM. SEM and TEM are used to obtain microscale as well as nanoscale structural information for Mg alloys. EBSD and XRD measurements will be used to keep track of texture evolution during deformation. The quantitative as well as qualitative chemical compositions of each phase present in the alloys will be individually analyzed by an energy dispersive X-ray spectroscopy technique. An in

situ chemical analysis and mapping of alloying elements can be used to keep track of these elements. A 3DAP is capable of resolving the chemical identity and position of individual atoms in 3D with atomic resolution in the z-direction and subnanometer resolution in the lateral direction. Conventional hardness tests will be conducted to gain overall properties of the alloys, while depth-sensing microindentation and nanoindentation tests are performed to obtain micromechanical properties of each microstructural phase present in Mg alloys. Thermomechanical experiments to evaluate creep resistance and ductility are carried out under various conditions. X-ray CT will be used before and after the creep tests to quantify the 3D morphological and topological evolutions of voids and microstructural features relevant to material damage. Experimental failure analysis will be performed to understand the microstructure-driven mechanism of plasticity and damage growth under monotonic and cyclic loadings. (For a more detailed description of our experimental and computational approach, see the 2007 annual report [15].)

### **Interatomic Potentials for Mg-Based Alloys**

In addition to the Mg, Al, and Mg-Al interatomic FMEAM potentials we developed in the first year [15, 16], we developed two additional interatomic potentials this year: Zn and Mg-Zn FMEAM potentials.

It is quite a challenge to develop a successful embedded-atom-method (EAM) potential for Zn [17] and only a few EAM potentials are available for Zn to date. Ramprasad and Hoagland developed an EAM potential for Zn and applied it to study the thermodynamic properties of small Zn clusters [18]. Recently, challenging the prevalent opinion of inadequateness of the EAM for hexagonal close packed (hcp) metals, Liu and coworkers developed a set of EAM potentials for the Mg-Al alloy system that give much more improved results than currently available MEAM potentials [14, 19]. Sun et al. further improved this EAM potential to get better equilibrium melting properties and high-temperature phase stability [20]. We prefer the EAM potential since we are interested in eventually developing related semiempirical potentials for alloy systems



involving Zn, such as the  $\rho$ -phase of Al-Mg-Zn [21]. EAM is much better suited for multicomponent systems than MEAM since EAM requires a separate potential for each pair of elements while MEAM requires a separate potential for each combination of triplets of atoms. Therefore, we choose Liu's EAM potential as a template to develop an EAM potential for Zn.

The multi-objective optimization procedure [22] was used to develop the Zn FMEAM potential [23]. We used the Mg potential by Liu et al. [14] as an initial potential. We used zero temperature configurations with fixed positions for various calculations except force calculations. We calculated the forces on Zn atoms in structures obtained by thermal equilibrium at six different temperatures. More than 18 objectives including equilibrium lattice constant, cohesive energies, and elastic constants are used to construct the EAM potential parameters for Zn. The cohesive energies of Zn atoms in hcp, face-centered cubic, and body-centered cubic crystal structures were calculated for several atomic volumes near the equilibrium atomic volumes. Figure 1 is the plot of cohesive energies of Zn crystals in hcp structure as a function of atomic volume. The minimum of this curve determines the equilibrium lattice constant  $a_0$  and equilibrium cohesive energy  $E_{coh} = E_{hcp}$ . Hexagonal crystals have five independent elastic constants:  $C_{11}$ ,  $C_{12}$ ,  $C_{13}$ ,  $C_{33}$ , and  $C_{44}$  [24]. The elastic constants are calculated numerically by

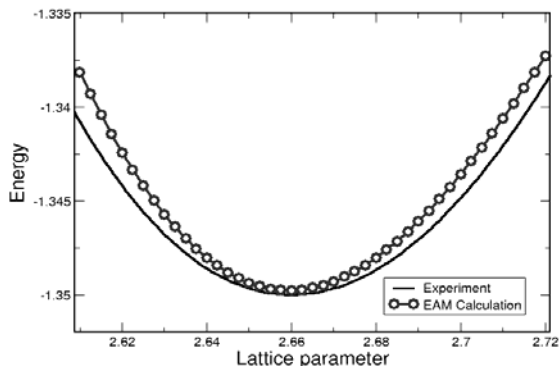


**Figure 1.** The energy per atom of Zn crystals in hcp structures as a function of atomic volume. The Rose's equation of state is constructed from experimental values of bulk modulus equilibrium volume and cohesive energy.

applying small strains to the lattice. We follow the procedure described by Mehl et al. [25] and apply several different strains ranging from  $-2.0\%$  to  $+2.0\%$ . The elastic constants are obtained by fitting the resultant curves to quadratic functions.

To obtain the force data, initial atomic structures that contain 192 Zn atoms were created from the bulk hcp crystal structure. The positions of atoms are randomly disturbed from their equilibrium positions and 10,000 steps of MD simulations with a time step  $\Delta t = 1.0$  fs were performed to equilibrate each structure for different temperatures. If no FMEAM potential is available for MD simulations, one could use an intermediate FMEAM potential that is generated. The potential should be adequate enough to obtain a reasonable set of structures.

The energy-volume curve for three basic structures has been evaluated with the present EAM potential and compared with DFT calculations. Figure 1 shows that our new Zn FMEAM potential reproduces the Rose's universal equation of state constructed from the experimental parameters rather well. Whenever possible, the experimental values are chosen as the target values. If the experimental values are not available or known to be unreliable, the computed values from the first-principles method are used.

We note that the present FMEAM potential reproduces the experimental lattice constant and the cohesive energy correctly. The sequence of the structures is also predicted correctly in the order of stability by the present Zn FMEAM potential. The five elastic constants for hexagonal crystal structure are in good agreement with the experimental values.

The force-matching against the ab initio forces database has also been performed. The DFT and FMEAM calculations were done with 192 atoms, at six different temperatures. It shows that the FMEAM potential from the present work reproduces the forces in close agreement with DFT calculations.

**Mg-Zn-Al Ternary Phase Structure**

The structure of  $Mg_{84}(Al_xZn_{1-x})_{68}$  alloy in ternary  $\phi$  phase has been determined from the first-principles calculations. Bourgeois et al. characterized the crystal structure of the equilibrium intermetallic  $\phi$ -phase formed in a Mg–Zn–Al casting alloy from electron diffraction patterns obtained using TEM [21]. Despite these experiments and a few simulations to reproduce the diffraction patterns, the equilibrium structure of  $\phi$  phase in a Mg–Zn–Al casting alloy is not fully determined and the identity of some of the ambiguous sites are yet to be determined [21, 26]. For the first time, we obtained the equilibrium structure and determined the identity of all atomic sites of  $\phi$  phase based on the first-principles method based on DFT [2, 3]. The structure and identity of atoms are determined by minimizing the heat of formation of  $Mg_{84}(Al_xZn_{1-x})_{68}$  alloy as a function of  $x$ . The heat of formation is evaluated from:

$$H_f = E[Mg_{84}(Al_xZn_{1-x})_{68}] - xE(Mg_{84}Al_{68}) - (1-x)E(Mg_{84}Zn_{68}) \quad (1)$$

There are 10 sites which Al and Zn atoms can occupy interchangeably. Figure 2 shows the heat of formation values obtained from Eq. (1) for all possible combinations ( $2^{10} = 1,024$ ). Figure 3 shows the structure of  $Mg_{84}(Al_xZn_{1-x})_{68}$  alloy in  $\phi$  phase with  $x = 0.4725$  that has the lowest heat of formation in Figure 2.

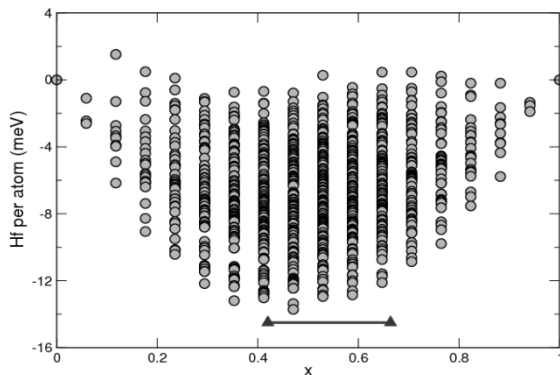


**Figure 2.** The heat of formation per atom of  $Mg_{84}(Al_xZn_{1-x})_{68}$  alloy as a function of  $x$ . The dark grey line indicates the range of  $x$  values consistent with previous experiments [21].

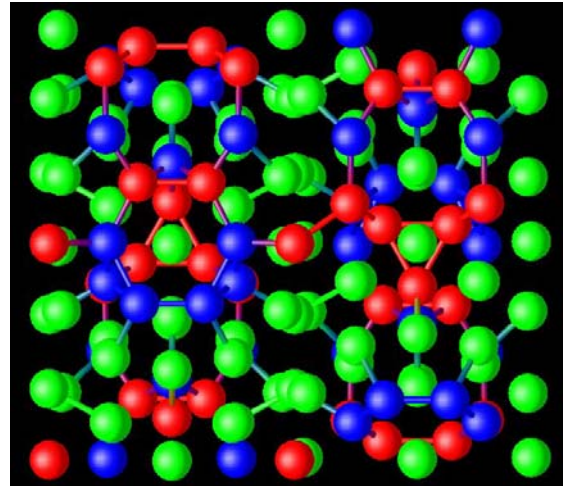


**Figure 3.** The structure of  $Mg_{84}(Al_xZn_{1-x})_{68}$  alloy in  $\phi$  phase with  $x = 0.4705$ . The green spheres represent Mg atoms, blue spheres Zn atoms, and red spheres Al atoms.

**Mechanical Properties of Mg-Based Alloys**

To obtain fundamental mechanical properties and attain proper stress levels for creep tests, tensile tests were carried out in the quasi-static strain rate regime. The tensile tests were performed at various strain rates of 0.0001, 0.001, and 0.01 per second, with different testing temperatures of room temperature and 150°C. The stress versus strain plots of the various base alloys under such test conditions are shown in Figure 4. The ultimate tensile stress and the flow stress level of the alloys strongly depend on the alloy composition, testing temperature, and strain rate. Not surprisingly, AZ91D possessed the highest tensile strength and the worst ductility among tested alloys. AM series Mg alloys are developed for and characterized by slightly reduced strengths with higher ductility and impact strength compared to AZ91D grade [27, 28, 29, 30], while AE series Mg alloys are developed for good ambient and elevated temperature properties and creep resistance [31, 32, 33, 34, 35]. The test results showed such characteristics.

Figure 5 provides fracture surfaces of the tensile tested specimens observed by SEM. The fractography reveals that fractures occurred in a brittle manner in all cases. The absence of shear lips on the edges of fracture surfaces, indicating a general lack of ductility, is noted. The features of the fracture surfaces are associated with shrinkage

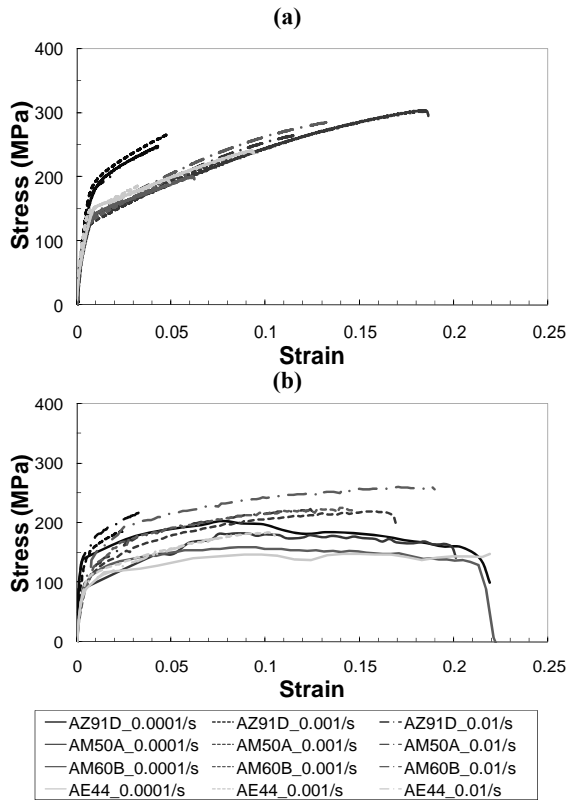


**Figure 4.** Stress versus strain plots of the Mg-based alloys obtained from quasi-static tensile tests at (a) room temperature and (b) 150°C.

cavities. Fracture surfaces contained many pores ranging from a few tens of microns to hundred microns in size. These cavities could have resulted from entrapped air being carried into the mold by undue turbulence during casting. In addition, granular secondary arms of dendrites can be seen on the fracture surfaces.

The creep behaviors of the base alloys were investigated to determine better ways for developing novel Mg alloys with improved creep resistance. Two experimental approaches, stress relaxation and creep tests, were used to obtain creep properties of the base alloys. The stress relaxation tests were carried out on an Instron machine at various temperatures (120, 150, and 200°C) after imposing prestrain of 0.02 and prestrain rate of 0.001/s before the stress relaxation process. Stress versus time plots of the base alloys obtained from the stress relaxation tests are given in Figure 6. For a given test condition, the peak stress obtained from AZ91D before the stress relaxation tests is the highest

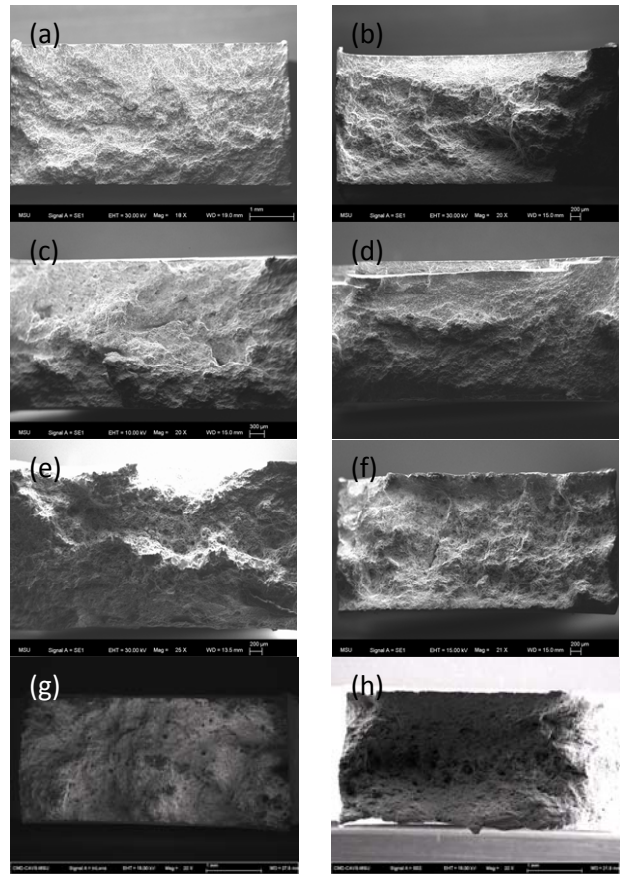


**Figure 5.** SEM fractography on the tensile tested specimens. (a) AZ91D, (b) AM50A, (c) AM60B, and (d) AE44 tested at room temperature; (e) AZ91D, (f) AM50A, (g) AM60B, and (h) AE44 tested at 150°C.

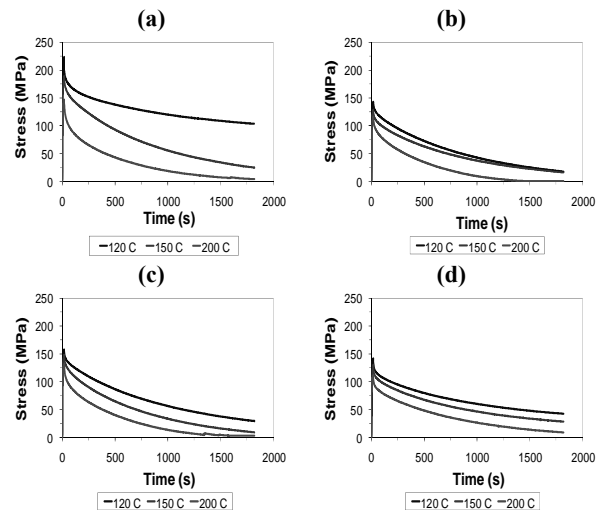


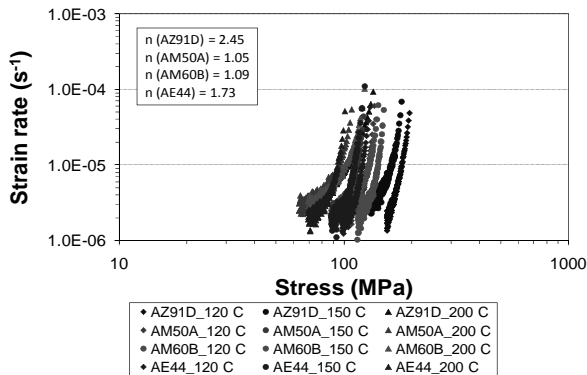
**Figure 6.** Stress versus time plots obtained from stress relaxation tests at various temperatures: (a) AZ91D, (b) AM50A, (c) AM60B, and (d) AE44.

among tested alloys, and this result is comparable to tensile test results. The peak stress and residual stress levels decrease with increasing testing temperature for any given test conditions.

The creep parameters for the base alloys obtained from stress relaxation tests can be extracted by fitting the data to a power-law creep equation [36]:

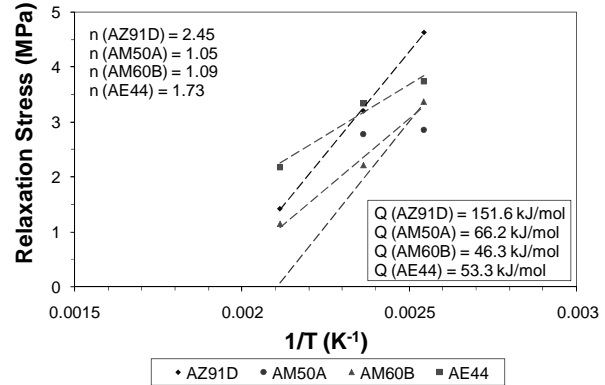
$$\dot{\gamma} = A\tau^n \exp\left(-\frac{Q_c}{RT}\right), \quad (2)$$

where  $\dot{\gamma}$  is the steady-state strain rate in creep,  $A$  is the material constant,  $\tau$  is the stress,  $n$  is the stress exponent,  $Q_c$  is the creep activation energy,  $R$  is the gas constant, and  $T$  is the absolute temperature. The relationship between strain rate and stress of the base alloys obtained from the stress relaxation part of the tests is depicted in Figure 7. The stress exponents that depend on the operating creep mechanisms are provided, and they are comparable to the stress exponents reported in the literature [37, 38, 39].



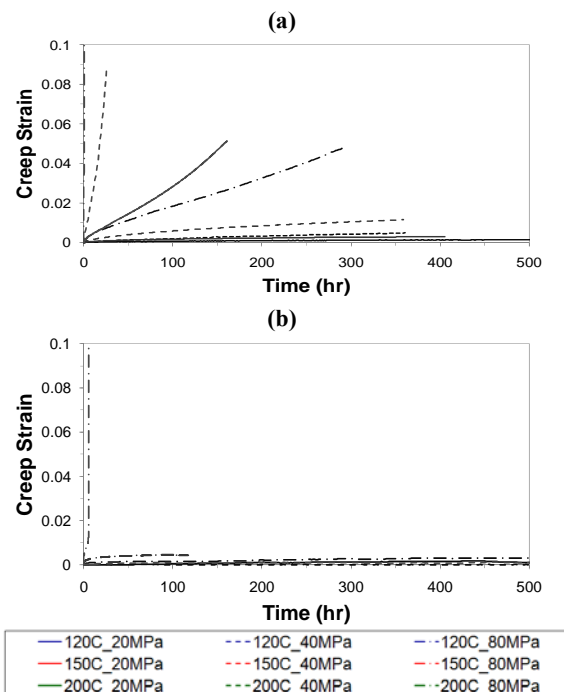
**Figure 7.** Relationship between strain rate in creep and stress obtained from the stress relaxation tests of various base alloys.

Figure 8 shows the relationship between peak stress and testing temperature using the data from Figure 7. The creep activation energy values obtained from stress relaxation tests are varied with respect to different compositions of the alloys. The dominant creep mechanism of the tested condition can be identified by comparing the experimentally obtained values of  $n$  and  $Q_c$  with those predicted because each creep mechanism predicts a unique range of those values [40, 41].



**Figure 8.** Relationship between peak stress and testing temperature obtained from the stress relaxation tests.

Creep test results obtained from ORNL creep test facilities are shown in Figure 9. Creep tests were performed at three different temperatures (120, 150, and 200°C) with three different stress levels (20, 40, and 80 MPa). Four creep tests (two low stress tests at 120 and 150°C) for AZ91D were discontinued after 500 hours of testing as the apparent steady state condition was achieved, whereas six tests were discontinued for AE44



**Figure 9.** Creep curves obtained from ORNL creep test facilities under various test conditions: (a) AZ91D and (b) AE44.

creep tests because no detectable creep deformation was observed under such test conditions.

Figure 10 provides a comparison of creep curves between AZ91D and AE44 tested at 200°C under stress of 80 MPa. Steady-state creep rate of AZ91D is much higher than that of AE44, and the rupture lifetime of AE44 is dramatically longer than that of AZ91D.

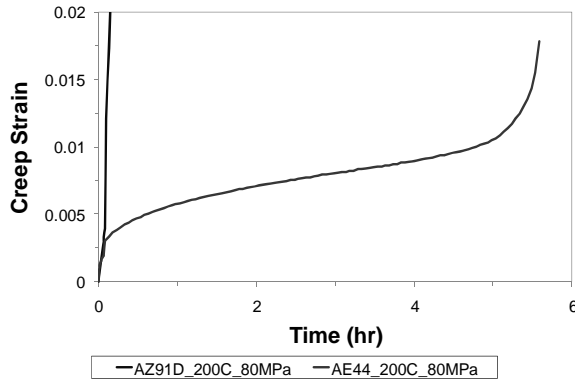


Figure 10. Comparison of creep curves between AZ91D and AE44 tested at 200°C under 80 MPa.

As to strengthening mechanisms of Mg-based alloy systems, to strengthen the Mg-Zn system, the alloy must be aged to increase hardness. The yield strength increases with hardness as the aging temperature increases. Using results for Mg-7 wt % Zn, the strength increases by 29.3% to 199.8 MPa at an aging temperature of 40°C.

Figure 11 shows the plot of aging temperature against composition of Zn. The data points in the plot correspond to peak hardness values found through literature review. The solvus lines were estimated by tracking the phases of the precipitates present at each of the data points. For instance, if the  $\beta_1'$  and  $\beta_2'$  phases both exist at a certain aging temperature and composition, this data point was assumed to lie between the solvus lines of  $\beta_1'$  and  $\beta_2'$ . Points lying on the solvus lines for the  $\beta_1'$  and  $\beta_2'$  phases were found in the literature for Mg-5 wt % Zn, and a point on the solvus line for the Guinier-Preston (GP) zone precipitates was found for Mg-5.53 wt % Zn. It should be noted that peak hardness is controlled by the  $\beta_1'$  and  $\beta_2'$  phases. These points were used as reference points

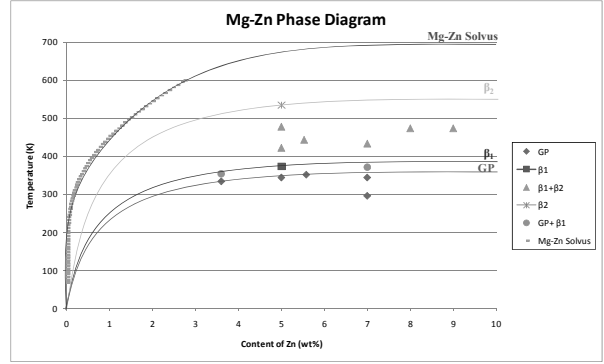


Figure 11. Metastable phase diagram for Mg-Zn: Aging temperature versus composition of Zn.

to draw the estimated solvus lines in Figure 12. We investigated the strengthening mechanisms of the Mg-Zn and Mg-Zn-Ca systems based on the experimental data in the literature. To strengthen the Mg-Zn system, the alloy must be aged to increase hardness. The yield strength increases with hardness as the aging temperature increases. Using results for Mg-7 wt % Zn, the strength increases by 29.3% to 199.8 MPa at an aging temperature of 40°C.

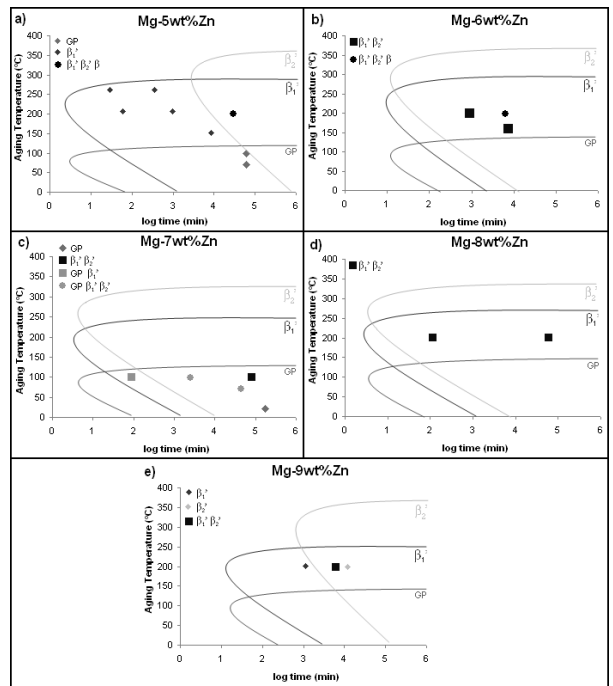


Figure 12. TTT diagrams for (a) Mg-5 wt % Zn, (b) Mg-6 wt % Zn, (c) Mg-7 wt % Zn, (d) Mg-8 wt % Zn, and (e) Mg-9 wt % Zn.

To characterize the time-temperature transformation (TTT) diagrams, data from the literature on the phases present at certain aging temperatures and aging times were plotted. Based on which phases were present at each point, the appropriate phase transformation lines were drawn.

Figure 12 shows the TTT diagrams for several compositions of the Mg-Zn system. In general, in the Mg-Zn system, at lower temperatures, GP zones form first, followed by the metastable  $\beta_1'$  and  $\beta_2'$  phases, and the stable  $\beta$  phase. The transformation lines were estimated using this general trend.

As shown in Figure 12(a), for the Mg-5 wt % Zn alloy, at lower temperatures the  $\beta_1'$  and  $\beta_2'$  phases do not seem to develop even after extended periods of aging. Also, it is reasonable to conclude that the  $\beta_1'$  phase will build up at aging temperatures higher than 150°C. At 200°C, the  $\beta_2'$  and  $\beta$  phases appear after 30,000 minutes of aging. It is clear as to when the  $\beta_1'$  phase is dominant.

The Mg-6 wt % Zn alloy is shown in Figure 12(b). The  $\beta_1'$  and  $\beta_2'$  phases were present in this alloy at an aging temperature of 200°C and an aging time of 900 minutes, which corresponds to peak hardness. As the alloy is overaged, the stable  $\beta$  phase begins to accumulate, resulting in decreased hardness.

For the Mg-7 wt % Zn alloy in Figure 12(c), after aging at a temperature of 98°C for 90 minutes, GP zones and the  $\beta_1'$  phases were observed. After aging for 2,400 minutes, the  $\beta_2'$  phase appears in addition to the GP zones and the  $\beta_1'$  phase. As the alloy is aged even more, at 84,000 minutes, the GP zones disappear leaving only the  $\beta_1'$  and  $\beta_2'$  phases present. It should also be noted that at ambient temperature aging, even after extended periods of aging, the  $\beta_1'$  and  $\beta_2'$  phases do not appear and only the GP zones are observed. Due to limited resources, only two data points were plotted for the Mg-8 wt % Zn alloy. The phases present in both data points were the  $\beta_1'$  and  $\beta_2'$  phases, as shown in Figure 12(d). The GP zone transformation line should lie below 200°C while the  $\beta_1'$  and  $\beta_2'$  lines should lie above 200°C.

## Conclusions

We applied the multi-objective optimization procedure to develop two new interatomic potentials for Zn and Mg-Zn based on FMEAM.

The structure of  $\text{Mg}_{84}(\text{Al}_x\text{Zn}_{1-x})_{68}$  alloy in ternary  $\phi$  phase has been determined from first-principles calculations.

The creep behavior of the Mg-based alloys was investigated using stress relaxation and long-time creep tests. We found that steady-state creep rate of AZ91D is much higher than that of AE44, and the rupture lifetime of AE44 is dramatically longer than that of AZ91D.

The strengthening mechanisms of the Mg-based alloy systems were investigated. The metastable phase diagrams with GP solvus and metastable precipitate solvus have been constructed. Preliminary TTT diagrams of Mg-based alloys have been estimated according to experimental information. These diagrams provide the basis for calibration of thermodynamic and kinetic modeling of precipitation strengthening in the Mg-based alloy systems.

## Presentations/Publications/Patents

1. B. Jelinek et al., "Modified embedded-atom method interatomic potentials for the Mg-Al alloy system," *Phys. Rev. B*, **75**, 054106 (2007).
2. J. Houze et al., "A multi-objective optimization procedure to develop modified-embedded-atom-method potentials: an application to magnesium," submitted to *Phys. Rev. B*, arXiv:0708.0075.
3. Shengjun Zhang and Gregory B. Olson, "3D-atom probe investigation of strengthening precipitates in a Mg-7Zn-3Al alloy," Preprint.
4. S. Groh et al., "Mobility of  $\langle a \rangle$  dislocations in Mg and Mg/Al alloys by molecular dynamic simulations," submitted to *Computational Materials Science*.
5. Amitava Moitra et al., "Force-matching embedded-atom-method potential for Zinc," to be submitted to *Phys. Rev. B*.

6. Amitava Moitra et al., “Adsorption of Zn atoms on Mg(0001) surface,” in preparation.
7. J. Houze et al., “First-principles calculation of the crystal structure of Phi phase in Mg-Zn-Al casting alloys,” in preparation.

## References

1. G. Olson, “Systems design of hierarchically structured materials: Advanced steels,” *Journal of Computer-Aided Materials Design*, **4**, p. 143 (1998).
2. G. Kresse and J. Furthmüller, “Efficient iterative schemes for ab initio total-energy calculations using a plane-wave basis set,” *Phys. Rev. B*, **54**, p. 11169 (1996).
3. W. Kohn and L. J. Sham, “Self-consistent Equations Including Exchange and Correlation Effects,” *Phys. Rev.*, **140**, p. A1113 (1965).
4. M. I. Baskes, “Modified embedded-atom potentials for cubic materials and impurities,” *Phys. Rev. B*, **46**, p. 2727 (1992).
5. M. S. Daw and M. I. Baskes, “Embedded-atom method: Derivation and application to impurities, surfaces, and other defects in metals,” *Phys. Rev. B*, **29**, p. 6443 (1984).
6. M. S. Daw and M. I. Baskes, “Semiempirical, Quantum Mechanical Calculation of Hydrogen Embrittlement in Metals,” *Phys. Rev. Lett.*, **50**, p. 1285 (1983).
7. P. E. Blöchl, “Projector augmented-wave method,” *Phys. Rev. B*, **50**, p. 17953 (1994).
8. G. Kresse and D. Joubert, “From ultrasoft pseudopotentials to the projector augmented-wave method,” *Phys. Rev. B*, **59**, p. 1758 (1999).
9. D. M. Ceperley and B. J. Alder, “Ground State of the Electron Gas by a Stochastic Method,” *Phys. Rev. Lett.*, **45**, p. 566 (1980).
10. J. P. Perdew and A. Zunger, “Self-interaction correction to density-functional approximations for many-electron systems,” *Phys. Rev. B*, **23**, p. 5048 (1981).
11. J. P. Perdew, K. Burke, and M. Ernzerhof, “Generalized Gradient Approximation Made Simple,” *Phys. Rev. Lett.*, **77**, p. 3865 (1996).
12. G. Kresse and J. Hafner, “Ab initio molecular dynamics for liquid metals,” *Phys. Rev. B*, **47**, p. 558 (1993).
13. Youhong Li et al., “Embedded-atom-method tantalum potential developed by the force-matching method,” *Phys. Rev. B*, **67**, p. 125101 (2003).
14. Xiang-Yang Liu et al., “EAM potential for magnesium from quantum mechanical forces,” *Modell. Simul. Mater. Sci. Eng.*, **4**, p. 293 (1996).
15. Seong-Gon Kim et al., “Task 4: Materials Design for Mg Alloys,” ORNL FY 2006–2007 Annual Report, Chaps. 4, pp. 28–45 (2007).
16. B. Jelinek et al., “Modified embedded-atom method interatomic potentials for the Mg-Al alloy system,” *Phys. Rev. B*, **75**, p. 054106 (2007).
17. R. Pasianot and E. J. Savino, “Embedded-atom-method interatomic potentials for hcp metals,” *Phys. Rev. B*, **45**, p. 12704 (1992).
18. R. Ramprasad and R. G. Hoagland, “Thermodynamic properties of small zinc clusters based on atomistic simulations,” *Modell. Simul. Mater. Sci. Eng.*, **1**, p. 189 (1993).
19. X.-Y. Liu et al., “Anisotropic surface segregation in Al-Mg alloys,” *Surf. Sci.*, **373**, p. 357 (1997).
20. D. Y. Sun et al., “Crystal-melt interfacial free energies in hcp metals: A molecular dynamics study of Mg,” *Phys. Rev. B*, **73**, p. 24116 (2006).
21. L. Bourgeois, B. C. Muddle and J. F. Nie, “The crystal structure of the equilibrium  $\phi$  phase in Mg–Zn–Al casting alloys,” *Acta Mater.*, **49**, pp. 2701–2711 (2001).
22. J. Houze et al., “A multi-objective optimization procedure to develop modified-embedded-atom-method potentials: an application to magnesium,” Preprint, arXiv:0708.0075.
23. Amitava Moitra et al., “Force-matching embedded-atom-method potential for Zinc,” to be submitted to *Phys. Rev. B.*, (2008).

24. H. M. Ledbetter, *Journal of Physical and Chemical Reference Data*, **6**, p. 1181 (1977).
25. M. J. Mehl, B. M. Klein, and D. A. Papaconstantopoulos, in "Intermetallic Compounds: Principles and Applications," edited by J. H. Westbrook and R. L. Fleischer John Wiley & Sons Ltd., London, 1994.
26. P. Lianga et al., "Experimental investigation and thermodynamic calculation of the Al-Mg-Zn system," *Thermochimica Acta*, **314**, pp. 87–110 (1998).
27. W. Blum et al., "Independent deformation of the magnesium alloys AS21 and AZ91," *Zeitschrift für Metallkunde*, **88**, p. 636 (1997).
28. W. K. Miller, "Creep of die cast AZ91 magnesium at room temperature and low stress," *Metall. Trans. A*, **22**, p. 873 (1991).
29. K. Pettersen and S. Fairchild, "Stress relaxation in bolted joints of die cast magnesium components," SAE Tech. Paper 970326 (1997).
30. B. R. Powell et al., "Microstructure and creep behavior in AE42 magnesium diecasting alloy," *J. Electrochem. Soc.*, **54**, p. 34 (2002).
31. I. A. Anyanwu, Y. Gokan, A. Suzuki, S. Kamado, Y. Kojima, S. Takeda, and T. Ishida, "Effect of substituting cerium rich mischmetal with lanthanum on high temperature properties of die-cast Mg-Zn-Al-Ca-RE alloys," *Mater. Sci. Eng. A*, **380**, 93 (2004).
32. P. Bakke, K. Pettersen, and H. Westengen, "Improving the strength and ductility of magnesium die casting alloys via rare earth addition," *JOM*, **46** (2003).
33. B. Mordike, "Development of highly creep resistant magnesium alloys," *J. Mater. Process. Technol.*, **117**, p. 391 (2001).
34. I. P. Moreno et al., "Microstructural characterization of a die cast magnesium-rare earth alloy," *Scr. Mater.*, **45**, p. 1423 (2001).
35. L. Y. Wei and G. L. Dunlop, "The solidification behavior of Mg-Al-rare earth alloys," *J. Alloys Compd.*, **232**, p. 264 (1996).
36. T. H. Courtney, *Mechanical Behavior of Materials*, McGraw-Hill, Inc., New York, 1990.
37. *Metals Handbook*, 9th ed., ASM, Metals Park, Ohio, 1985.
38. F. von Buch and B. L. Mordike, "Microstructure, mechanical properties and creep resistance of binary and more complex magnesium scandium alloys," Mg Alloys & their App. Conf. 1998, 145, Wolfsburg, Germany (1998).
39. V. Sklenicka, M. Pahutova, and T. G. Langdon, "Creep of reinforced and unreinforced AZ91 magnesium alloys," *Key Eng. Materials*, **171–174**, p. 593 (2000).
40. M. F. Ashby and D. R. H. Jones, *Engineering Materials: an Introduction to Their Properties and Applications*, (Pergamon Press, Oxford, 1982).
41. G. E. Dieter, *Mechanical Metallurgy*, McGraw-Hill, Inc., London, 1988.



## **J. High Throughput Isotopic Diffusion Databases for Integrated Computational Materials Engineering**

*Nagraj S. Kulkarni*

*Research Assistant Professor*

*Department of Materials Science & Engineering*

*Center for Materials Processing*

*University of Tennessee,*

*Knoxville, TN 37996-0816*

*Monolithic Systems Development Group*

*Oak Ridge National Laboratory*

*Measurement Science & Systems Engineering Division*

*Oak Ridge, TN 37831-6006*

*(865)576-0592; fax: (865)576-2813, e-mail: kulkarnins@ornl.gov*

*Technology Area Development Manager: Joseph A. Carpenter*

*(202) 586-1022; fax: (202) 586-1600; e-mail: joseph.carpenter@ee.doe.gov*

*Field Technical Monitor: C. David Warren*

*(865) 574-9693; fax: (865) 574-6098; e-mail: warrencd@ornl.gov*

*Participants:*

*Peter Todd*

*Oak Ridge National Laboratory*

*Professor Yongho Sohn*

*University of Central Florida*

---

*Contractor: Oak Ridge National Laboratory (ORNL)*

*Contract No.: DE-AC05-00OR22725*

---

### **Objectives**

- Develop a tracer-diffusion database for magnesium-rich phases in the magnesium-aluminum-zinc-manganese (Mg-Al-Zn-Mn) system using secondary ion mass spectrometry (SIMS) for measurements of diffusion depth profiles of isotopes. Initial year focus will be on the Mg-Al-Zn system.
- Upgrade the SIMS instrument (Cameca IMS 4f ion microscope) at ORNL for automated and reliable isotopic ratio depth-profile measurements.
- Use an intrinsic diffusion simulation to assess diffusion formalisms needed for obtaining practical interdiffusion information from tracer-diffusion and thermodynamic databases. Diffusion formalisms include the Darken, Manning, and Moleko formalisms.

### **Approach**

- Establish procedures for thin-film isotope deposition and SIMS measurements of diffusion depth profiles in a few select Mg alloy samples annealed at different temperatures. Analyze diffusion profiles to determine tracer diffusivities.

- Prepare homogeneous single-phase compositions in the Mg-rich phase of ternary subsystems such as Mg-Al-Zn and Mg-Al-Mn and a few in the quaternary Mg-Al-Zn-Mn. Deposit thin films of stable isotopes (Mg, Zn) of the primary elements and anneal at different temperatures and times. Analyze diffusion data using SIMS to obtain Mg and Zn tracer-diffusion coefficients for various compositions as a function of temperature.
- Construct a tracer-diffusion database for Mg and Zn in this system by fitting tracer-diffusion data as a function of composition and temperature using polynomial or other suitable functions.
- Conduct interdiffusion and intrinsic diffusion measurements using diffusion couples.
- Further develop intrinsic diffusion simulations that can take tracer-diffusion and thermodynamic data as input and provide interdiffusion and intrinsic diffusion data as output in order to compare them with experimental interdiffusion and intrinsic diffusion measurements. Collaborate with leading theoreticians in diffusion to further refine formalisms.

### Accomplishments (since July 2008)

- **Initiated upgrade of Cameca IMS 4f ion microscope for SIMS.** A primary requirement of our project is the capability to quickly and accurately measure isotopic ratios in Mg samples using SIMS. The SIMS instrument at ORNL (Cameca IMS 4f ion microscope) is being upgraded for the high sample load of this project (initially with hardware improvements, to be followed by method and automated software improvements).
- **Initiated assessment of diffusion formalisms.** To use tracer-diffusion databases for prediction of interdiffusion behavior in the presence of concentration or chemical potential gradients, the connection between tracer and interdiffusion as embodied in the Darken-Manning formalisms needs to be utilized. Recently, the Darken-Manning formalisms for a test copper-nickel-zinc (Cu-Ni-Zn) system at 900°C were evaluated using the intrinsic diffusion simulation. Preliminary simulations indicated that the Manning formalism was slightly better than the Darken formalism though none of these formalisms provided an ideal fit. More detailed simulations and analyses are in progress at the present time.

### Future Direction

- Complete initial upgrade of ORNL SIMS system (Cameca IMS 4f), and test the University of Central Florida (UCF) SIMS system (Cameca IMS 3f) for isotopic ratio measurements in select Mg alloy samples.
- Once preliminary SIMS measurements are confirmed, begin sample preparation in Mg-rich phase of Mg-Al-Zn system and proceed with tracer-diffusion database construction for ternary systems.
- Assess the Darken and Manning formalisms at various temperatures in face-centered cubic (fcc) Cu-Ni-Zn. Incorporate Moleko formalism in the diffusion simulation if results in the test Cu-Ni-Zn system show improvement over the Darken-Manning formalisms.
- Evaluate project and funding requirements for tracer-diffusion measurements of radioactive isotopes of Al and Mn in the Mg-Al-Zn and Mg-Al-Mn ternary systems.

---

### Introduction

The vision of the Department of Energy Integrated Computational Materials Engineering (ICME) project (see report 6G) is to initiate and coordinate a multiorganizational effort whose goal is to develop an integrated suite of validated computational materials modeling tools that are linked to analysis systems used in manufacturing as well as engineering design [1]. In short, the goal is to provide a quantitative linkage between the processing, microstructure, and properties of a material for the desired application (e.g.,

Mg-based light-metal alloys used in the automotive industry). Improvement in the ICME approach will require continued improvement both in theory and in the associated modeling within the vast array of tools currently available and those still in need of development. Knowledge of fundamental materials properties, thermodynamics, and kinetics in the form of reliable databases are the foundations on which the ICME approach is based. These are expected to be incorporated in the task on cyber infrastructure within the ICME project. A gap in the

understanding of any one of these may dramatically reduce the effectiveness of, adaptability of, and confidence within the engineering community in the ICME effort. While great strides have been made in the development of reasonably robust thermodynamic databases over the course of the past 25 years, the same cannot be said for diffusion databases. The reasons have partly to do with the lack of fundamental (tracer) measurements of diffusion in binary or multicomponent systems; the limited research resources available for such studies; and the lack of clarity in using the appropriate theoretical, experimental, and modeling tools necessary for developing robust diffusion databases that are valid regardless of the driving forces (e.g., concentration, temperature, stress gradients) causing diffusion.

This project aims at developing a tracer-diffusion database in Mg-based light-metal alloy systems. The safety issues that have hampered previous tracer-diffusion measurements based on radioactive tracers are somewhat avoided in this project with the use of *stable isotopes* for most elements in this study (except Al and Mn for which radioactive isotopes are needed). Homogeneous single-phase samples in the Mg-Al-Mn system will be prepared using conventional techniques, stable isotopes of these elements will be deposited in the form of thin films on these samples, and the measurement of isotopic diffusion profiles of stable isotopes in these samples after diffusion annealing will be conducted using automated SIMS facilities either at ORNL or UCF. A combined tracer-diffusion and thermodynamic database, which is continually updated by participants during the course of the Mg-ICME project, will provide the required interdiffusion information for the other modeling tasks in this program. More rigorous application of the phenomenological theory connecting tracer and interdiffusion or intrinsic diffusion behavior can be obtained using the Manning random alloy model [2], rather than the Darken model [3], or using the more recent Moleko formalism [4].

The first year of this study will focus on isotopic-diffusion measurements in the Mg-Al-Zn system, which is the base system for commercial AZ (i.e., Mg-Al-Zn) alloys. Future work beyond this

ternary will include studies in the Mg-Al-Mn ternary and Mg-Al-Zn-Mn alloy systems. Additionally, various diffusion formalisms will be evaluated for the test Cu-Ni-Zn system (for which a tracer-diffusion database already exists). The formalisms will then be evaluated for the Mg tracer-diffusion database.

### **Project Background**

Current diffusion database efforts are based on an approach developed by John Agren and others as part of the diffusion software DICTRA (Diffusion Controlled TRAnsfOrmations) [5]. The foundation of this approach is the Darken version of the intrinsic diffusion flux in a multicomponent system with  $n$  components:

$$J_k = - \sum_{i=1}^n L_{ki} \frac{\partial \mu_i}{\partial x} = -L_{kk} \frac{\partial \mu_k}{\partial x} \quad (1)$$

$$J_k = -c_k M_k \frac{\partial \mu_k}{\partial x} \dots (L_{ki} = 0, k \neq i) (k = 1, 2, \dots, n)$$

By ignoring the cross terms in the matrix of phenomenological diffusion coefficients  $L_{ki}$ , the above simplified version of the formalism used by DICTRA is obtained. In this expression, the flux  $J_k$  of a component is dependent only on the diagonal term  $L_{kk}$ , which in turn is related to the “mobility” of component  $k$ ,  $M_k$ . In the simplified form of the above equation, the driving force for the intrinsic flux of a component is provided by the chemical potential gradient  $\partial \mu_k / \partial x$  of that component. From the Darken theory, the connection between  $L_{kk}$  or  $M_k$  and the tracer-diffusion coefficient  $D_k^*$  is

$$L_{kk} = c_k M_k = \frac{c_k D_k^*}{RT} \quad (2)$$

Originally, the Darken theory connecting the mobility to the tracer-diffusion coefficient was proposed for binary systems. In Eq. (2), it has been extended to multicomponent systems as well. In principle, if the tracer-diffusion coefficients (i.e., the diffusion of an isotope of a component in a homogeneous system) in a system are known, the entire matrix of phenomenological coefficients for that system can be determined (*without ignoring the cross terms—i.e., with no assumptions*) provided the thermodynamics of that

system are known, which is expected to be the case for the current Mg alloy system because a thermodynamic database is already available and is being continually updated. However, because tracer-diffusion experiments are difficult to perform (tracers typically used are radioactive isotopes) and such data are not readily available, the above Darken assumption [Eq. (2)], inherent in the DICTRA formalism, is needed to determine unknown mobilities from diffusion data obtained through conventional interdiffusion experiments. The combination of mobilities obtained from tracer-diffusion data and those obtained from interdiffusion and intrinsic-diffusion experiments are typically used in an optimization process to develop a functional form of a mobility database within the DICTRA formalism [5, 6]. While the assumptions inherent in the DICTRA formalism are well known, the approach nevertheless appears to have provided a practical path toward developing diffusion databases within acceptable margins of error [6]. However, for developing reliable diffusion databases using this formalism, tracer-diffusion information is still necessary for most compounds and phases in the system of interest. This means for compounds or phases in new systems that have not been previously studied, the limiting factor in the development of dependable diffusion databases is the availability of tracer-diffusion data. Additionally, because the DICTRA approach is dependent upon a thermodynamic database for the construction of a mobility database (because converting interdiffusion information to mobilities requires thermodynamic information), the mobility database is not independent of the thermodynamic database. This means that alternate thermodynamic databases cannot be straightforwardly used for diffusion analysis and modeling with the existing mobility database.

### **Approach**

The approach proposed at ORNL offers a robust procedure for developing tracer-diffusion databases using SIMS measurements of the concentrations or concentration ratios of stable isotopes in homogeneous Mg-based light-metal alloy systems. The important point to be noted here is that, unlike tracer-diffusion studies in the past where the use of radioactive isotopes meant

that such studies required several years of effort and considerable expense even for limited data, in the present case stable isotopes are used instead, and their diffusion profiles are measured using SIMS techniques [7] whose resolution and accuracy have improved significantly within the past 5–10 years. The advances in SIMS techniques that now permit trace amounts of stable isotopes to be detected enable the use of thin-film or Fick's type solutions to determine the tracer diffusivity that are only valid for trace amounts of isotopes in homogeneous phases.

Unfortunately, the elements Al and Mn do not have any known stable isotopes; hence, for these elements, radioactive isotopes have to be used. However, SIMS can still be used for the tracer-diffusion measurements as before. One advantage of using SIMS over radiation measurement techniques for the radioactive isotope of Al is that the reduced activity of the isotope is actually not a hindrance for SIMS measurements [8]. In addition, safety requirements are likely to be less severe though a more detailed analysis remains to be performed. Because of the high costs of the Al radioactive isotope and the associated safety requirements for handling radioactive isotopes, a separate program request for such experiments will be needed.

An important advantage of a tracer-diffusion database over a mobility database is that the former is independent of the thermodynamic database; hence, the same tracer-diffusion database can be used with a variety of thermodynamic databases for analyzing diffusion problems.

### **Progress in Fiscal Year 2008 (July–September)**

#### **SIMS Upgrade**

An important requirement of our project is the ability to measure isotope ratio depth profiles using the SIMS facility at ORNL. Therefore, the ORNL SIMS instrument (Cameca IMS 4f ion microscope, Figures 1 and 2) is initially being upgraded for the high sample load of this project with hardware improvements, to be followed by method and automated software improvements. Completed upgrades include improved pumping of

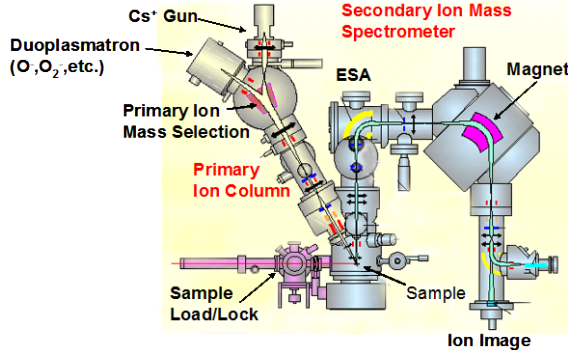


**Figure 1.** Diagram of ORNL Cameca IMS 4f SIMS system that is ideally suited for isotope ratio diffusion depth-profile measurements.



**Figure 2.** ORNL Cameca IMS 4f SIMS system currently being upgraded for rapid isotopic ratio diffusion depth-profile measurements.

the secondary ion source, permitting a vacuum of  $10^{-11}$  torr. This level of vacuum virtually eliminates interference caused by formation of secondary ion hydrides, which in fact are the principle interferants in isotope ratio measurements. Pending upgrades include integration of optical and electronics microscopic systems with the secondary-ion microscope systems of the Cameca. These upgrades will permit automated determination of exactly where on a sample measurements are being made at any given time.

### Assessment of Diffusion Formalisms

A test of different diffusion formalisms connecting tracer diffusion to interdiffusion requires reliable tracer-diffusion and thermodynamic databases. The Cu-Ni-Zn system is one of the few systems where an excellent tracer-diffusion database is available [9]. A thermodynamic model for this

system is also available [10]. Thus, the system was chosen as a test case to evaluate the diffusion formalisms, including the Darken and Manning formalisms. An intrinsic-diffusion simulation [11] that can take the available tracer and thermodynamic information as input and provide the required interdiffusion and intrinsic-diffusion information (e.g., concentration profiles, composition paths, lattice or Kirkendall shifts) as output was used for this assessment.

### Darken

In the extended version of the Darken or mobility formalism to multicomponent systems, the cross terms in the matrix of phenomenological coefficients are ignored [see Eq. (1)]. The mobility of a component is related to its tracer-diffusion coefficient as shown in Eq. (2). The resultant multicomponent intrinsic flux expression for a component is

$$J_i = \frac{-D_i^*}{V} X_i \frac{\partial \ln a_i}{\partial x} \quad (1)$$

where  $D_i^*$  is the tracer-diffusion coefficient,  $X_i$  is the mole fraction,  $V$  is the molar volume, and  $a_i$  is the activity of component  $i$  in this system. In terms of the thermodynamic factors, the flux is expressed as

$$J_i = \frac{-D_i^*}{V} X_i \left( \frac{\Phi_{ii}}{X_i} \frac{dX_i}{dx} + \sum_{j=1 \neq i}^{c-1} \frac{\Phi_{ij}}{X_j} \frac{dX_j}{dx} \right) \quad (2)$$

where the thermodynamic factors  $\Phi_{ij}$  are defined by

$$\Phi_{ij} = \frac{d \ln a_i}{d \ln X_j} \quad (3)$$

The thermodynamic factors in turn can be obtained in analytical form using the excess Gibbs energy function for face-centered cubic (fcc) Cu-Ni-Zn as a function of composition and temperature. The tracer-diffusion coefficients are available in a convenient form at 900°C [10]:

$$\begin{aligned} \ln D_{Cu}^* &= -3.53 X_{Ni}^{1.16} + 3.6 X_{Zn}^{1.02} - 9.46 \\ \ln D_{Ni}^* &= -4.05 X_{Ni}^{1.3} + 3.28 X_{Zn}^{1.07} - 9.96 \quad (4) \\ \ln D_{Zn}^* &= -3.2 X_{Ni}^{1.16} + 5.21 X_{Zn}^{1.25} - 9 \end{aligned}$$

Using the above tracer functions and thermodynamic data as input to the diffusion simulation [11], the outputs of the diffusion simulation were compared with the experimental measurements in diffusion couples prepared by Wan [9]. A few experimental and simulated composition paths are provided in Figures 3 and 4.

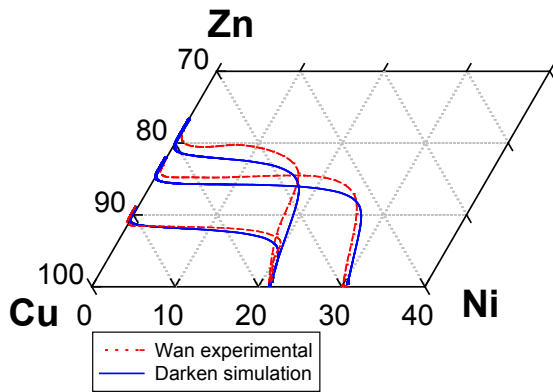


**Figure 3.** Experimental and simulated composition paths in fcc Cu-Ni-Zn at 900°C using the Darken formalism.

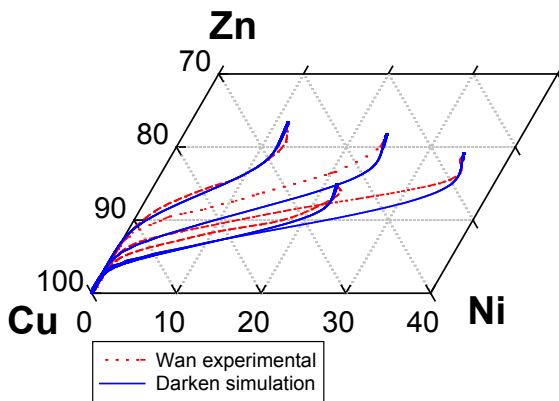


**Figure 4.** Additional experimental and simulated composition paths in fcc Cu-Ni-Zn at 900°C using the Darken formalism.

**Manning**

For a multicomponent system consisting of *n* components, the intrinsic flux can be expressed in terms of the phenomenological coefficients (*L<sub>ij</sub>*'s) as follows:

$$J_i = -L_{ii} \frac{\partial \mu_i}{\partial x} - \sum_{j=1, j \neq i}^n L_{ij} \frac{\partial \mu_j}{\partial x} \quad (5)$$

The diagonal and the nondiagonal phenomenological coefficients are related to the tracer-diffusion coefficients by the relations provided by Manning [2]:

$$L_{ii} = \frac{X_i D_i^*}{VRT} \left( 1 + \frac{2X_i D_i^*}{M_o \sum_{k=1}^n X_k D_k^*} \right) \quad (8)$$

$$L_{ij} = \frac{X_i D_i^*}{VRT} \frac{2X_j D_j^*}{M_o \sum_{k=1}^n X_k D_k^*} \dots (i \neq j)$$

where *M<sub>o</sub>* is a geometric constant for the given crystal structure (7.15 for fcc structures) and *R* is the universal gas constant. The chemical potential gradients in Eq. (7) can be expressed in terms of the thermodynamic factors as in the Darken case. The resultant expression can then be used to test the Manning relations for the fcc Cu-Ni-Zn system at 900°C as was done previously for the Darken relations.

The simulated composition paths using the Manning relations were found to be very similar to those obtained with the Darken simulation and are hence not shown here. The Kirkendall shifts for various diffusion couples using both the Darken and Manning formalisms are compared in Figure 5. Though more simulations are needed to confirm the present findings, it is evident from the preliminary simulations that the Manning relations appear to be slightly better than the Darken

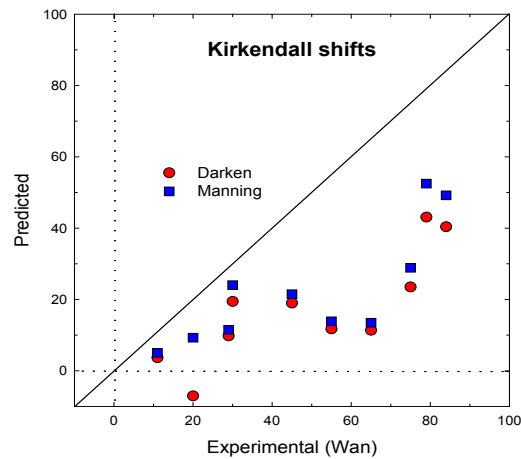


**Figure 5.** Experimental and simulated Kirkendall shifts in fcc Cu-Ni-Zn at 900°C using the Darken and Manning formalisms.

relations, especially for the Kirkendall shifts. However, neither the Darken nor Manning formalisms could provide a good match to the experimental Kirkendall shifts. Thus there appears to be a need to explore alternate formalisms such as the Moleko formalism [4] in the future.

Additionally, a test of diffusion formalisms in hexagonal close-packed systems, such as the current Mg alloy systems, will provide further evidence for the choice of the most suitable diffusion formalism.

### **Conclusions**

A Cameca IMS 4f SIMS system is currently being upgraded at ORNL for reliable automated isotopic ratio depth profile measurements in Mg alloy systems.

Preliminary tests of diffusion formalisms in the Cu-Ni-Zn system indicated that while the predicted composition path profiles provided a reasonable representation of experimental composition paths, the simulated Kirkendall shifts were underestimated in comparison to the experimental ones.

### **Presentations/Publications/Patents**

1. N. S. Kulkarni, P. J. Todd, and Y. H. Sohn, "Assessment of Diffusion Formalisms for Databases," invited talk presented at the *Symposium on Fundamentals & Characterization: Phase Stability, Diffusion Kinetics & Their Applications (PSDK-III)* at the Materials Science & Technology Conference (MS&T08), Pittsburgh, Pennsylvania, October 5–9, 2008.

2. N. S. Kulkarni, P. J. Todd, Y. H. Sohn, "Diffusion Databases for Mg-ICME," presented at the TMS 2008 Annual Meeting, New Orleans, Louisiana, March 12, 2008.

### **References**

1. J. Allison, D. Backman, and L. Christodoulou, *J. Met.*, p. 25 (Nov. 2006).
2. J. R. Manning, *Met. Trans.* **1**, p. 499 (1970).
3. L. S. Darken, *Trans. AIME* **175**, p. 184 (1948).
4. L. K. Moleko, A. R. Allnatt, and E. L. Allnatt, *Phil. Mag. A* **59**, p. 141 (1989).
5. J. O. Andersson et al., *Calphad* **26**, p. 273 (2002).
6. C. E. Campbell, W. J. Boettinger, and U. R. Kattner, *Acta Mat.* **50**, p. 775 (2002).
7. R. A. De Souza et al., *Sol. State Ionics* **176**, p. 1465 (2005).
8. P. Fielitz et al., *Sol. State Ionics* **177**, p. 493 (2006).
9. C. C. Wan, Ph.D. dissertation, University of Florida, Gainesville, 1973.
10. M. Jiang et al., *J. Phys. Chem. Sol.* **66**, p. 246 (2005).
11. N. S. Kulkarni and R. T. DeHoff, *Acta Mat.* **53**, p. 4097 (2005).

## K. Cyberinfrastructure

*Principal Investigator: Tomasz Haupt*

*Center for Advanced Vehicular Systems*

*Mississippi State University*

*P.O. Box 5405, Mississippi State, MS 39762*

*(662) 325-4524; fax: (662)325-5433; email: haupt@cavs.msstate.edu*

*Co-Principal Investigator: Ricolindo Carino*

*Center for Advanced Vehicular Systems*

*Mississippi State University*

*P.O. Box 5405, Mississippi State, MS 39762*

*(662) 325-5579; e-mail: rlc@cavs.msstate.edu*

*Co-Principal Investigator: Anand Kalyanasundaram*

*Research Associate, Center for Advanced Vehicular Systems*

*Mississippi State University*

*P.O. Box 5405, Mississippi State, MS 39762*

*(662) 325-5458; e-mail: anand@cavs.msstate.edu*

*Technology Area Development Manager: Joseph A. Carpenter*

*(202) 586-1022; fax: (202) 586-1600; e-mail: joseph.carpenter@ee.doe.gov*

*Field Project Officer: Aaron D. Yocum*

*(304) 285-4852; fax: (304) 285-4403; e-mail: aaron.yocum@netl.doe.gov*

---

*Contractor: Mississippi State University (MSST)*

*Contract No.: DE-FC26-06NT42755*

---

### Objective

- Design and develop a cyberinfrastructure to exploit the recent transformative research in material science involving multiscale physics-based predictive modeling, multiscale experiments, and design. More specifically, the creation of the cyberinfrastructure will result in the development of the “community of practice” portal that allows development and integration of multiscale physics-based materials models for selected properties and processes, in the context of United States Automotive Materials Partnership (USAMP) three-nation Magnesium Front-End Research and Development pilot project.

### Approach

- The development of the cyberinfrastructure to support the capabilities described above will leverage tools, technologies, and software approaches developed by other large-scale scientific cyberinfrastructures, in particular GEONGrid (<http://www.geongrid.org/>) and NEESit (<http://it.nees.org/>). Much of the foundation of the infrastructure is common across domains (security, grid integration, etc) and can serve to bootstrap this project to delivering an initial working solution in a relatively short time frame. Some initial customization was needed to support the unique aspects of this project. After the initial system had been developed, many of the advanced capabilities of the system required additional software development and customization and entirely new development to support additional features. Hence, we are proceeding with a two-stage development model: phase one was to initial leverage of existing software and tools to bring up a working software infrastructure, and phase two was to evaluate and further develop missing or insufficient software, as needed, to support the project requirements.



- The actual development and deployment of the cyberinfrastructure was driven by the requirements and early feedback generated by the engineering community, composed of MSST researchers performing other tasks of this project, as well as researchers and engineers involved in the MFERD/ICME project. Frequent interactions between researchers and students developing the cyberinfrastructure with the community (as defined above) resulted in modifications of the initial plans, such as adding new elements to the cyberinfrastructure and changing the priorities of the development and deployment of the cyberinfrastructure components. The changes reflect a close collaboration between tasks and the pursuit to maximize the benefits of the cyberinfrastructure to the end user.

## Accomplishments

- **Task 1:** Identify, acquire, and deploy servers supporting simple object access protocol (SOAP), Web Services Description Language (WSDL), and integrating Message Oriented Middleware. This task has been completed. We selected and installed: Globus Toolkit 4 grid computing (remote access to resources, security); Apache/Tomcat Web Server with support for J2EE (Java Server Pages), GridSphere (portlet container), JBoss (Enterprise JavaBeans container), Axis (SOAP and WSDL container), ServiceMix (Java Business Integration—Service Bus) and Microsoft's SharePoint Server for the deployment of USAMP community portal. This subtask has been completed during year 1 of this project. Year 2 activities were limited to the maintenance of the deployed servers and fine-tuning of their configurations.
- **Task 2:** Create a virtual organization encompassing all partners involved in the project research and implement authentication, authorization, and auditing mechanisms according to policies negotiated with the system administrators. This task has been modified. At this phase of the project there is no need for resource sharing (e.g., running jobs on machines outside MSST campus or allowing non-MSST employees or students to run jobs on MSST systems). On the other hand, the USAMP project mandates the development of an electronic "community of practice" web site, which allows for the development and integration of multi-scale physics-based material models for selected properties and processes. To this end, we deployed the Microsoft's SharePoint Server configured to be accessible from any place in the world, with all necessary security settings protecting against misuse and cyber-vandalism. The portal has been made available to the users participating in the USAMP MFERD project. Most of this effort has been completed during year 1. During year 2, the SharePoint server has been filled with contents, closely collaborating with Eric Nyberg and Robert McCune, who are managing the Web Sites for MFERD and ICME, respectively. Eventually, the server will provide a single point of access to all services rendered by the cyberinfrastructure, through the contents aggregation. The current and future activity focuses the maintenance of the servers. As of October 2007, the MFERD/ICME (<http://carload.hpc.msstate.edu>) portal has 100+ registered users from the U.S., Canada, and China.
- **Task 3:** Develop and deploy services for secure access to remote resources (job submission to high performance platforms, job monitoring, access to file systems and databases). Most of the services have been developed and utilized in Task 5. This task has been essentially completed in year 1 (back-end and middle-tier support). In year 2, the job submission service has been extended for running MATLAB-based applications, as required by the modified task 5 described below.
- **Task 4:** Develop support for service orchestration and workflows. In year 1, the service orchestration is achieved by employing the Service Bus and used in Task 5. The interfaces for composing workflows remain to be implemented. This means that Task 4 is 50% completed. Since the direct support for multiscale simulations has been postponed to the later phases of the project, no progress has been achieved in year 2.
- **Task 5:** Develop specific services supporting online repository of material properties, design optimizations, and multiscale simulations. This builds on the results of activities within Tasks 1, 3, and 4, and is the subject for the integration efforts in Tasks 2 and 7. Most of the year 2 achievements have been accomplished within this task and task 7, even though the direct support for multiscale simulations has been postponed to the later phases of the project. Based on the metadata and storage services developed during year 1 (presented at 7<sup>th</sup> International Conference on Grid Computing, Barcelona 2006 and International Conference on Grid Computing and Applications, Las Vegas 2007), a repository of material properties has been developed and made available to test users (both at MSST and ICME). The repository is online at <http://cgg.hpc.msstate.edu/cggportlets> and through ICME site. The repository is comprised of a database of experimental data (stress-strain, strain-life, and microstructure images), a database of material constants (for damage and multistage fatigue models), and is seamlessly integrated with online tools (Damage Fit, Multistage Fatigue Fit, and Microstructure Analyzer) for

calibrating model constants from experimental data. The seamless integration means a full support for searching experimental data directly from the tools interfaces, transferring analysis results from one tool to another (e.g., grain statistics to damage or fatigue model), and storing the analysis results into the material constants database so that they can be retrieved a latter time, perhaps by a different user, and formatted according to specification of a finite element analysis (FEA) application, such as ABAQUS. The concept and implementation of the repository has been presented and discussed during ICME meetings and The Minerals, Metals, and Materials Society (TMS) annual meetings in Orlando (2007) and New Orleans (2008). Independently, a preview of the Flexible Advanced Metamodeling Estimator (FAME) for automatic generation of best metamodel-based surrogate model has been developed and made available for testing and validation (see report 6.L, FY 2008 Progress Report on “Simulation-Based Design Optimization”). FAME is comprised of integrated web services for the creation of metamodels applying different algorithms, such as radial basis functions (RBFs) or response surface methodology (RSM), and web services for aggregating the metamodels into metamodel assemblies.

- **Task 6:** Develop a resource management system for multiscale simulations. During year 1, we have developed an overlay scheduler to support adaptive multiscale simulations (presented at TMS 2006). No further development has been made during year 2.
- **Task 7:** Integrate all components into a single system (cyberinfrastructure). Verify and validate the system and improve the graphical user interfaces (GUIs), performance, and robustness. The year 2 achievement here is applying a service oriented architecture (SOA) involving web services and service bus (cf, task 1), for a seamless integration of independent, loose-coupled back-end services, including MATLAB-based modules, into integrated sub-systems: the repository of material properties and FAME. The initial Java-based GUI has been abandoned and replaced by lightweight, rich user interfaces implemented in AJAX (asynchronous JavaScript and XML), promoting service aggregations (mashups), and enhancing the end user experience (faster response, more context sensitivity) on one hand and simplifying the maintenance, as well as extensibility of the systems.

## Future Direction

- During the first year, the basic infrastructure has been created that forms a solid foundation for creating the cyberinfrastructure for engineering virtual organizations. Furthermore, preliminary implementation of vital components has been done, in particular support for design optimizations and service-based repository of material properties. During year two, the infrastructure has been used to develop and deploy two integrated applications: the repository of material properties and FAME.
- The planned activities for year three include the following.
  - Maintenance of all servers comprising the cyberinfrastructure, including MFERD/ICME portals.
  - Repository of Material Properties: Transition to production mode, making it widely accessible to the researchers within the MFERD/ICME project, in particular making it the project-wide platform for the exchange of magnesium data and material models. Populate the database with experimental data, generated at MSST and through collaborators and data taken from literature. Enhance access control mechanisms (group and/or project based) to support protection of intellectual properties, thus making it possible to open the database to the general public in the future, perhaps in collaboration with TMS. Collect the user feedback and enhance the repository by supporting more data types and more types of material models, as requested by the user community and the project objectives.
  - Support for Design Optimizations: Collaborate with Task 4 to verify and validate FAME, collect the user feedback, and improve/enhance the GUI according to the user requests. Merge FAME with job submission and job monitoring services into a single system supporting the complete process of design optimizations starting with the design-of-experiment service. Through automated job submissions, generate the responses of the simulated system while using the adaptive environment for creating metamodel ensembles to the support of the actual design optimizations with user-friendly interfaces all while developing flexible resource management techniques to minimize the turnaround time for generation metamodels. In the later phases, the subsystem for design optimizations will be integrated with the subsystem for multiscale simulations.
  - Repository of computational modules: Create the prototype of a repository of computational modules needed for multiscale simulations including manufacturing processes, fatigue and design optimizations. The repository will allow exchange codes between the collaborators, and for authorized users, submit jobs

on the computational resources at MSST. The initial targets are: Vienna Ab-initio Simulation Package (VASP), Molecular Dynamics Simulator LAMMPS, Micro-3D, ABAQUS, and LS-DYNA.

- Gather community requirements for support for multiscale simulations, and design the cyberinfrastructure components to meet these requirements.

## **Introduction**

The objective of this cyberinfrastructure is the establishment of an engineering virtual organization (EVO) to exploit the recent transformative research in material science involving multiscale physics-based predictive modeling and multiscale experiments and design, in conjunction with robust design and manufacturing process optimizations with uncertainty and cyberinfrastructure development (Figure 1). The information, data, and software tools generated by the virtual organization will enable closing the significant knowledge gaps in a unifying physics-based modeling theme that captures a broad range of materials, admits structure-property relations, can be used in simulation-based design, can be implementable into finite-element codes, can be experimentally validated, can capture historical effects, and can morph into a metamodel for rapid use prognostics. The knowledge and data will come from many sources across organizational boundaries (distributed databases of geometries, material properties, manufacturing processes, experimental results coming from different labs, etc.), allowing experts from different disciplines (such as bio-inspired material models, models at different length scales, metamodeling, and optimizations) to work together toward a common goal.

### **The implementation will follow the Service-Oriented Architecture paradigm.**

More specifically, the creation of the cyberinfrastructure will result in the development of the “community of practice” portal that allows for the development and integration of multiscale physics-based materials models for selected properties and processes in the context of USAMP’s three-nation Magnesium Front-End Research and Development pilot project (MFERD), in particular task 1.9: Cyberinfrastructure for Integrated Computational Material Engineering (ICME).

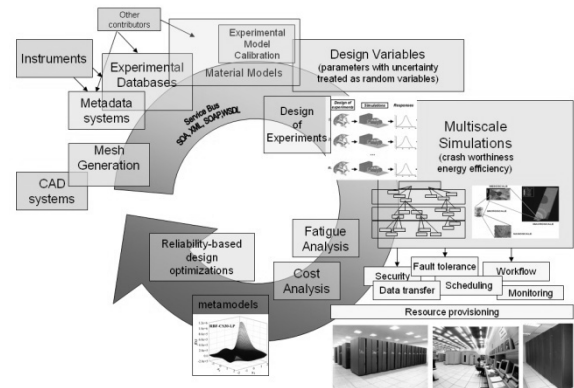


**Figure 1.** The vision of the cyberinfrastructure will integrate distributed databases of engineering knowledge and computational workflows for multi-objective, multiscale design optimizations under uncertainty.

The Portal manages the user credentials and user sessions and hosts portlets implementing rich GUIs for services rendered by the infrastructure (database queries, remote job submission, etc.). The GUI is being implemented using the combination of Java Applets, Java Script, and AJAX. In addition, the Portal will enable accessing the services from Grid-enabled standalone applications. For example, modules for MATLAB and ABAQUS are planned to allow these applications to access the material properties databases directly from the native GUI (MATLAB, ABAQUS, respectively) and submit jobs to remote high-performance platforms.

The portals delegate the actual processing of the user requests to services implemented in Java. The services will form a façade for the Grid fabric services, such as Globus grid resource allocation management (GRAM)—remote job submission, direct access interface system (DAIS)—remote database access, and gridFTP (file transfer and remote file system access). The overall architecture of the proposed Cyberinfrastructure for engineering Virtual Organization is shown in Figure 2.

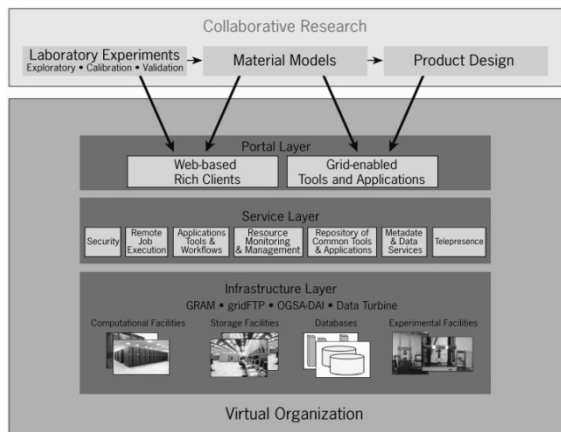


Figure 2. Architecture for MFERD/ICME portal.

Finally, the software integration is accomplished by applying the Java Business Integration (JBI) approach, using an open-source Service Bus implementation, as shown in Figure 3.

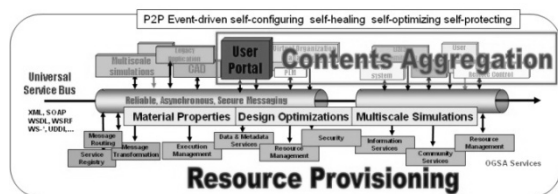


Figure 3. Horizontal software integration based on the service bus concept (as opposed to currently used centralized “hub and spoke” architectures) leading to vertical silos and stovepipes.

## Repository of Material Properties

### Introduction

The goal for this cyberinfrastructure component is threefold as shown in Figure 4. It serves as a repository for experimental data (stress-strain, strain-life, and microstructure images), a repository for material constants (for plasticity-damage models, the multistage fatigue models, and models of the material microstructure), and a suite of online tools for extracting the material constants from the experimental data (damage fit, multistage fatigue, and microstructure analyzer). The seamless integration of those otherwise disparate functionalities is achieved by implementing all back-end (“server-side”) support as web services and mashing them up using AJAX on the client-side (Web browser).

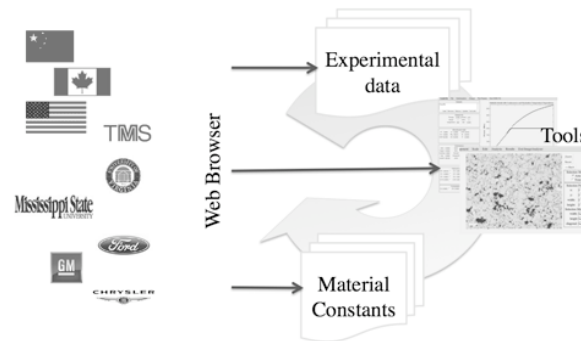


Figure 4. The concept of the Web-based Repository of Materials Properties.

## Design of the Repository

### Experimental Data

The system is designed to support the sharing of thousands of data sets of a small to moderate size (gigabytes). The large number of the data sets mandates a support for metadata describing these data sets thus allowing for queries. The manner of how the data is described, that is, the metadata schema, may vary for different types of experimental data and in addition, it may change in time, adapting to the evolving user needs. Therefore, it is necessary to introduce a very flexible metadata system without compromising the performance of queries. The data may be stored at different locations that support different mechanisms or interfaces for data access. Finally, strong authentication and group-based authorization mechanisms are required.

The metadata catalog and the storage are deliberately organized independently from each other. The storage is implemented as a flat collection of files and the physical location of a particular file is determined by the storage. The user can access it only by its logical name. The resolution from the logical name to the physical location is performed dynamically by an independent service—the replica locator. The metadata catalog is conceptually implemented as a single “business” structured query language (SQL) table. The columns of the table represent the attributes of the metadata, with the logical name of the file as one of the attributes. The user may query the catalog to retrieve a set of logical names of files that match the selection criteria constructed as Boolean expressions involving the

values of the metadata attributes—equivalent of SQL queries. In addition, the metadata system supports capturing the parent-child relationships between the metadata entries, adding to the flexibility creating different views on the catalog, and consequently, allowing the user to customize the interfaces for the data selection.

The data stored in the repository are meant to be consumed by the user applications (as input files). It is a well known fact that hardly ever any two applications accept the data in the same format. It is thus imperative that the repository provides support for data transformations. The transformation can be simple, such as format translations (e.g., the parameters of a stress-strain curve needs to be formatted differently for ABAQUS and LS-DYNA finite analysis simulations) or may involve more complex processing, such as performing model fits.

The repository of experimental data is thus implemented as an aggregate of independent services: metadata service, replica locator, data storage and authorization service, and transformation services, all integrated using Apache's ServiceMix—an Open Source implementation of an enterprise service bus (ESB) compliant to the Java Business Integration (JBI) specification. A more detailed description of the repository of the experimental data has been given in the last year annual report.

### **Material Constants**

The material constants are stored as metadata records without associated data files. The same metadata service is used for managing the constants (without orchestration with the replica locator and storage services).

### **Integration of the Repository of Experimental Data and the Repository of Material Constants**

The integration is achieved by the association of the experimental data entries in the metadata catalog and, independently, material constants entries in the catalog with particular material. To make the navigation of the metadata catalog easier for the end user, the materials (typically understood as a particular alloy) are grouped into

“material classes” representing the dominant component of the alloy. For example, the class “Magnesium” represents all alloys of magnesium. As shown in Figure 5, to find all experimental data pertaining to material hy130steel, the metadata catalog is queried to find all metadata records corresponding to experimental data with material name “hy130steel.”

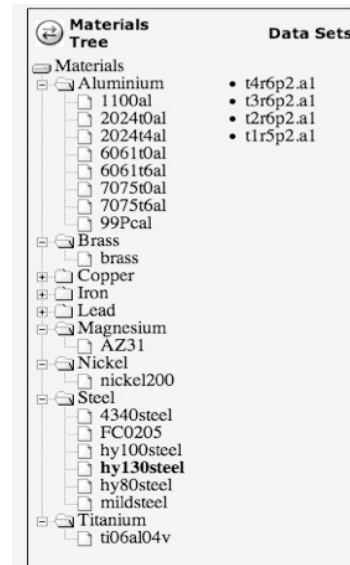


**Figure 5.** A screenshot of the user interface for browsing the contents of the repository.

To narrow the search, the query may be limited to data sets corresponding to a particular data type, such as stress-strain, or by specifying the values of a set of metadata attributes to be matched. Note the GUI of the repository automates the process of generating queries; the user navigates the tree of materials as if the repository was just a hierarchy of folders and files on the local disk, accessible through familiar File Explorer (Microsoft's Windows) or Finder (Mac) interfaces. The result of the query—the list of the available data sets—is displayed under the “data set” header (Figure 5). By selecting a particular element in the list, the user may display the metadata record (Figure 6), see the data displayed as a plot (Figure 7), or invoke a tool (damage fit for stress-strain data). Note that in order to display the plot, the replica locator needs to be queried to localize the data set, the data must be retrieved from the storage, the stress-strain curve must be calculated from the raw data, and a plot must be generated and sent to the

browser. All this happens automatically as a result of pressing the “Plot” button.

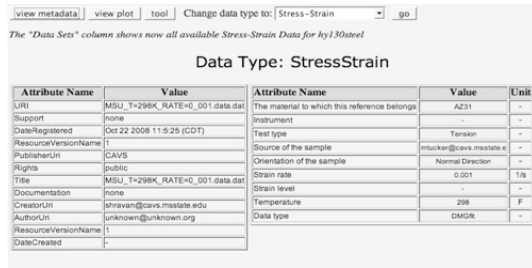


Figure 6. A screenshot of the user interface displaying the metadata record for a selected experimental data set.

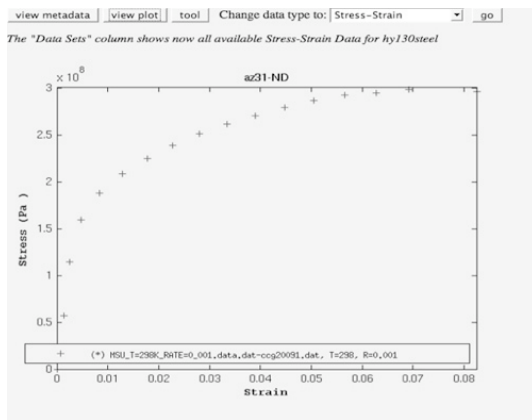


Figure 7. A screenshot of the user interface displaying a stress-strain curve computed from the selected data set.

To get material constants for a given material, a similar catalog query needs to be executed: “find all metadata records representing material constants with material name ‘hy130steel’.”

### Online Tools

The tools are implemented as MATLAB modules running on the server side, invoked via a job submission service.

The job submission service, as any other WSDL service, is stateless and designed to support running jobs in batch mode, which is in clear conflict with statefull and inherently interactive MATLAB applications. This problem has been solved by re-engineering the MATLAB code for a tool into a series of short, stateless batch operations executed as the result of the user clicking on GUI widgets and delegating the responsibility of maintaining the MATLAB

session to the Portal middleware (the session object). This solution not only creates an illusion of interactivity for the end user, but also allows for several independent users using the MATLAB of the same tool. Figures 8, 9 and 10 are screenshots to demonstrate the available tool.

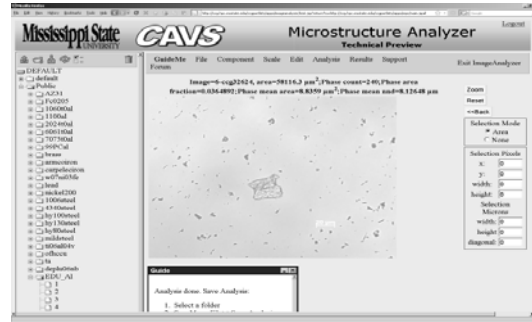


Figure 8. A screenshot of the user interface for the tool to extract microstructure information from a high-resolution image of a material sample.

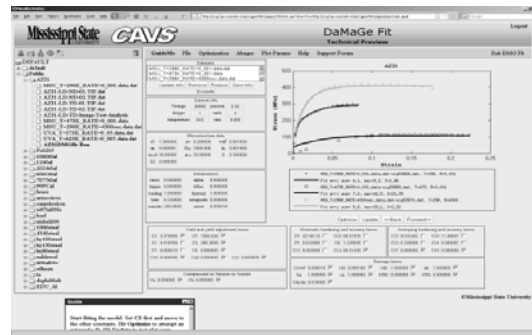


Figure 9. A screenshot of the user interface for the damage model calibration tool.

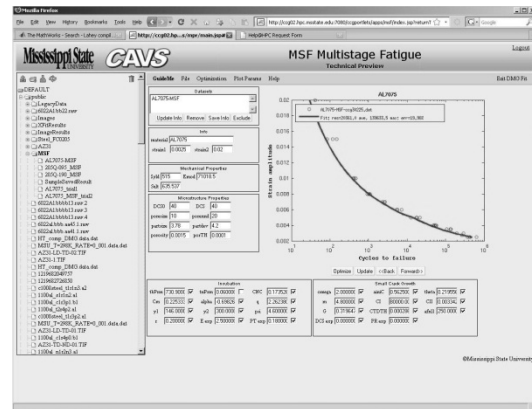


Figure 10. A screenshot of the user interface for the multistage fatigue model calibration tool.

## **Data Service Façade**

Construction of the repository from the independent services has many advantages. On the other hand, it is difficult for the end user (or the user agent) to use such a distributed system. Many conceptually simple operations, such as retrieving a file, require making multiple requests to different services. The above mentioned flexibility of the system adds to the complexity of using the repository: the user must not only know the right order of service invocations, but also needs to know interfaces of the particular services and the communication protocols used by these services. Furthermore, since all services act independently from each other, maintaining repository consistency becomes difficult (e.g., each metadata record corresponds to at least one data resource and each data resource has associated metadata records).

To ease these difficulties, all constituent services of the repository are hidden from the user behind a façade, which is the middle-tier service that orchestrates the services and exposes a simple, intuitive interface for the end user. Now, given the Uniform Resource Identifier (URI) of the resource (from querying the metadata service or otherwise), there is a single method of the façade to retrieve the file. The invocation of this method results in all actions needed to get the authorization assertions, resolving URI to the physical locations and returning the data stream. To achieve that, the façade employs the business delegate pattern that delegates the actual implementations of the back-end service clients to service providers, which understands the transport and assertion requirements of the corresponding services. In addition, the provider-based architecture makes it easy to retarget the repository to a different implementation of any of the constituent services; it requires just replacing the service provider without the need for modifications of the façade interface. The business logic of the façade also enforces the integrity of the repository. For example, a request to remove a data resource from the storage automatically triggers appropriate actions of replica locator and metadata services initiated by the façade.

## **Data Transformations**

Hardly ever have any two applications accepted the data in the same format. It is thus imperative that the repository provides support for different data transformations. There are two basic types of data transformations. One type facilitates relatively simple operations, such as format translations or processing data headers that can be performed on-the-fly. The other type supports the processing of large files or making complex transformations. These transformations are delegated to high-performance platforms. The data transformations are independent from the metadata catalog, or file repository services, and need to be implemented as independent services (the loose coupling principle) and invoked either prior to the data uploading or after retrieving the data from the file repository, but before returning the data to the end user.

Several data transformations have been developed. Among the purposes of the material properties repository is the collection of data coming from the measurement of stress-strain curves. The data coming from different instruments are, very expectably, in different formats. A transformation service hides these differences from the instrument operator who uploads the data to the repository. The service creates a metadata record by combining the information from the header automatically generated by the instrument from the system (e.g., time and the operator identifier), and the data typed in by the operator (the instrument has no way to know what material and in what manufacturing stage, e.g., after rolling or stamping), and then from the measured values of the displacements and loads, calculates the true stress and strain values. Once this “transformation” is complete, the metadata and data pair are uploaded to the repository. When retrieving the data from the repository, the user may specify the desired format (e.g., raw data, data formatted to match the syntax of the ABAQUS FEA package, or others). Such format translation is delegated to another transformation service, which is invoked automatically after retrieving the data from the repository and before sending the data to the user.

**Integration of Data Repository Services Using the Enterprise Service Bus**

The primary functionality of the service bus is to route messages between services associated with it. There are two base types of associations. The service can be plugged into the bus container as a so-called service engine to be directly invoked through a Java message service (JMS).

Alternatively, a service may be deployed in a separate container and be invoked through a web service interface (WSDL). The web service invocation is facilitated by a binding service bus component.

The incoming requests, generated by a web portal or a standalone client, are accepted by a custom developed hypertext transfer protocol (HTTP) input component. The input components effectively act as service brokers, forwarding the requests to the target services that generate the actual responses to the client requests. To make it possible, the client’s request must provide a signature of the target service. In order to invoke the service (i.e., to forward the request), the signature must be resolved into the service endpoint reference (EPR). To this end, the broker uses a service directory—another custom service engine. The service signature is a collection of the service attributes. In the simplest case, it could be just the service name. The service WSDL interface could serve as the service signature; however, for this data repository, most of the transformation services implement the same WSDL interface making it easy to “bind” the actual transformation late, depending on the context of the request. The EPR may refer to an “atomic” service (either a service engine or a binding component) or refer to an orchestrating service (e.g., a Business Process Execution Language (BPEL) engine, or a service façade) that aggregates several services in order to generate the final response the client requested.

**Architecture of the Repository**

The architecture of the repository is shown in Figure 11. The clients, implemented in asynchronous JavaScript, communicate with the service bus through the ubiquitous Hypertext Transfer Protocol (HTTP). The Input Component/Service Broker accepts three types of requests: metadata query, data upload (that may or

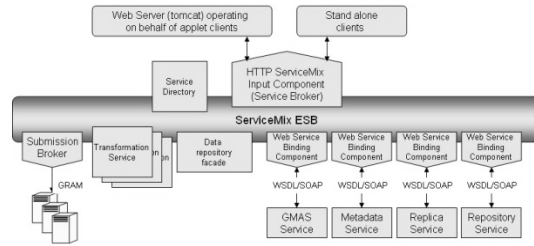


**Figure 11.** Architecture of the data repository integrated by an enterprise service bus (ESB).

may not involve the data transformations), and data download (that may or may not involve the data transformations). The metadata query allows the user to search the metadata catalog to locate the data set of interest, create custom views on the data repository, as well as uploading and downloading of data. Consequently, the client requests to perform these operations are simply forwarded by the service broker to the façade service engine. The data façade invokes the constituent service services as needed through the binding components.

The data transformations, on the other hand, are dynamically bound. If the repository operation requires a transformation, the name of the transformation is passed as the request argument. The broker resolves the transformation name into the service EPR using the service directory and invokes the service before or after invoking the data façade services, depending whether data are uploaded to or downloaded from the repository, respectively. Simple transformations are implemented as ESB service engines, while complex transformations are executed by the submission broker—a binding ESB component. The submission broker is responsible for setting the runtime environment (setting the environmental variable, creating a working directory, etc.), staging in data, executing and monitoring jobs on remote systems and finally passing the results to the requested destination (typically through a third-party data transfer). Since all transformations implement the same WSDL interface (the transformation specific parameters are grouped as a single array of strings), the dynamic binding allows seamless adding or replacing existing transformations.



## FAME: Flexible Advanced Metamodeling Estimator

### Simulation-Based Design Optimizations

Simulation-based design optimization is playing an increasingly important role in engineering product development. It enables engineers to make optimal product design and manufacturing process decisions, reduce or eliminate the need for physical prototyping, and increase the quality of manufactured products. This importance is also evident in the development and marketing of several commercial optimization software tools (e.g., Vanderplaats R&D, Inc.'s Design Optimization Tool, Dassault Systemes' iSIGHT) that can be interfaced with computer-aided design (CAD) or computer-aided engineering (CAE) and engineering simulation programs to accommodate a paperless product design activity.

The rapid development of computer technology and commercial simulation tools has enabled engineers to solve more complex problems and obtain more details to enhance knowledge. For example, it is now possible to perform full-scale, finite-element (FE) simulations of vehicle crashes with commercial FE codes and parallel computers. However, the increased complexity has significantly increased the computational cost that in turn prevents engineers from combining the simulation tool with an optimization method, which is an iterative procedure and requires hundreds or even thousands of simulations to perform one design. To alleviate the high computational cost of full-scale simulations, yet maintain the level of complexity, the metamodeling approach has been widely adopted in simulation-based design optimization.

In the metamodeling approach, the expensive simulation tool is replaced with a surrogate approximation model (metamodel) that is in explicit form and efficient to evaluate. The metamodel is created from the results of some predefined simulations determined by Design of Experiments (DoE) methods. Figure 12 illustrates the procedure of simulation-based design optimization using DoE and metamodeling. There are four major components in this procedure: DoE, simulation, metamodeling, and optimization, which serve as four independent functional blocks.

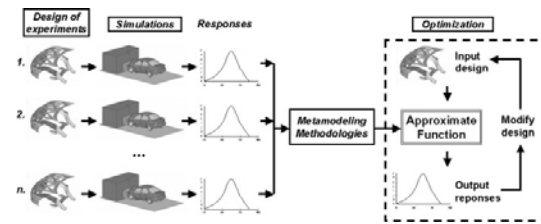


**Figure 12.** Workflow for simulation-based optimization using DoE and metamodeling.

Since a limited number of simulations are used in creating the metamodel, the model accuracy will depend on how well the selected designs represent the design space. To this end, the DoE methods such as factorial design, central composite design, Taguchi orthogonal array, and Latin hypercube sampling are typically used to create the samples and referred to as the response surface methodology (RSM). For high-order nonlinear responses, other metamodeling methods using high-order nonlinear functions, particularly the RBFs, work best.

With the created metamodels representing responses within the design space, the optimization can be carried out using existing optimization methods such as gradient-based or direct search algorithms. As pointed out by the no-free-lunch theory, there is no single optimization method that is good for all types of problems. Therefore, it is preferred to apply different optimization methods at this stage to obtain the best solution.

### FAME Design

The purpose of FAME is to provide the environment for the creation of metamodels given a set of input (design) points and the corresponding system responses. The flexibility refers to the capability of FAME to generate many different metamodels by selecting different metamodeling techniques and adjusting their parameters. Once created, the metamodel can be quickly verified by computing the residuals between the metamodel predictions and the actual responses obtained by a measurement and/or by a direct numerical simulation. Advanced refers to the capability of FAME to combine several metamodels into a metamodel ensemble, by applying different ensemble techniques (from

simple average to methods weighting the contributions from constituent metamodelling, based on the accuracy of their predictions). The metamodelling (and metamodelling ensembles) are persistent [i.e., they can be accessed (be modified or used to generate predictions)] across the user sessions and shared between users.

This functionality has been achieved by orchestrating several loose-coupled web services, as illustrated in Figure 13. The metamodelling service provides a uniform interface for creating, customizing, evaluating, and getting predictions of metamodelling, given the values of the input variables and the system responses (typically two sets: one for the metamodelling creation and the other for the metamodelling validation). The ensemble service provides a uniform interface for creating, customizing, evaluating, and getting predictions of ensembles, given a vector of existing metamodelling together with a set of test points (the value of the input variables and the corresponding responses).

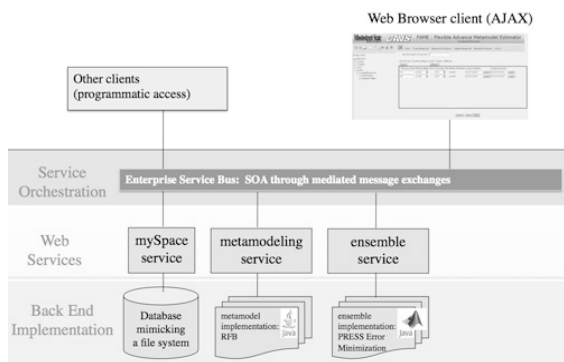


Figure 13. The architecture of FAME.

The design based on uniform interfaces guarantees extensibility of FAME. Each metamodelling (or ensemble) technique is an independent software component (a Java class), implementing a common (i.e., uniform) service interface. This allows the adding of new metamodelling techniques at a later time, without the need of modifying the existing components. The uniform interface provide methods for the metamodelling (or ensemble) creation, validation, and getting predictions, as well as methods for querying the service about the parameters needed by a particular implementation of the interface. The FAME GUI implementation extensively uses the queries in order to dynamically create the user

interface custom tailored for a particular metamodelling (or ensemble) technique to be used (cf Figure 14).

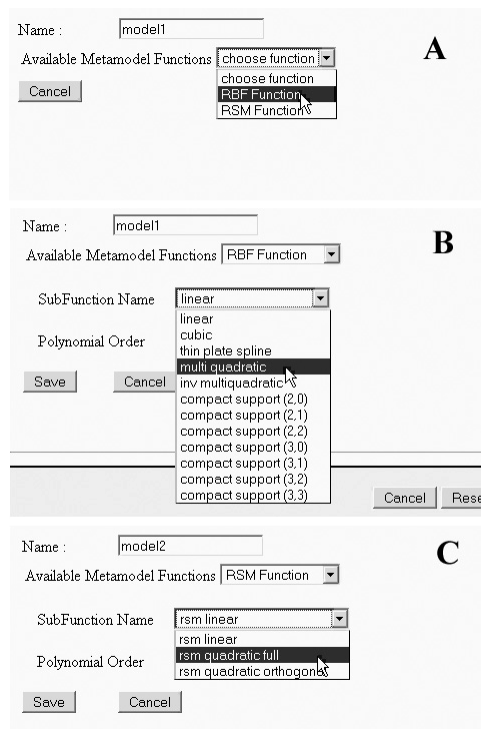
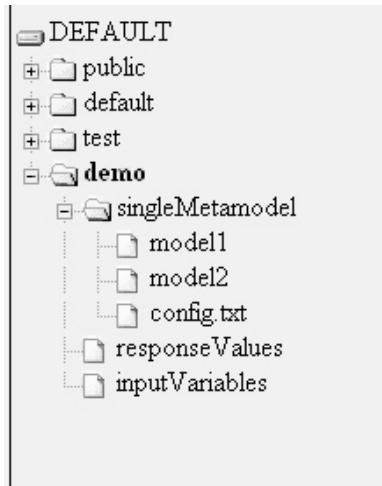


Figure 14. A composite of three screenshots of a fragment of FAME user interface. Depending on the selection of the metamodel type (A), the GUI displays a custom form for providing metamodel parameters (B or C).

The metamodelling and ensemble services operate on data (values of input variables and responses) provided by the user. Therefore, it was necessary to develop a support for uploading and maintaining the data on the server side. This has been accomplished by developing MySpace service. MySpace reuses the services used for the repository of experimental data with metadata record, comprising the name of the data set, the name of the user who uploaded it and the date and time of the upload. The GUI for the MySpace service is similar to Microsoft’s File Explorer and Mac’s Finder (cf Figure 15). MySpace is used not only to store and manage user-provided data set; the results of FAME—metamodelling, ensembles, and results of validation are stored there as well.



**Figure 15.** A screenshot of MySpace user interface.

### **Presentations/Publications/Patents**

1. T. Haupt and M. Horstemeyer, "Cyberinfrastructure for Design Optimizations," 2008 TMS Annual Meeting, New Orleans, LA, March 9–13, 2008
2. T. Haupt, "Cyberinfrastructure for multiscale Simulations," 2007 TMS Annual Meeting, Orlando, FL, Feb 25–March 1, 2007.
3. T. Haupt, A. Voruganti, A. Kalyanasundaram, and I Zhuk. "Grid-Based System for Product Design Optimization," *2nd IEEE International Conference on e-Science and Grid Computing*, Amsterdam, the Netherlands, Dec 4–6, 2006.
4. T. Haupt, A. Kalyanasundaram, and I. Zhuk "Architecture for a Secure Distributed Repository," *7th IEEE/ACM International Conference on Grid Computing*, Barcelona, Spain, Sept 27–28, 2006: IEEE/ACM Press, 170–177.
5. T. Haupt, A. Kalyanasundaram, G. Singh, and I. Zhuk, "Data Repository for Ad-Hoc Collaborations Horizontally Integrated with Transformation Services," *The 2007 International Conference on Grid Computing and Applications*, Las Vegas, NV, June 25–28, 2007.

## L. Simulation-Based Design Optimization

*Principal Investigator: Masoud Rais-Rohani*

*Professor, Aerospace Engineering*

*Mississippi State University*

*318c Walker Bldg.*

*Mississippi State, MS 39762*

*(662) 325-7294; fax: (662) 325-7730; e-mail: masoud@ae.msstate.edu*

*Co-Principal Investigator: Chris Eaman*

*Assistant Professor, Civil Engineering*

*Mississippi State University,*

*235F Walker Bldg.*

*Mississippi State, MS 39762*

*(662) 325-9839; fax: (662) 325-7189; e-mail: eaman@enr.msstate.edu*

*Technology Area Development Manager: Joseph A. Carpenter*

*(202) 586-1022; fax: (202) 586-1600; e-mail: joseph.carpenter@ee.doe.gov*

*Field Project Officer: Aaron D. Yocum*

*(304) 285-4852; fax: (304) 285-4403; e-mail: aaron.yocum@netl.doe.gov*

*Contractor: Mississippi State University*

*Contract No.: 4000054701*

### Objective

- Develop computational design technologies (methods and tools) that can be used for the analysis and optimization of automotive structural design concepts made of lightweight materials. The selected research topics are directed towards the principal attributes, lightweighting and safety, in presence of design uncertainties and are investigated while pursuing the following objectives.
  - Development of novel approaches for deterministic and probabilistic (reliability-based) design optimization of automotive structures.
  - Investigation of various metamodeling and mechanics-based analytical techniques as viable surrogates for expensive, high-fidelity finite-element simulations.
  - Development of mathematical models for efficient uncertainty quantification and structural reliability analysis.
  - Integration of advanced constitutive models in simulation-based design optimization of automotive structures.
  - Application of the developed methods and tools in design optimization of example problems involving automotive structural components, subsystems, and systems.

### Approach

- The activities in this task are separated into the following areas: (1) design optimization, (2) structural mechanics, (3) surrogate modeling, (4) uncertainty quantification, and (5) structural reliability. The research scope and plan of action in each area are outlined as follows.
  - Investigate different approaches for reliability-based design optimization (RBDO) of automotive structural components. Develop RBDO formulations and solution techniques consistent with the complexity of vehicle structures. Investigate novel approaches for topology optimization of continuum structures and multilevel optimization of hierarchical systems, with deterministic and reliability-based design constraints.

- Since crashworthiness is a major requirement in design of automotive structures, investigate the mechanics of progressive collapse in dynamically-loaded thin-walled structures to explore opportunities for design of lightweight and energy-absorbent components. Perform nonlinear static and nonlinear transient dynamic finite-element simulations of vehicle components and systems made of different lightweight materials. Compare the response predictions with traditional plasticity and the internal state variable (ISV)-based constitutive models.
- Evaluate the performance of modern metamodeling techniques as low-cost surrogates for high-fidelity response simulations. Study the accuracy and efficiency of stand-alone and ensemble of metamodels for estimation of nonlinear response functions. Investigate the accuracy and efficiency of mechanics-based analytical models for estimation of structural responses, such as energy absorption under impact loading.
- Investigate the accuracy and efficiency of the different techniques used for the quantification of random uncertainties and their propagation in the design optimization process.
- Develop new approaches to increase the efficiency and accuracy of failure probability/safety index estimations for the evaluation of component, as well as system reliability.
- Apply the techniques developed or examined in the different research areas to simulation-based design optimization of automotive structural problems ranging from a single component to a multi-component system.

### **Accomplishments**

- Developed a new stochastic method for topology optimization of continuum structures and compared its performance with some other stochastic, as well as gradient-based, techniques reported in the literature.
- Investigated the application of alternative approaches for multilevel optimization of hierarchical (product-material) systems under uncertainty.
- Performed nonlinear transient dynamic finite-element simulations to investigate the progressive collapse and energy-absorption characteristics of extruded multi-cell tubes as design concepts for automobile side rail. Also developed a mechanics-based analytical model for estimation of mean crush force of multi-cell tubes.
- Developed an analytical technique for uncertainty quantification and investigated its use in uncertainty analysis of damage based on an internal state variable constitutive model.
- Developed a simulation-based technique for component and system reliability analysis and compared its performance with several analytical and simulation-based techniques reported in the literature.
- Collaborated with cost-share partners, Alpha STAR Corporation and Wade Services, on topics related to finite-element modeling and simulation of joint concepts for composite structures and optimum designs for trailer components.
- Wrote several conference papers and journal publications as listed at the end of this chapter. However, the journal manuscripts that are still under review are not included.

### **Future Direction**

- Investigate the energy-absorption characteristics of crush tubes made of fiber-reinforced polymer composite materials.
- Investigate multilevel optimization of integrated material-product / process-product systems, using multiscale material models.
- Conduct an optimization study, using full-vehicle simulations with ISV-based material models under multiple design criteria, such as damage and fatigue.

---

### **Introduction**

This report provides a summary of major activities conducted in the second year of the Department of

Energy's Southern Regional Center for Lightweight Innovative Design project as part of the simulation-based design optimization task. The areas of emphasis include topology optimization,

energy absorption under impact loads, uncertainty quantification, and structural reliability. In each of the following sections, a major focus area is briefly discussed with highlights of pertinent results.

Other activities not reported here include the application of multilevel optimization techniques to hierarchical systems with deterministic and reliability-based design constraints. Also, as a result of collaboration with two cost-share providers, Alpha STAR Corporation and Wade Services, members of this task had the opportunity to apply some of the developed techniques to an industrial problem and to explore the capabilities of the progressive failure analysis software GENOA for the analysis of structural design concepts made of advanced composite materials.

### **Topology Optimization Using Element Exchange Method**

Topology optimization of continuum structures is aimed at finding the optimum distribution of a specified volume fraction of material in a selected design domain that would result in the minimization of structural compliance or strain energy and provide an optimal load path between the loading points and the structural supports.

Topology optimization is often used as a first step in identifying the general layout of the material in a specific domain before performing sizing and/or shape optimization to find the optimal geometry.

Previous efforts in topology optimization have, for the most part, been based on the gradient-based solid isotropic material with penalization (SIMP) method (Bendsoe 1989, Zhou and Rozvany 1991). SIMP is computationally efficient and easy to integrate with most general-purpose FEA codes. However, SIMP-based solutions show mesh-dependency and the clarification of final topology requires the use of one of several filtering techniques.

Besides the gradient-based methods, several stochastic methods have also been developed for topology optimization. Two notable approaches are the particle swarm optimization (PSO) (Fourie and Groenwold 2001) and enhanced genetic algorithms (GAs) (Wang et al. 2006). Although

these methods may not require any filtering of the optimum layout, they tend to be very computationally expensive.

As part of this project, we developed a new stochastic approach called the Element Exchange Method (EEM) for compliance minimization. Named after the principal operation in the topology optimization strategy, EEM solution procedure is simple to implement and easy to integrate with any existing FEA code.

In this section of the report, we provide a brief description of the EEM algorithm and compare the performance of this method with some others using two- and three-dimensional example problems.

The EEM algorithm starts with a random distribution of a specified number of solid isotropic elements consistent with the desired volume fraction,  $V_o$ , in the design domain. While the solid elements are given a nondimensional density of 1.0, the void elements have a small nondimensional density (0.001). Similarly, the Young's modulus of void elements is taken as 0.001 times that of the solid elements. The non-zero properties for the void elements are meant to prevent numerical ill conditioning of the stiffness matrix in FEA.

With the initial topology identified, a static FEA is performed to find the strain energy distribution among the solid and void elements, as well as the strain energy of the structure as a whole. Based on the selected value for the number of exchange elements,  $N_{EE}$ , the algorithm performs a so-called *element exchange* operation. The  $N_{EE}$  solid elements with the lowest strain energy amongst the solid elements are converted into void elements (density and Young's modulus set to respective minimum values), while a volumetrically-equivalent number of void elements with the highest strain energy amongst the void elements are converted into solid elements (density and Young's modulus set to respective maximum values), such that the volume fraction remains fixed. This step is followed up by another static FEA and the exchange operation procedure is continued until convergence is reached.

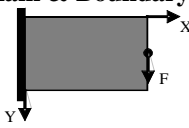



Although the EEM algorithm pushes the topology towards minimum-compliance, the basic element exchange operation alone may not prevent the development of undesirable checkerboard patterns or the possibility of back-and-forth oscillation in a subset of elements from solid to void, back to solid in repeated iterations.

However, with the help of additional operations introduced as part of EEM algorithm, these two problems are eliminated. One such operation identifies and eliminates the checkerboard regions in the topology, whereas another involves a random redistribution or shuffling of a limited number of solid elements after the completion of a set number of exchange iterations. This move is similar to a mutation operation in GAs and craziness in PSO, and is found to improve the final topology by eliminating the possibility of entrapment at a locally optimum design point. Additional details about EEM can be found in Rouhi and Rais-Rohani (2008).

**Two-Dimensional Example Problems**

The cantilevered beam model and corresponding optimum topology results are shown in Table 1.

**Table 1.** Comparison of EEM and enhanced GAs

Design domain & Boundary conditions			
			
$n_x, n_y, V_0$	24, 12, 0.5		48, 24, 0.5
Method	EEM	Enhanced GA <sup>a</sup>	EEM
SE	66.1	64.4	63.5
N	150	4x10 <sup>4</sup>	250
Topology			

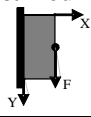




<sup>a</sup>Wang et al. (2006).

Each design domain is defined according to  $n_x, n_y$ , and  $V_0$  values, representing the number of finite elements in the horizontal and vertical directions and the required volume fraction, respectively. The final value for the nondimensional strain energy (SE), total number of iterations (N) and the resulting topology are also shown in Table 1. Two

different mesh densities are considered for EEM, resulting in slightly different topologies. The results reported by Wang et al. (2006) based on the enhanced GA approach are also shown in Table 1 for comparison. Although the final geometry and strain-energy values are nearly the same, the EEM solution converges much faster.

With the beam dimensions modified, the EEM solutions are compared with those based on PSO in Table 2. As in the previous model, the EEM approach converges much faster with no loss of accuracy.

**Table 2.** Comparison of EEM and PSO

Design domain & Boundary conditions				
				
$n_x, n_y, V_0$	20, 47, 0.5		40, 94, 0.5	
Method	EEM	PSO <sup>*</sup>	EEM	PSO <sup>a</sup>
SE	2.96	Not reported	5.1	Not reported
N	100	10 <sup>5</sup>	103	10 <sup>3</sup>
Topology				
		Continuous Density		Binary Density

<sup>a</sup>Fourie and Groenwold (2001).

**Three-Dimensional Example Problems**

A cubic domain shown in Figure 1(a) is simply supported at its four bottom corners and is loaded by four concentrated vertical forces at the top surface. Using the EEM procedure with  $n_x, n_y, n_z, V_0 = 20, 20, 20, 0.08$ , the optimum topology in Figure 1(b) is obtained after 178 iterations. For comparison, the results obtained by Olhoff et al. (1998) using the optimum microstructure (OM) method is shown in Figure 1(c). The grey regions in Figure 1(c) imply intermediate density, since the OM method is gradient-based. Also, elements with density less than the threshold value are filtered out to arrive at the final topology.

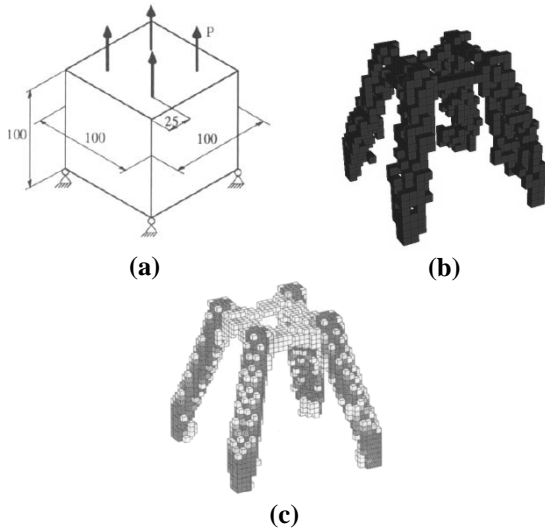


**Figure 1.** (a) Design domain and boundary conditions, (b) EEM, and (c) Optimum microstructures.

Therefore, the final topology of OM may not match the pre-specified volume fraction.

The geometry shown in Figure 2(a) is a generic model of an automobile control arm. While the triangular region in the middle can be altered through topology optimization, the three-corner regions (knuckles) are held fixed with the specified boundary conditions. The EEM solution based on  $n_x, n_y, n_z, V_0 = 26, 40, 12, 0.1$  is shown in Figure 2(b). Since the design domain is symmetric, only the upper half of the final topology is considered and shown for clarity. The optimization result in Figure 2(c) is obtained using commercial software Optistruct,\* where elements with density less than 0.15 are removed and the resulting geometry is post-processed to obtain a smoother shape.

The conclusions that can be drawn from this work are that unlike the gradient-based methods, EEM requires no filtering of the final topology and the resulting solid-void solution satisfies the imposed volume fraction. Also, the checkerboard control and the random shuffle algorithms help increase the solution fidelity and accuracy. Although EEM is not as efficient as the SIMP method, it is found

to be significantly more efficient than the stochastic methods found in the literature.

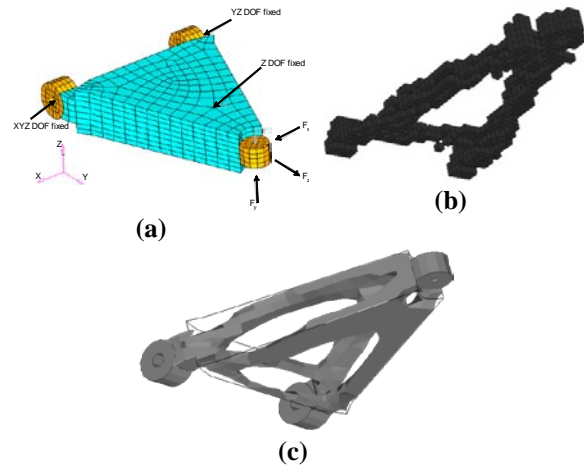


**Figure 2.** (a) Design domain and boundary conditions, (b) EEM, and (c) Optistruct.

### Energy Absorption Assessment of Axially Loaded Multi-Cell Tubes

There is a growing interest in the use of lightweight materials (e.g., magnesium alloys) combined with the extrusion process for the future production of automotive components, such as the side rails. One desirable feature of the extrusion process is that it accommodates the fabrication of multi-cell tubes with varying degrees of geometric complexity, as dictated by the design requirements.

Besides the material properties, the cross-sectional geometry (shape and size) of the side rails has a significant influence on its collapse mechanism and energy-absorption capacity in frontal collisions. Hence, the ability to evaluate multiple rail design concepts in an efficient manner can help improve the overall design process of automotive structures.

As part of our research in simulation-based design optimization, we investigated the mechanics of progressive collapse in thin-walled, angular, multi-cell tubes using the nonlinear transient dynamic FE simulations and studied the influence of cross-sectional geometry on the energy absorption of such tubes made of ductile materials.

We performed a series of FE simulations to evaluate the force-displacement response, specific

\* <http://www.kxcad.net/Altair/HyperWorks/ostutorials/ostut.htm#os2010.htm>



energy absorption (SEA), crush pattern and crush distance for different multi-cell, multi-corner models. As part of this work, we also investigated the merits of adaptive meshing, the effect of using different shell-element formulation, the effect of friction at the barrier contact surface, the role of trigger mechanism and initial imperfection on crush response and the used hourglass energy as means of verifying the accuracy of the simulation results.

The multi-cell models investigated are shown in Figure 3(a). The principal feature of these models is that they consist of two square tubes that are connected together in four different forms: corner-to-corner (A), web-to-corner (B), corner-to-web (C) and web-to-web (D). Although the different forms of connection do not drastically change the weight of the tube, it can alter the collapse response under dynamic axial loading.

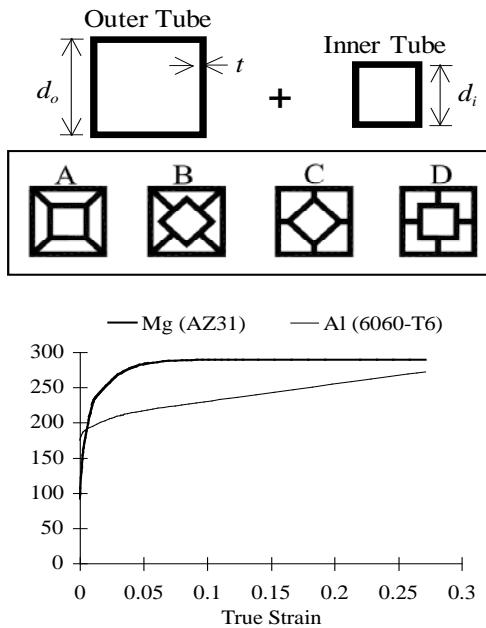


**Figure 3.** (a) Alternative cross-sectional models and (b) Tensile stress-strain curves of aluminum and magnesium alloys.

We developed an FE shell model for each tube in Figure 3(a) and used them for crush simulations using LS-DYNA. All tubes are 400 mm in length with  $(d_o, d_i, t) = (80, 40, 2)$  mm. The tube is treated as a clamped-free column that is impacted on its free end by a rigid block of 300-kg mass traveling

at a speed of 15.6 m/s (35 mph). The material model used for preliminary investigations is AA6060-T6 with  $E = 70$  GPa,  $\nu = 0.3$ , and  $\rho = 2.7e-6$  kg/mm<sup>3</sup>, and the true stress-strain curve as shown in Figure 3(b).

Figure 4 shows the simulated collapse of the four aluminum tube models at various time increments up to 30 ms. All FE models are based on Hughes-Liu shell elements and have an indentation trigger mechanism placed on two opposite walls of the outer tube near the impacted end.

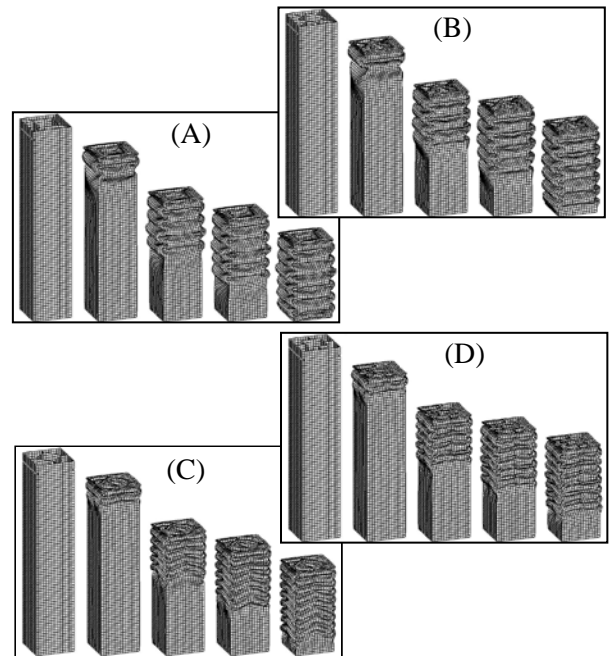


**Figure 4.** Collapse behavior of multi-cell tubes.

All models show a fairly symmetric progressive collapse with repeated folding deformation that extends to nearly 75% of the length in model D and the entire length in model A. Clearly, model A demonstrates less resistance to axial deformation as compared to model D, indicating the difference between corner-to-corner and web-to-web connections. Also, models B and C appear to have nearly the same crush distance, although the folding geometries are distinctly different. While the trigger mechanism reduces the maximum peak force shortly after impact, it helps to stabilize the crush deformation.

The plots of the crush force versus crush distance are shown in Figure 5.

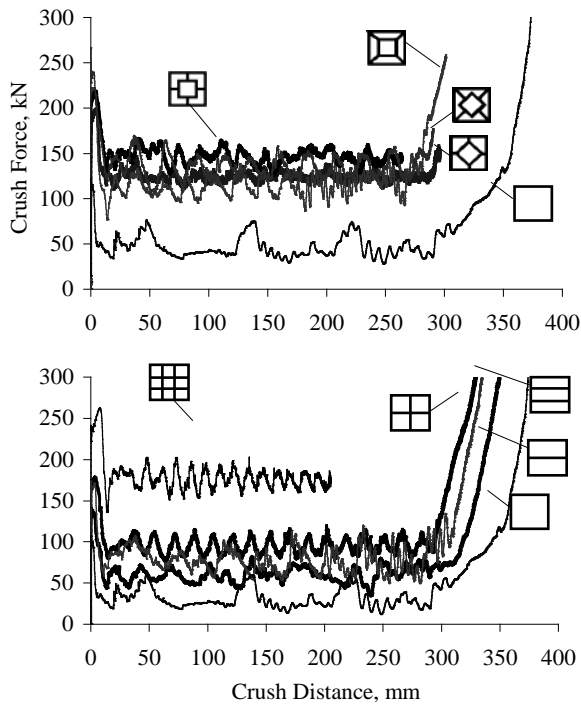


**Figure 5.** Crush force versus crush distance for different cross-sectional shapes.

Besides the models introduced earlier, other configurations (with uniform cell geometry), as reported in the literature, are also shown for comparison. Using the cell divisions in the horizontal and vertical directions as the distinguishing feature, these models are labeled as  $2 \times 1$ ,  $3 \times 1$ ,  $2 \times 2$ , and  $3 \times 3$ . The response of a single-cell square tube is also shown in Figure 5 for reference purposes.

The larger oscillatory pattern in each curve is due to the changes in tube stiffness as a result of repeated formation and closure of folds in the tube walls (see Figure 4). The maximum peak load varies from a low of 107 kN for the single-cell tube, to a high of 263 kN for the  $3 \times 3$  model. For models A through D, the average maximum peak value is approximately 215 kN. The rapid rise at the end of some curves indicates complete collapse that results in solidification (end of plastic deformation) in the tube.

The bar chart in Figure 6 compares the impact energy absorption as a measure of efficiency of

the tube models considered. SEA is the ratio of internal energy to mass. The energy values used for the calculation of SEA in Figure 6 correspond to the point where solidification begins. The models with the minimum and maximum SEA values are the square tube and the multi-cell model C, respectively. With an average SEA of 28.2 kJ/kg, models A through D appear to absorb more energy than the other four multi-cell shapes with an average SEA of 25.8 kJ/kg. The mass of each tube in units of kg is shown parenthetically in Figure 6.

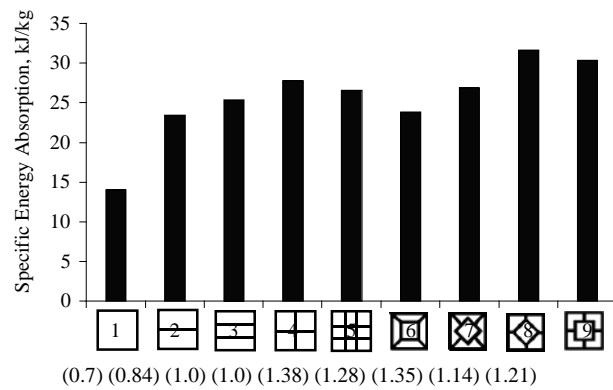


**Figure 6.** Specific energy absorption and mass (kg) for different cross-sectional shapes.

Crushing deformation of ductile thin-walled, multi-corner tubes under quasi-static and dynamic axial loads is principally governed by the collapse mechanism of the corner sections. In their study of rectangular tubes, Wierzbicki and Abramovicz (1983) pointed out that the generalized folding collapse of the corner sections involves four separate mechanisms described as rigid-body translation and rotation along with inextensional, quasi-inextensional, and extensional deformation. Although a large portion of the material undergoes rigid-body translation and rotation due to propagating hinge lines, it is the smaller region of toroidal and conical surfaces that is responsible for plastic deformation and energy absorption.

Figure 7 shows the predicted mean crush force for the four multi-cell models A through D based on three different analytical models, one developed here and two others as reported in the literature. The prediction accuracy of these models is judged by the relative difference with the values found by FE simulations using LS-DYNA. With an average

error of 8% for the four tube models, the present analytical model is found to be more accurate than the other two. Detailed description of this study appears in Najafi and Rais-Rohani (2008), with some of the key findings presented in this section of the report.

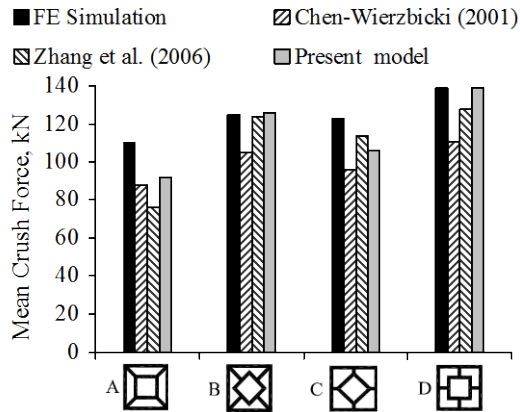


Figure 7. Comparison of numerical and analytical predictions for the mean crush force.

The crush simulations were repeated by switching the material to a magnesium alloy (AZ31) ( $E = 45$  GPa,  $\nu = 0.33$ , and  $\rho = 1.8e-6$  kg/mm<sup>3</sup>), with the true stress-strain curve as shown in Figure 3(b). Using the mean crush force and SEA values, the bar charts in Figure 8 show the difference in performance as a result of material selection. It is worth noting that the material models used here do not consider damage. Therefore, the comparison of different materials is solely based on the plasticity models in Figure 3(b).

**Uncertainty Analysis Using Dimension Reduction and Distribution Fitting**

Random uncertainties in the material properties and boundary conditions can lead to uncertainties in structural responses, such as stress, strain, and damage. Generally speaking, the probability theory can be used to capture the influence of random or stochastic uncertainties in the basic parameters on uncertainty of the resulting random response.

In this section an analytical approach is described and applied to uncertainty analysis of damage as predicted by an internal state variable (ISV) plasticity-damage model (Horstemeyer 2001). ISV

evolution equations, which are formulated at the macroscale level, offer an effective method to capture the microstructure-property relationships. The ISVs reflect the lower spatial size-scale microstructural rearrangements, so that history effects can be modeled. With the help of such a material model, it would be possible to relate structural responses of interest, such as damage, to key material parameters such as particle size, interfacial strength, and spacing at each length scale.

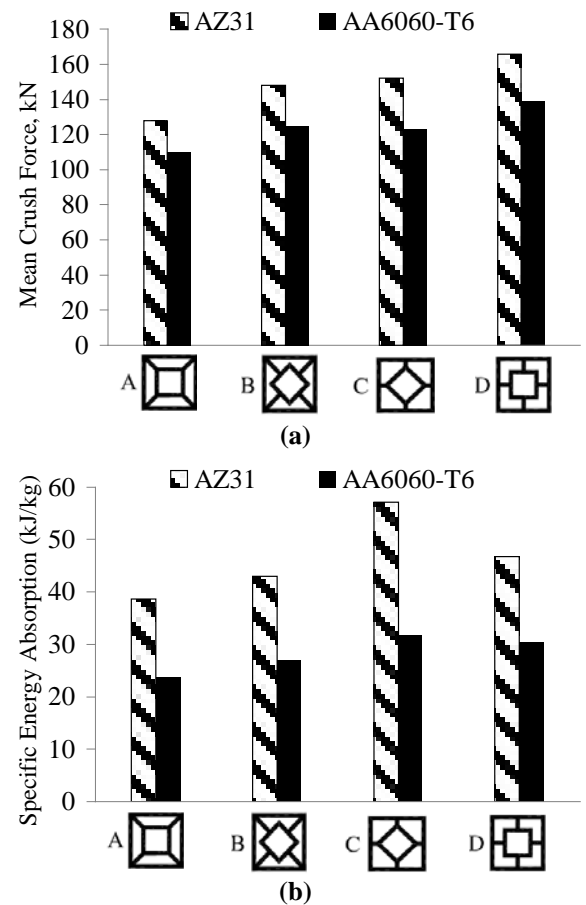


Figure 8. (a) Mean crush force and (b) Specific energy absorption using two different lightweight materials.

Horstemeyer et al. (2005) used a first-order Taylor series expansion to investigate the effects of uncertainty in microstructure features and the boundary conditions that characterize damage evolution in A356 cast aluminum alloy. In particular, void-nucleation, void-growth, and void-coalescence equations were evaluated and

quantified in terms of the sensitivity and uncertainty of various parameters in the constitutive equations. However, the accuracy of a Taylor expansion method largely depends on the scale of uncertainty in the random parameters and the nonlinearity in the corresponding random response.

Recently, Rahman and Xu (2004) proposed the dimension reduction (DR) technique to evaluate a multidimensional integral of a random function by solving multiple one-dimensional integrals. This technique offers an efficient approach for the evaluation of statistical moments such as the mean, variance, skewness, and kurtosis of a random response.

To fully characterize the uncertainty in a random response, such as damage, the estimated moments can be used to find its probability distribution using a suitable probability distribution fitting technique.

Commonly-used distribution fitting techniques include the Pearson and Johnson families of distributions, Saddlepoint approximations, and generalized lambda distributions (GLDs). In this work, we used the extended generalized lambda distribution (EGLD), which combines the GLD with the generalized beta distribution (GBD). The efficiency and accuracy of distribution fitting via GLD and GBD can be found in Karian et al. (1996), Karian and Dudewicz (2000), Lampasi et al. (2005), and King and MacGillivray (2006). After the first four statistical moments of damage are calculated, the parameters of the EGLD are estimated by minimizing the differences between the moments of EGLD and those obtained through DR.

As an illustrative example, we considered the FE simulation of an un-notched A356 aluminum alloy tension specimen loaded at a strain rate of  $10^{-3} \text{ s}^{-1}$  until the point of failure. Using an ISV-based constitutive model (Horstemeyer 2001) in the FE simulations, DR+EGLD technique is used to study the influence of uncertainty in the individual parameters of the ISV model on the uncertainty in damage.

The microstructure of a typical metallic material contains a large number of microdefects such as microcracks, dislocations, pores, and decohesions. Some of these defects are induced during the manufacturing process and are present before the material is subjected to mechanical loads and thermal fields. In general, these defects are small and distributed throughout the material. For A356 cast aluminum alloy, scattered electron microscope images suggest that the material is more isotropic in nature with the secondary constituent particles within the matrix ranging from 3 to 6  $\mu\text{m}$ , with an average size of 4  $\mu\text{m}$  and particle volume fraction of approximately 7%.

Using the experimental data obtained from the testing of A356 specimens, a nonlinear regression algorithm (Horstemeyer, 2001) is used to calculate the ISV model constants. Moreover, the experimental data and associated uncertainties are propagated through a model correlation routine to predict uncertainties in the ISV model parameters. The calculated first-order coefficients of variation (COV) of the plasticity parameters related to the yield strength ( $C_1$  to  $C_6$ ), the kinematic hardening and recovery terms ( $C_7$  to  $C_{12}$ ), the isotropic hardening and recovery terms ( $C_{13}$  to  $C_{18}$ ), and the shear and the bulk moduli ( $G$  and  $K$ ), along with their temperature and strain-rate dependencies ( $a_1$  and  $b_1$ ) are as shown in Table 3. In addition,  $C_a$  and  $C_b$  are the material plasticity parameters related to dynamic recovery and anisotropic hardening terms, respectively. Similarly, the microstructure damage parameters and associated uncertainties are given in Table 4, where  $m$  is void growth constant,  $R_0$  is the initial void radius,  $a$ ,  $b$ , and  $c$  are the stress state-based void nucleation constants,  $C_{coeff}$  is the void-nucleation coefficient parameter,  $K_{ic}$  is the fracture toughness,  $d$  is the particle size,  $f$  is the particle volume fraction,  $cd_1$  and  $cd_2$  are the coalescence factors,  $z$ ,  $DCS$  and  $DCS_0$  are parameters related to grain size and  $C_{CT}$  and  $C_{\eta T}$  are the void-coalescence and the void-nucleation temperature-dependent parameters, respectively. The excluded parameters, with mean and COV of zero, are also shown in Tables 3 and 4 for completeness sake.

The calculated COVs are assumed to be normally distributed and rounded off, due to limited test data. These COVs indicate the scatter in the given

parameters that enable the study of their influences on damage uncertainty.

**Table 3.** Elastic-plastic model constants for A356-T6 aluminum alloys

ID #	Constants (Units)	Mean	COV
1	$G$ (MPa)	25920	0.05
2	$a_1$	1.0	0.05
3	$K$ (MPa)	67630	0.05
–	$b_1$	0.0	0.0
4	Melting temperature ( $^{\circ}\text{K}$ )	5556	0.08
5	$C_1$ (MPa)	53.09	0.08
6	$C_2$ ( $^{\circ}\text{K}$ )	945.3	0.08
7	$C_3$ (MPa)	155.9	0.08
8	$C_4$ ( $^{\circ}\text{K}$ )	110.5	0.08
9	$C_5$ (1/MPa)	0.00001	0.08
–	$C_6$ ( $^{\circ}\text{K}$ )	0.0	0.0
10	$C_7$ (1/MPa)	0.00087	0.08
11	$C_8$ ( $^{\circ}\text{K}$ )	–1877	0.08
12	$C_9$ (MPa)	4820	0.08
13	$C_{10}$ ( $^{\circ}\text{K}$ )	10.94	0.08
14	$C_{11}$ (s/MPa)	0.01369	0.08
15	$C_{12}$ ( $^{\circ}\text{K}$ )	2000	0.08
16	$C_{13}$ (1/MPa)	0.0000165	0.08
17	$C_{14}$ ( $^{\circ}\text{K}$ )	–1000	0.08
18	$C_{15}$ (MPa)	2818	0.08
19	$C_{16}$ ( $^{\circ}\text{K}$ )	4.622	0.08
–	$C_{17}$ (s/MPa)	0.0	0.0
20	$C_{18}$ ( $^{\circ}\text{K}$ )	235.4	0.08
21	$C_a$	–7.0	0.05
22	$C_b$	–0.3776	0.05
23	Initial temperature ( $^{\circ}\text{K}$ )	297	0.10
–	Heat generation coefficient	0.0	0.0

The plot of damage,  $\phi$  as a function of strain,  $\varepsilon$  is shown in Figure 9. Damage values range from zero to one, with a rapid growth beyond the value of ~0.01. Here, the uncertainty in damage depends on the random uncertainties in the ISV model parameters and the strain value selected.

The overall uncertainty analysis procedure using DR+EGLD technique is as follows. First, damage calculations are performed at some selected points in the random variable space. Next, the first four statistical moments of damage are estimated using DR. Then, the probability distribution of damage is approximated with EGLD. Detailed description of this technique is provided in Acar et al. (2008).

**Table 4.** Damage model constants for A356-T6 aluminum alloys

ID #	Constants (Units)	Mean	COV
24	$m$	0.3	0.15
25	$R_o$ (mm)	0.0002	0.25
26	$a$	615369	0.15
27	$b$	58630	0.15
28	$c$	30011	0.15
29	$C_{coeff}$	90.6	0.15
30	$K_{ic}$ (MPa-m <sup>1/2</sup> )	17.3	0.20
31	$d$ (mm)	0.000004	0.25
32	$f$	0.07	0.25
33	$cd_1$	1.0	0.15
–	$cd_2$	0.0	0.0
34	$DCS_o$ (mm)	20	0.15
35	$DCS$ (mm)	20	0.15
36	$z$	0.0509	0.15
	Initial void volume fraction		
37	fraction	0.0001	0.15
38	$C_{\eta r}$	0.6	0.15
–	$C_{CT}$	0.0	0.0

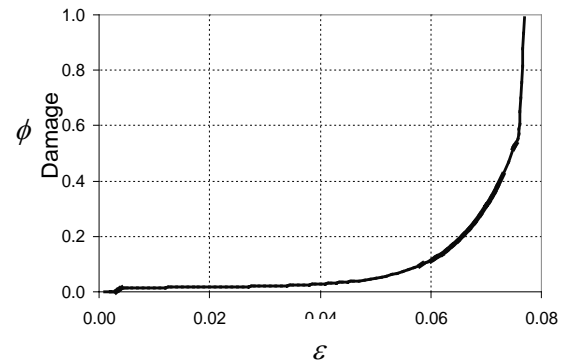


**Figure 9.** Damage vs. strain for A356 aluminum alloy.

The DR+EGLD-based probability density function (PDF) plots of damage at different points along the damage-strain curve (Figure 9) are shown in Figure 10. The mean value and scatter ( $C_\phi$ ) in damage appear to increase as the strain value increases.

For comparison, the PDF plots based on the direct Monte Carlo simulation (MCS) with a sample size of  $10^4$  and those based on a Gaussian (normal) estimation of damage, are also shown. Since the number of random variables is large (38 random variables), in view of the central limit theorem, the

probability distribution of damage can also be represented reasonably well with a normal distribution.

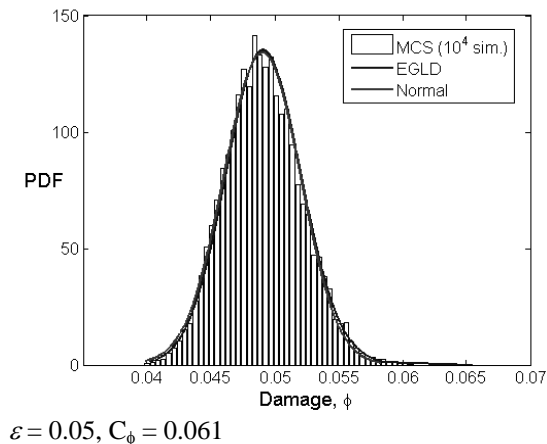
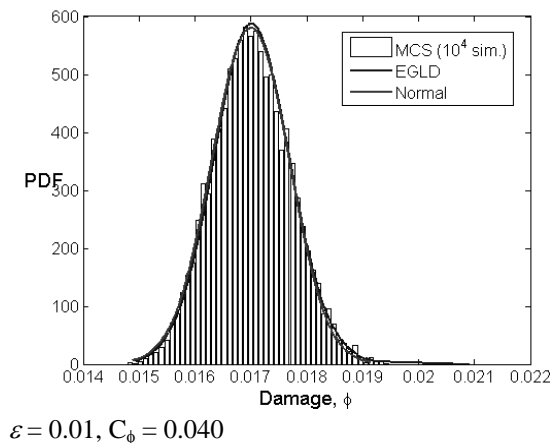
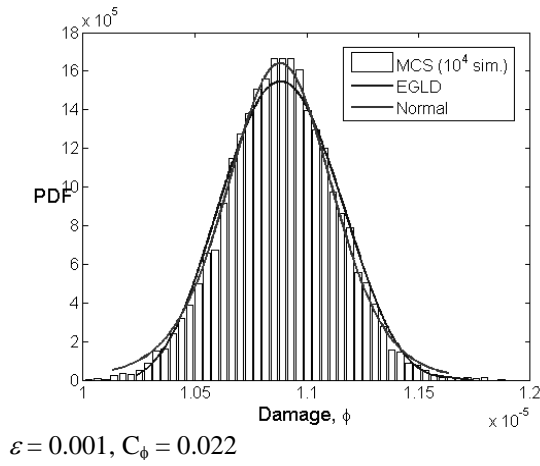


**Figure 10.** Probability distributions of damage at different strain levels.

In addition to uncertainty analysis, the sensitivity of damage to the random variables in Tables 3 and

4 were also investigated. Initially, at  $\varepsilon = 0.001$ , damage is found to be most sensitive to the initial radius of spherical void  $R_0$ , and void-nucleation coefficient  $C_{coeff}$ . With increasing values of strain ( $\varepsilon = 0.01$ ) and corresponding damage in the tensile specimen, the initial temperature, coalescence factor  $cd1$  and initial void volume fraction become more important, and finally, at  $\varepsilon = 0.05$ , the most influential parameters are found to be the fracture toughness  $K_{ic}$ , initial temperature and void-coalescence temperature dependent parameter,  $C_{\eta T}$ .

From the results obtained in this study, we can draw the following conclusions.

1. The scatter in damage, as measured by the coefficient of variation of damage, can increase with strain even though the uncertainties in the input variables are kept fixed.
2. The sensitivities of damage uncertainty to the uncertainties in the input random variables are dependent on the strain values. As the strain value changes (as damage evolves), the importance of the random variables changes.
3. The sensitivities are found to be consistent with the physics of the damage progression. At the very beginning, the void properties (initial size and growth parameters) are found to drive the damage evolution. Then, void coalescence becomes the main driver and finally near the failure condition, macroscopic properties such as fracture toughness, dominate the damage evolution process.

### Reliability Analysis Using Failure Sampling

The reliability assessment of a structural component requires the evaluation of the failure probability of one or more possible failure modes. If the limit state or safety margin for a particular mode is defined by the function  $g(\mathbf{X})$ , where  $\mathbf{X}$  denotes the vectors of random variables, then safety is defined as  $g(\mathbf{X}) > 0$  and failure as  $g(\mathbf{X}) \leq 0$ . The probability of failure is computed according to the multi-integral equation

$$P_f = P(g < 0) = \int_{g(\mathbf{X}) \leq 0} f_x(\mathbf{X}) d\mathbf{X} \quad , \quad (1)$$

where  $f_X(\mathbf{X})$  is the joint PDF of random variables. For most engineering problems, the analytical integration of Eq. (1), or the full distributional approach is not possible. Hence, alternate techniques are often used to find an estimation of  $P_f$  or its corresponding safety index,  $\beta$ .

Popular simulation based methods include Monte Carlo simulation (MCS) and associated variance reduction techniques, such as importance sampling (Rubinstein 1981) and adaptive importance sampling (Wu 1992). Analytical methods such as first- and second-order reliability methods (FORM, SORM) (Madsen et al. 1986) and fast probability integration (Wu and Wirsching 1987) tend to be more efficient than simulation methods, but often with reduced accuracy. Recently, we showed that it is also possible to use the DR+EGLD technique, as discussed in the *Uncertainty Analysis using Dimension Reduction and Distribution Fitting* section, for analytical estimation of failure probability. Details of that study can be found in Acar et al. (2008).

As part of this project, we developed a computationally-efficient simulation-based method that does not rely on a most probable point of failure (MPP) search, such as importance sampling, but can generate accurate results for difficult limit states of relatively high-reliability. We refer to the method as failure sampling (FS). The method is based on a combination of Conditional Expectation and the cumulative distribution function (CDF) or PDF of a portion of the limit state,  $g$ , by direct MCS. If the CDF, or PDF, of  $g$  can be accurately developed, failure probability can be easily calculated by numerical integration over the failure region. The difficulty of developing this curve by MCS is that most samples fall close to the mean of  $g$ , which may be far from the failure region, making accurate integration of this region difficult or impossible. For complex, implicit problems, such as some practical nonlinear engineering problems, requiring an incremental FEA solution for evaluation of the limit state is a realistic concern.

FS solves this problem by reformulating the initial limit state,  $g(\mathbf{X})$ , into a new limit state,  $g_{fs}$ , which

is expressed in terms of a control random variable ( $X_k, k \neq i$ ), representing the ‘load’,  $q$ , and all the remaining random variables, which will collectively represent a ‘resistance’ function,  $R(X_i)$ , with

$$g_{fs} = R(X_i) - q, \quad (2)$$

$g_{fs}$  is mathematically equivalent to  $g$ , hence, failure probability is identical.

Other than statistical independence from the remaining random variables, there is no theoretical limitation to the selection of the control variable; thus,  $X_i$  and  $q$  are not required to be the actual resistance and load random variables of the problem. However, some choices of the control variable may cause FS to fail, though these cases are often easy to identify based on some understanding of the mechanics of the problem. Note that  $g_{fs}$  can be completely implicit and there is no need for an analytical or closed-form formulation.

The value of  $R(X_i)$  at the MPP of  $g_{fs}$  is generally closer to the central region of the PDF of  $R(X_i)$ ,  $f_r$ , than  $g(X_j) = 0$  is to the central region of the PDF of  $g$ ,  $f_g$ . Therefore, if  $f_r$  is generated by MCS, for instance, the calculation of  $P_f$  of  $g_{fs}$  becomes less sensitive to the tail region of  $f_r$ , than is the  $P_f$  of  $g$  to the tail of  $f_g$ . This allows a more accurate computation of  $P_f$  of  $g_{fs}$ , than the  $P_f$  of  $g$ , with the same number of simulations.

The samples needed to estimate  $F_R$  or  $f_r$ , are taken while the condition  $g_{fs} = 0$  is imposed on the process. Practically, this involves conducting MCS to generate values  $x_i$ , then  $R(x_i)$  is evaluated. The value of  $q$  required to set  $g_{fs} = 0$  is then found. Since  $R(x_i) = q$  at failure,  $q$ , therefore, represents a sample of  $R(X_i)$ . With sufficient samples of  $R(X_i)$  obtained, a good estimation of  $F_R$  or  $f_r$  can be obtained and  $P_f$  or  $\beta$  can easily be computed from Eq. (2), using a large variety of available reliability techniques. For many practical (i.e., nonlinear and implicit) problems, imposing  $g_{fs} = 0$  generally requires a higher computational cost per FS sample than MCS sample, as each FS sample requires solution of  $g_{fs} = 0$  for  $q$ . For an implicit, nonlinear problem, this may require multiple iterations. However, as will be shown, this cost is greatly outweighed by the savings in overall

number of samples required, especially as  $P_f$  decreases.

We applied the FS technique to a large number of example problems, two of which are included in this report. Most problems considered have a range of  $\beta$  from 2 to 5, which is a realistic range for most structural reliability problems, although some  $\beta$  beyond this range have also been considered.

**Ten-Bar Nonlinear Truss**

The truss shown in Figure 11 is subjected to a random load,  $P$ , at joint 2. The material model is steel (elastic modulus 29,000 ksi), with a bi-linear stress-strain curve. Yield stress of all members is taken as a single random variable (i.e., yield stress fully correlated), with mean of 50 ksi and COV of 10%. Post-yield (tangent) modulus,  $E_t$ , of all members is also taken as a single random variable, with mean of 1200 ksi and COV of 25%. Thus, including load, there are only three random variables in this problem. Mean value of  $P$  is varied from 40 to 60 kips, with COV of 10%. All random variables are normally distributed. Failure is defined as the state when the vertical displacement,  $d$ , of joint 2 reaches 1.5 inches.

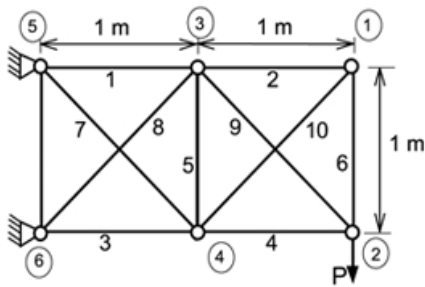


**Figure 11.** Ten-bar Truss.

The limit state is expressed as

$$g = 1.5 - d(\sigma_y, E_t, P) \quad (3)$$

with  $P$  treated as the control variable. The nonlinear truss problem is analyzed using the FEA code MSC Nastran with Newton-Raphson solution. For FS,  $P$  is selected as the control variable and the bisection method is used to find the value for which  $g_{fs} = 0$  (error tolerance taken

as 0.01). Results are given in Table 5 for a mean load of 50 kips.

**Table 5.** Comparison of results for the truss example

Method	No. of calls	CPU time (hr)	$\beta$	% err
Exact	$10^5$	43	2.35	–
FS (NI)	1000	3	2.36	0.5
FS (FORM)	1000	3	2.35	0.3
FORM (RF)	15–239	0.017–0.17	7.85	235
SORM	25–444	0.034–0.25	5.67	142
MCS	7000	3	2.27	3.4
LHS	7000	3	2.43	3.7
IS	7000	3	2.34	0.3

In Table 5, the “Exact” result is based on  $10^5$  MCS samples, with each requiring a separate FE solution. FS (FORM) refers to calculating  $\beta$  from Eq. (2) with FORM once  $f_r$  was estimated with FS results, whereas FS (NI) refers to calculating  $P_f$  from FS results by numerical integration.

$$p_f = \int_{-\infty}^{\infty} F_R(x) f_q(x) dx \quad (4)$$

Equation (4) is a 2-random variable form of Eq. (1), once  $F_R$  is estimated from FS results.

Then, using the standard normal transformation  $\beta = -\Phi^{-1}(P_f)$ , generalized  $\beta$  is reported in the table. FORM (RF) applies the Rackwitz-Fiessler (1978) search algorithm to locate the MPP, while SORM refers to the common parabolic approximation of Breitung (1984). LHS refers to Latin Hypercube sampling. Using the correlation reduction technique as described by Inman and Conover (1982), it was generally found that MCS is equally if not more effective than LHS with only 1000 samples, though LHS can provide significant improvements over MCS with a larger number of simulations (Eamon et al. 2005). The simple version of importance sampling (IS) considered the uses of the MPP found from FORM (RF), while the importance sampling function is taken as the joint probability density function of the original limit state, with the random variables’ means shifted to the MPP.



The simulation methods were given equal CPU time, rather than equal number of calls. This is because an FS call is more costly than the others for this type of implicit problem due to the need to satisfy the constraint  $g_{fs} = 0$  for each sample. This resulted in the other simulation methods, acquiring seven times the number of samples as FS. Even so, FS out-performed the comparison methods, resulting in a more accurate solution for the same overall CPU time. This is particularly apparent at the highest  $\beta$  level.

### Crush Tube

A square tube, 400 mm long and 80 mm wide, with an end mass,  $m$ , and initial velocity,  $V$ , strikes a rigid wall. Random variables are the tube density,  $\rho$ , end mass,  $m$ , tube thickness,  $t$ , initial velocity,  $V$ , Young's modulus,  $E$ , yield stress,  $\sigma_y$ , and tangent modulus,  $E_t$ . Statistical properties of the random variables are given in Table 6.

**Table 6.** Properties of the random variables

RV	Mean	COV	Distribution
$\rho$	$2.70 \times 10^{-6}$ kg/mm <sup>3</sup>	0.05	normal
$m$	800 kg	0.15	normal
$t$	4 mm	0.01	normal
$V$	11 m/s	0.10	normal
$E$	69 GPa	0.10	lognormal
$\sigma_y$	0.175 GPa	0.15	normal
$E_t$	0.265 GPa	0.15	normal

Failure is defined as the crush distance exceeding 50% of the tube's original length, or 200 mm at 20 ms after impact. The limit state is given as

$$g = 200 - d(\rho, m, t, V, E, \sigma_y, E_t) \quad (5)$$

The limit state is evaluated with the FEA code LS-DYNA, using a (explicit) central difference integration scheme for solution. The tube is modeled using quadrilateral shell elements. Due to the computational cost of this problem, only 100 FS samples are considered. As each FS sample takes approximately three times as long as an MCS sample, the other simulation methods each achieve approximately 300 samples for the same CPU time. Results are given in Table 7. The MCS samples were plotted on probability paper to verify results. Here only FS was able to provide a solution and was very accurate. By contrast, FS

(FORM), SORM and IS methods could not converge to an acceptable solution.

**Table 7.** Comparison of results for the crush tube example

Method	No. of calls	CPU time	$\beta$	% err
Exact	60,000	10 days	2.28	–
FS (NI)	100	25 hrs	2.23	–2.3
FORM	104	9 hrs	2.54	11
MCS	300	25 hrs	2.11	7.1
LHS	300	25 hrs	2.22	–2.8

The results of this investigation show that the new FS approach can provide accurate results for a wide range of reliability problems at considerable computational savings.

### Conclusions

A summary of research activities under the general area of simulation-based design optimization were presented. Good progress was made in a number of areas, including topology optimization, energy absorption characterization of extruded multi-cell crush tubes, uncertainty quantification, and reliability analysis.

### Presentations/Publications/Patents

1. E. Acar and M. Rais-Rohani, "Ensemble of Metamodels with Optimized Weight Factors," *Structural and Multidisciplinary Optimization*, **37**, No. 3, 2008, pp. 279–294.
2. E. Acar, K. Solanki, M. Rais-Rohani, and M. Horstemeyer, "Uncertainty Analysis of Damage Evolution Computed Through Microstructure-Property Relations," *Proceedings of the ASME 2008 International Design Engineering Technical Conferences & Computers and Information in Engineering Conference (IDETC/CIE)*, New York City, NY, Aug 3–6, 2008.
3. A. Najafi and M. Rais-Rohani, "Influence of Cross-Sectional Geometry on Crush Characteristics of Multi-cell Prismatic Columns," *Proceedings of the 49th AIAA/ASME/ASCE/AHS/ASC Structures, Structural Dynamics, and Materials Conference*, Schaumburg, IL, Apr 7–10, 2008.

4. M. Rouhi and M. Rais-Rohani, "Topology Optimization of Continuum Structures Using Element Exchange Method," *Proceedings of the 4th AIAA Multidisciplinary Design Optimization Specialist Conference*, Schaumburg, IL, Apr 7–10, 2008.
5. E. Acar, M. Rais-Rohani, and C. Eamon, "Reliability Estimation using Dimension Reduction and Extended Generalized Lambda Distribution," *Proceedings of the 10th AIAA Non-Deterministic Approaches Conference*, Schaumburg, IL, Apr 7–10, 2008.
6. E. Acar and M. Rais-Rohani, "Ensemble of Metamodels with Optimized Weight Factors," *Proceedings of the 4th AIAA Multidisciplinary Design Optimization Specialist Conference*, Schaumburg, IL, Apr 7–10, 2008.
7. B. Charumas, "A New Technique for Structural Reliability Analysis," MS Thesis, Mississippi State University, May 2008.
- Thin-Walled Structures in Energy Absorption," *Thin-Walled Structures*, **39**, No. 4, 2001, pp. 287–306.
6. C. Eamon, M. Thompson, and Z. Liu, "Evaluation of Accuracy and Efficiency of some Simulation and Sampling Methods in Structural Reliability Analysis," *Journal of Structural Safety*, **27/4**, pp. 356–392, 2005.
7. P. C. Fourie and A. A. Groenwold, "The Particle Swarm Algorithm in Topology Optimization," *Proceedings of the Fourth World Congress of Structural and Multidisciplinary Optimization*, Dalian, China, 2001.
8. M. F. Horstemeyer, "From Atoms to Autos, A New Design Paradigm Using Microstructure-Property Modeling, Part 1: Monotonic Loading Conditions," Sandia National Laboratories, Sand2000-8662, Mar 2001.
9. M. F. Horstemeyer, K. Solanki, and W. G. Steele, "Uncertainty Methodologies to Characterize a Damage Evolution Model," *Proceedings of International Journal of Plasticity Conference*, Kauai, Hawaii, Jan 2005.
10. R. L. Inman and W. J. Conover, "A distribution-free approach to inducing rank correlation among input variables," *Communications in Statistics*, **11**, No. 3, pp. 311–334, 1982.
11. Z. E. Karian, E. J. Dudewicz, and P. McDonald, "The Extended Generalized Lambda Distribution System for Fitting Distributions to Data: History, Completion of Theory, Tables, Applications, the "Final Word" on Moment Fits", *Communications in Statistics—Computation and Simulation*, **25**, No. 3, 1996, pp. 611–642.
12. Z. Karian and E. Dudewicz, "Fitting Statistical Distributions to Data: The generalized Lambda Distribution and the Generalized Bootstrap Methods", CRC Press, Boca Raton, FL, 2000.
13. R.A.R. King and H.L. MacGillivray, "Fitting the Generalized Lambda Distribution with Location and Scale-Free Shape Functionals," *Proceedings of the Symposium on Fitting*

## **References**

1. E. Acar, K. Solanki, M. Rais-Rohani, and M. F. Horstemeyer, "Uncertainty Analysis of Damage Evolution Computed Through Microstructure-Property Relations," *Proceedings of the ASME 2008 International Design Engineering Technical Conferences & Computers and Information in Engineering Conference (IDETC/CIE 2008)*, New York, NY, Aug 3–8, 2008.
2. E. Acar, M. Rais-Rohani, and C. Eamon, "Reliability Estimation using Dimension Reduction and Extended Generalized Lambda Distribution," *Proceedings of the 10th AIAA Non-Deterministic Approaches Conference*, Schaumburg, IL, Apr 7–10, 2008.
3. M. P. Bendsoe, "Optimal Shape Design as a Material Distribution Problem," *Journal of Structural and Multidisciplinary Optimization*, **1**, No. 4, 1989, pp. 193–202.
4. K. Breitung, "Asymptotic Approximations for Multinormal Integrals," *Journal of Engineering Mechanics*, ASCE, **110**, No. 3, pp. 357–366, 1984.
5. W. Chen and T. Wierzbicki, "Relative Merits of Single-Cell, Multi-Cell and Foam-Filled

- Statistical Distributions to Data, Auburn, AL, Mar 2006.
14. D. A. Lampasi, F. D. Nicola, L. Podesta, "The Generalized Lambda Distribution for the Expression of Measurement Uncertainty," IEEE Instrumentation and Measurement Conference, Ottawa, Canada, May 2005.
  15. H. O. Madsen, S. Krenk, and N. C. Lind, *Methods of Structural Safety*, Prentice Hall, Englewood Cliffs, NJ, 1986.
  16. A. Najafi and M. Rais-Rohani, "Influence of Cross-Sectional Geometry on Crush Characteristics of Multi-cell Prismatic Columns," Proceedings of the 49th AIAA/ASME/ASCE/AHS/ASC Structures, Structural Dynamics, and Materials Conference, Schaumburg, IL, Apr 7–10, 2008.
  17. N. Olhoff, E. Ronholt, and J. Scheel, "Topology Optimization of three-dimensional structures using optimum microstructures," *Structural Optimization*, **16**, No. 1, 1998, pp. 1–18.
  18. R. Rackwitz and B. Fiessler, "Structural Reliability Under Combined Random Load Sequences," *Computers and Structures*, **9**, No. 5, pp. 484–494, 1978.
  19. S. Rahman and H. Xu, "A Univariate Dimension-Reduction Method for Multi-dimensional Integration in Stochastic Mechanics," *Probabilistic Engineering Mechanics*, **19**, No. 4, 2004, pp. 393–408.
  20. M. Rouhi and M. Rais-Rohani, "Topology Optimization of Continuum Structures Using Element Exchange Method," Proceedings of the 4th AIAA Multidisciplinary Design Optimization Specialist Conference, Schaumburg, IL, Apr 7–10, 2008.
  21. R. Y. Rubinstein, *Simulation and the Monte Carlo Method*, John Wiley & Sons, New York, 1981.
  22. S. Y. Wang, K. Tai, and M. Y. Wang, "An Enhanced Genetic Algorithm for Structural Topology Optimization," *International Journal of Numerical Methods in Engineering*, **65**, No. 1, 2006, pp. 18–44.
  23. T. Wierzbicki and W. Abramowicz, "On the Crushing Mechanics of Thin Walled Structures," *Journal of Applied Mechanics*, **50**, 1983, pp.727–734.
  24. Y. T. Wu, "An Adaptive Importance Sampling Method for Structural Systems Analysis," Reliability Technology, edited by T.A. Cruse, ASME Winter Annual Meeting, Vol. AD 28, Anaheim, CA, pp. 217–231, 1992.
  25. Y. T. Wu and P. H. Wirsching, "New Algorithm for Structural Reliability Estimation," *Journal of Engineering Mechanics*, ASCE, **113**, No. 9, pp. 1319–1336, 1987.
  26. X. Zhang, G. Cheng, and H. Zhang, "Theoretical Prediction and Numerical Simulation of Multi-Cell Square Thin-Walled Structures," *Thin-Walled Structures*, **44**, No. 11, 2006, pp. 1185–1191.
  27. M. Zhou and G.I.N. Rozvany, "The COC algorithm, part II: Topological, Geometry and Generalized Shape Optimization," *Computer Methods in Applied Mechanics and Engineering*, **89**, No. 1–3, 1991, pp. 197–224.

## M. Fatigue of Lightweight Automotive Materials

*Principal Investigator: Mark F. Horstemeyer*

*Chair in Solid Mechanics and Professor, Dept. of Mechanical Engineering*

*Center for Advanced Vehicular Systems*

*Mississippi State University*

*206 Carpenter Bldg., P.O. Box ME*

*Mississippi State, MS 39762*

*(662) 325-7308; fax: (662) 325-7223; e-mail: mforst@me.msstate.edu*

*Co-Principal Investigator: Paul T. Wang*

*Manager, Computational Manufacturing and Design*

*Center for Advanced Vehicular Systems*

*Mississippi State University*

*P.O. Box 5405*

*Mississippi State, MS 39762-5405*

*(662) 325-2890; fax: (662) 325-5433; e-mail: pwang@cavs.msstate.edu*

*Co-Principal Investigator: Adrian Pascu*

*Postdoctoral Associate, Engineering*

*Center for Advanced Vehicular Systems*

*Mississippi State University*

*P.O. Box 5405*

*Mississippi State, MS 39762-5405*

*(662) 325-3812; email: ap326@msstate.edu*

*Co-Principal Investigator: Yibin Anna Xue*

*Assistant Professor, Mechanical and Aerospace Engineering*

*Utah State University*

*4130 Old Main Hill*

*Logan, UT 84322*

*(435) 797-2867, e-mail: <http://www.mae.usu.edu/personnel/faculty.php>*

*Technology Area Development Manager: Joseph A. Carpenter*

*(202) 586-1022; fax: (202) 586-1100; e-mail: joseph.carpenter@ee.doe.gov*

*Field Project Officer: Aaron D. Yocum*

*(304) 285-4852; fax: (304) 285-4403; e-mail: aaron.yocum@netl.doe.gov*

---

*Contractor: Mississippi State University (MSST)*

*Contract No.: 4000054701*

---

### Objective

- Develop and experimentally validate prognostic tools for in-service life prediction and fatigue design of lightweight automotive materials and components. An extensive test program is being conducted for AZ31D and AM30 magnesium (Mg) extrusion alloys. A multistage fatigue (MSF) model, which considers fatigue life to comprise incubation, microstructurally small crack growth, and large crack growth, will be developed for Mg alloys.

## Approach

- Develop methodologies for simulating microstructurally-small cracks in selected magnesium alloys. Observation of the incubation lives for the selected magnesium alloys, measurement and correlation of the growth of microstructurally small cracks and large-crack behavior will be conducted for development of the physics-based models. (Task 1)
- Perform a literature survey on fatigue and small-crack behavior in magnesium alloys; conduct fatigue and crack-growth tests on selected magnesium alloys; conduct monotonic and cyclic stress-strain tests, uniaxial, and multi-axial fatigue tests on AZ31; conduct fatigue tests for the United State Automotive Materials Partnership (USAMP) round robin; and use data from the Fatigue and Durability Research Program to validate the models. (Task 2)
- Perform in situ scanning electron microscopy (SEM) fatigue tests on selected alloy(s) to identify crack initiation site(s) and metallurgical features. We will conduct in situ studies on the fatigue and crack behavior of the selected magnesium alloy. (Task 3)
- Correlate the influence of grain boundaries, crack shapes, and plasticity effects on the fatigue models. We will conduct microstructural studies on the influence of grain boundaries on crack growth, the effects of plastic deformations on the fatigue, and fatigue crack-growth behavior. (Task 4)
- Experimentally validate the models with a selected material and non-proprietary automotive component tested under in-service loading specified by sponsors. (Task 5)

## Accomplishment

- Conducted literature surveys on fatigue and small-crack growth in magnesium alloys. (Task 2)
- Developed a detailed Statement of Work on “Development of Microstructure-Based Multistage Fatigue Models for Alloys Utilized in Automotive Mg Front End Project.” (Task 2)
- Developed test matrix and test specimens for tensile and fatigue tests on the magnesium alloys to determine material parameters for the MSF model. (Task 2)
- Conducted MultiStage Fatigue (MSF) analyses of cast AZ91 material and components. (Task 1)
- Conducted preliminary fatigue crack-growth analyses and correlations of crack-growth rates for AZ91E to determine material parameters for Small-Crack Theory model. (Task 1)
- Conducted fatigue analyses on unnotched strain-controlled tests on AZ91E coupons using Small Crack Theory. (Task 1)
- Acquired AZ31D and AM30 extrusions from General Motors (GM). (Task 2)
- Determined composition and particle morphology and distributions for AZ31D and AM30 Mg alloys from GM. (Task 2)
- Developed a detailed test plan for the tensile and fatigue specimens to be machined from AZ31D and AM30 extrusions. (Task 2)
- Initiated tensile testing on the extruded AZ31D and AM30 alloy. (Task 2)
- Published a conference paper on MTS 2008 on fatigue of Mg AZ31. (Task 1)

## Future Direction

- Evaluate and model fatigue behavior of self-piercing rivet (SPR) lap joint configuration
  - Develop candidate SPR specimen
  - Uniaxial tensile strain-life testing ( $R > 0$ )
  - Microstructural evaluations

- Evaluate and model fatigue behavior of Mg AZ31D and AM30 extrusions
  - Evaluate grain size, orientation, and distribution for given Mg alloys
  - Complete the monotonic and cyclic stress-strain tests on the given extrusion samples
  - Conduct uniaxial strain-life tests with mean stress effects ( $R = -1$ , and  $R = 0.1$ )
  - Evaluate fractographs of fatigue specimens, identify incubation site(s) and fatigue stages
  - *In situ* SEM tests on AZ31 and AM30 coupons to study fatigue incubation and crack-growth behavior (collaboration with Chinese partners)
  - Perform MSF analyses of the uniaxial, strain-controlled fatigue tests on unnotched Mg coupons
- Fatigue components design
  - Obtain in-service spectrum loading sequences from automotive industry
  - Conduct MSF analyses under in-service variable-amplitude loading.
- Publications and reports
  - Submit a paper on the fatigue analysis of the AZ91E alloy using Small Crack Theory to the *International Journal of Fatigue*.
  - Complete a full report on fatigue analyses of AZ31D and AM30 under constant and variable amplitude loading.

**Introduction**

Prognostic tools for in-service life prediction of lightweight automotive materials and components are being developed and validated for magnesium alloys. Stress-strain tests and fatigue tests under low- and high-cycle fatigue conditions are being conducted. Detailed observations of the fatigue failure process will guide development of the physics-based models.

**Quasi-static Tensile Tests for AM30 Mg Alloy**

We ran the tensile tests with strain rate  $10^{-3}$ /sec, at  $T_1 = 300K$ , using the Instron 5869 machine and the Epsilon extensometer (Epsilon 3542-0100-025-ST). The tensile true stress-strain curves are presented in Figure 1. The tensile tests and elastic results are summarized in Table 1. The initial linear modulus were obtained using the least square regression technique from the tensile curve; however, this value is smaller than the elastic modulus obtained from unloading (unloading is more correct).

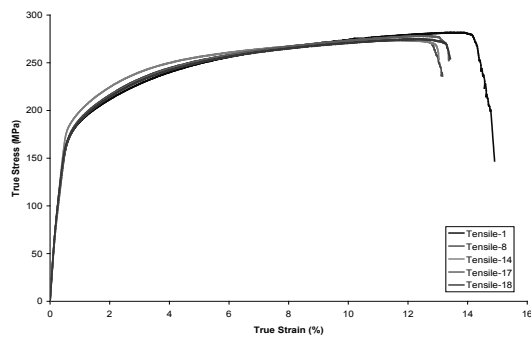


**Figure 1.** True stress-true strain curves for tensile tests at  $T_1 = 300K$  and strain rate  $10^{-4}$ /sec for AM30 Mg alloy.

**Table 1.** Tensile properties of AM30 Mg alloy at a strain rate of  $10^{-3}$ /s at  $T_1 = 300K$

Sample ID	Initial dimension	Linear modulus	Elastic modulus	Yield stress	Ultimate stress	Failure strain
	b x h [mm x mm]	[GPa]	[GPa]	[MPa]	[MPa]	[%]
Tensile-1	6.4 x 5.1	33.59	42.00	167.8	276.4	14.20
Tensile-8	6.4 x 5.1	32.49	42.00	170.2	268.4	12.83
Tensile-14	6.4 x 5.1	36.35	42.00	183.3	264.7	12.89
Tensile-17	6.4 x 5.1	32.69	42.00	168.9	272.1	13.19
Tensile-18	6.4 x 5.1	34.36	42.00	169.7	268.4	13.29
Average		33.90		172.0	270.0	13.30
SDV		1.56		6.39	4.45	0.54
CoV (%)		4.61		3.72	1.65	4.02

Figure 2(a) shows one specimen (Tensile-18) before the test and Figure 2(b) shows the same specimen after the tensile test at T1= 300K.

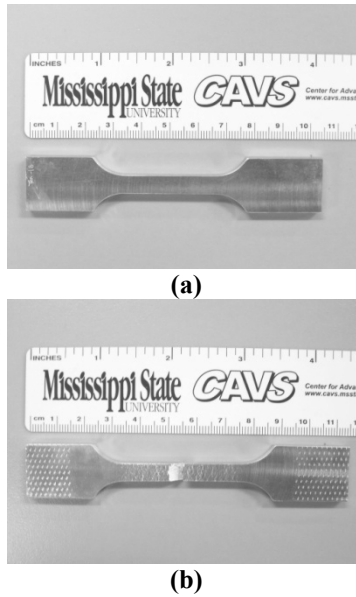


**Figure 2.** AM30 Mg alloy specimen (a) before test and (b) after the test at T1 = 300K.

Using the same Instron machine and an Instron extensometer (Instron 263-107 GL 25 mm), we ran the tensile tests with strain rate  $10^{-3}$  /sec, at T2=400K. The tensile tests and elasticity results are summarized in Table 2. The tensile true stress-strain curves are presented in Figure 3.

**Table 2.** Tensile properties of AM30 Mg alloy at a strain rate of  $10^{-3}$  /s at a T2=400K

Sample ID	Initial dimension b x h [mm x mm]	Linear modulus [GPa]	Elastic modulus [GPa]	Yield stress [MPa]	Ultimate stress [MPa]	Failure strain [%]
Tensile-1	6.4 x 5.1	30.42	42.00	147.51	197.6	33.42
Tensile-8	6.4 x 5.1	29.75	42.00	136.67	214.0	36.57
Tensile-14	6.4 x 5.1	27.63	42.00	124.76	173.5	47.09
Tensile-17	6.4 x 5.1	27.38	42.00	119.72	208.3	39.45
Tensile-18	6.4 x 5.1	23.98	42.00	120.44	208.2	33.86
Average		27.81	42.00	129.8	200.3	38.28
SDV		2.56		11.99	16.14	5.39
CoV (%)		9.19		9.24	8.06	14.09

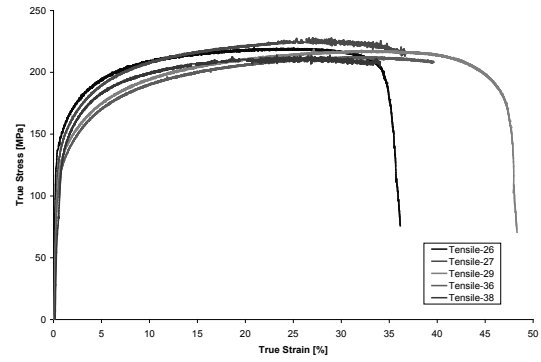


**Figure 3.** True stress-true strain curves for tensile tests at T2 = 400K and strain rate  $10^{-3}$  /sec for AM30 Mg alloy.

Figure 4(a) shows one specimen (Tensile-26) before the test and Figure 4(b) shows the same specimen after the tensile test at T2=400K. Figure 2(b) shows one specimen after the tensile test at T1=300K and Figure 4(b) shows the similar specimen after the tensile test at T2=400K. Figure 5 presents a comparative plot.

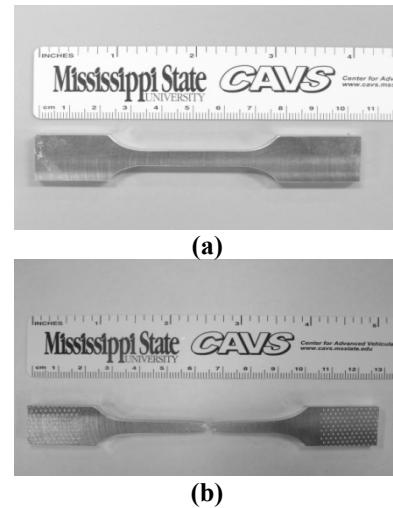


**Figure 4.** AM30 Mg alloy specimen (a) before test and (b) after the test at T2 = 400K.

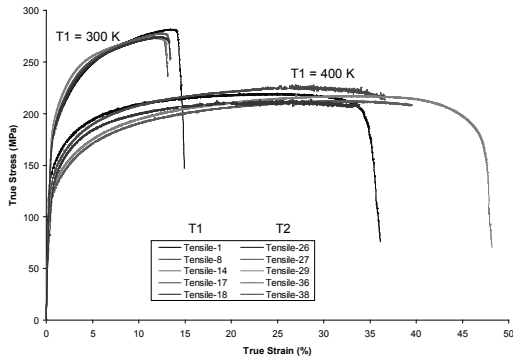


**Figure 5.** Comparative plots true stress-true strain curves for AM30 Mg sample tested in uniaxial tensile tests at T1 = 300K and T2 = 400K.

After these tests, we observed a decrease in the failure stress for testing at 400K with approximately 38% ( $\sigma_{HT} = 200.3$  MPa,  $\sigma_{RT} = 268.4$  MPa) compared to the tests at 300K, and an increase of failure strain with approximately 187% ( $\epsilon_{HT} = 38.2\%$ ,  $\epsilon_{RT} = 13.30\%$ ) compared with the same tests at 300K. Typical scanning electron microscope (SEM) images of the fracture surfaces of the AM30 tensile specimens tested at 300K and 400K is shown in Figure 6(a) and 6(b), respectively.

**Quasi-static Compression Tests at T1=300K for AZ31 Mg Alloy**

We ran compression tests with strain rate  $10^{-3}/\text{sec}$ , at T1=300K using the Instron 5869 machine and the Instron extensometer (Instron 263-107 GL 25 mm). The compression test results were summarized in Table 3. The stress-strain behavior is presented in Figure 7 for the extruded and transverse directions. The tests were run for three specimens, cutting one in the transverse direction (CT-2, CT-5) and cutting two specimens in the extruded direction (CE-1, CE-3, CE-4). Figure 8 shows the compression specimen after the test at T1=300K.

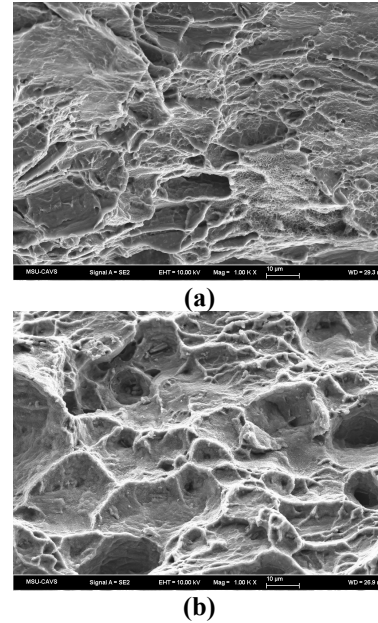


**Figure 6.** SEM fracture surface images with different magnification of the AM30 tensile specimens at (a) T1 = 300K tested with  $10^{-3}/\text{sec}$  strain rate and (b) T2 = 400K with  $10^{-3}/\text{sec}$  strain rate.

**Table 3.** Compression properties of AZ31 Mg alloy at a strain rate of  $10^{-3}/\text{s}$  at T1 = 300K

Sample ID	Initial dimension b x h [mm x mm]	Failure strain [MPa]	Failure stress [MPa]	Maximum stress [MPa]
CE-1	12.75 x 25.50	53.81	293.96	334.82
CE-3	12.75 x 25.50	55.06	336.24	355.65
CE-4	12.75 x 25.50	62.08	319.17	354.64
Average		56.98	316.46	348.37
SDV		4.46	21.27	11.75
CoV (%)		7.82	6.72	3.37
CE-3	12.75 x 25.50	35.44	235.61	271.70
CE-4	12.75 x 25.50	36.37	244.65	276.30
Average		35.91	240.13	274.00
SDV		0.66	6.39	3.25
CoV (%)		1.83	2.66	1.19

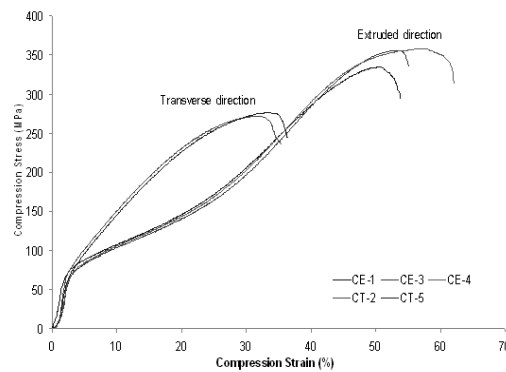


**Figure 7.** Compression stress-strain curves of five AZ31 Mg alloy samples, tested at a strain rate of  $10^{-3}/\text{s}$  and temperature T1 = 300K.



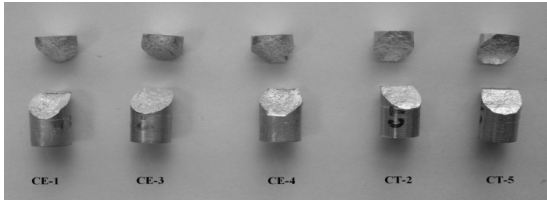


**Figure 8.** Compression specimens (AZ31) after the test at  $T_1 = 300K$ .

**Fatigue Tests for AM30 Mg Alloy**

The fatigue tests for AM30 Mg alloy were performed using a MTS machine (model MTS-810) with a 100 kN capacity. Also used was an extensometer (MTS model no.: 634-31F-25, gauge length: 10 mm) in order to control strain signal and measure strain (Figure 9). The fatigue tests were performed at room temperature for a fully reversed loading cycle ( $R = \epsilon_{min}/\epsilon_{max} = -1$ ) and for two strain amplitudes of 0.6 % and 0.3 % (there are more planned at different strain amplitudes). Figure 10 shows the experimental strain-life for AM30 Mg alloy. The number of failure cycles for each specimen is shown in Table 4 and the hysteresis for the first, middle, and last cycles for a few tests are presented in Figure 11.



**Figure 9.** Fatigue tests setup.

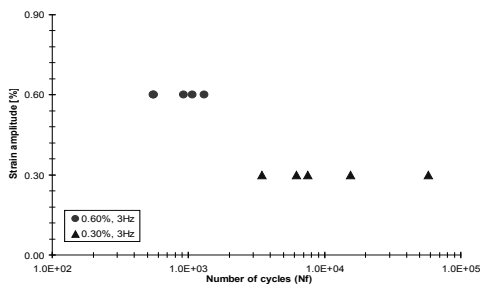
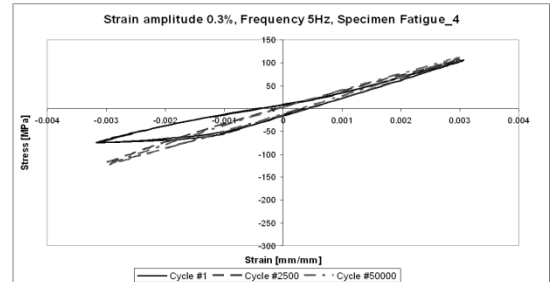


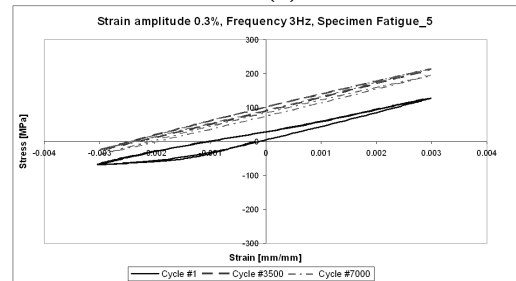
**Figure 10.** Experimental AM30 Mg strain life curve.

**Table 4.** Number of failure cycles for each specimen tested

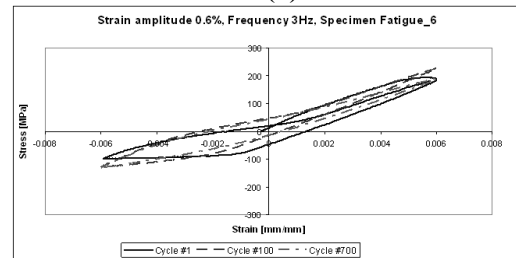
Strain amplitude [%]	Frequency [Hz]	Nf Specimen 1	Nf Specimen 2	Nf Specimen 3	Nf Specimen 4	Nf Specimen 5
0.3	5	6,212	15,488	3,459	57,891	7,491
Strain amplitude [%]	Frequency [Hz]	Nf Specimen 6	Nf Specimen 7	Nf Specimen 8	Nf Specimen 9	Nf Specimen 10
0.6	3	919	1,310	558	1,071	553



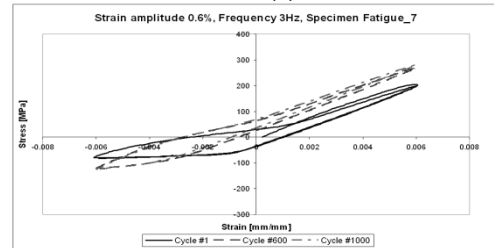
(a)



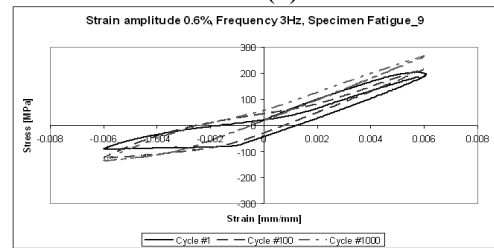
(b)



(c)



(d)



(e)

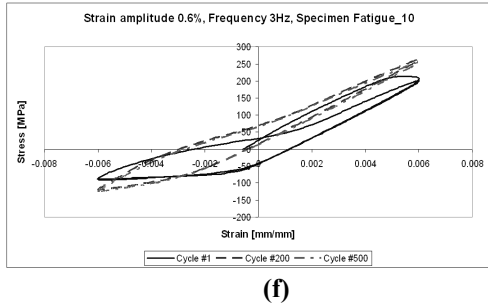


**Figure 11.** Hysteresis for different AM30 Mg alloy specimen at first, middle, and last cycle.

Using these test results, we have a preliminary model-experiment correlation for the extruded AM30 magnesium alloy. In Figure 12, the correlation between experimental results and MSF model results are presented.

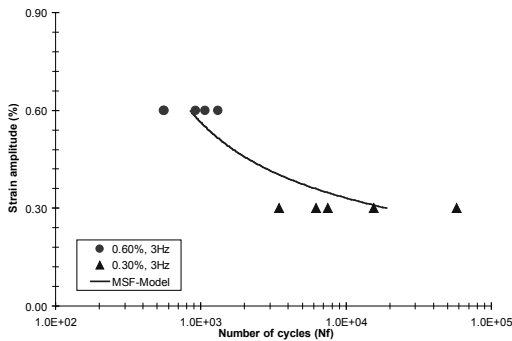


**Figure 12.** MSF model-experiment correlation showing the strain-life behavior for AM30 Mg alloy.

### Fatigue Tests for AZ31 Mg Alloy

Fatigue tests for the AZ31 Mg alloy were performed using the same MTS machine (model MTS-810) with 100 kN capacity and the same extensometer (MTS model no.: 634-31F-25, gauge length: 10 mm) for controlling the strain signal and to measure strain. Also, the fatigue tests for these materials were performed at room temperature for a fully reversed loading cycle ( $R = \epsilon_{\min} / \epsilon_{\max} = -1$ ) and for seven strain amplitudes: 0.2%, 0.25%, 0.3%, 0.4%, 0.5%, 0.6%, and 0.7%. In Figure 13, the experimental strain-life for AZ31 Mg alloy is presented. The number of failure cycles for each specimen is shown in Table 5.

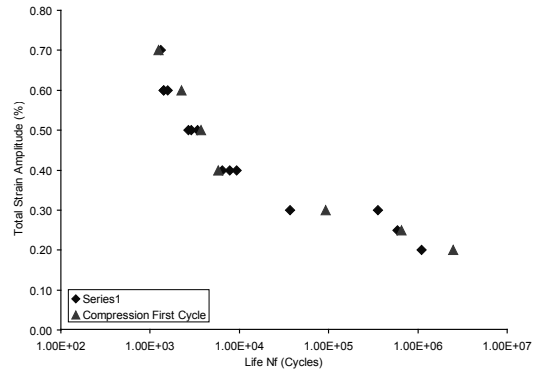


**Figure 13.** Experimental strain-life behavior for AZ31 Mg alloy.

**Table 5.** Number of failure cycles for each AZ31 Mg alloy specimen tested.

Sample ID	Diameter [mm]	Area [mm <sup>2</sup> ]	Strain amplitude [%]	Frequency [Hz]	Cycles failure [f]	Comments
UF2-12	6.10	29.19	0.70	1	1,308	
UF-6	6.10	29.19	0.70	1	1,246	compression first cycle
UF-2	6.32	31.42	0.60	1	1,583	
UF-11	6.30	31.16	0.60	1	1,426	
UF-10	6.32	31.42	0.60	1	1,424	
TL2-5	6.29	31.04	0.60	1	2,258	compression first cycle
UF-7	6.35	31.67	0.50	2	2,698	
UF-3	6.32	31.42	0.50	2	3,380	
UF-5	6.35	31.67	0.50	2	2,875	
UF2-11	6.32	31.42	0.50	1	3,697	compression first cycle
UF-14	6.32	31.42	0.40	3	6,400	
UF-4	6.34	31.54	0.40	3	9,381	
UF-12	6.32	31.42	0.40	2	7,831	
UF-9	6.32	31.42	0.40	2	5,786	compression first cycle
UF-13	6.35	31.67	0.30	3	36,852	
UF-1	6.34	31.54	0.30	3	356,043	
UF2-7	6.32	31.42	0.30	3	92,084	compression first cycle
UF2-TL2-6	6.18	30.04	0.25	4	591,620	
UF2-5	6.29	31.04	0.25	3	657,005	compression first cycle
UF-8	6.32	31.42	0.20	3	1,099,874	
UF2-TL2-4	6.32	31.42	0.20	4	2,486,100	compression first cycle

Using these test results, we started the model—experimental correlation for the AM30 magnesium alloy. In Figure 14, the correlation between experimental results and MSF modeling results are presented.

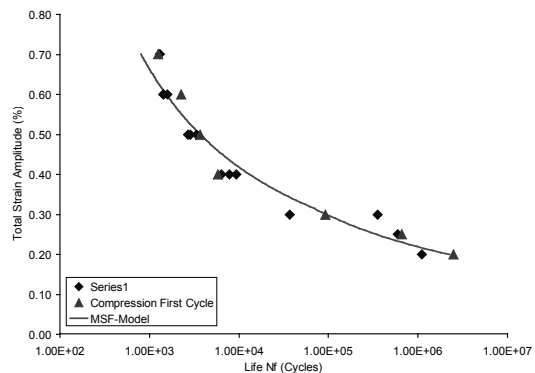


**Figure 14.** Model/Experimental correlation showing the strain life curve for AM30 Mg alloy.

### **Conclusions**

Two magnesium extruded alloys, AZ31 and AM30, provided by our automotive sponsors, were investigated. Tensile and fatigue tests were conducted to generate mechanical properties for calibrating a physics-based MultiStage Fatigue (MSF) model. Fatigue lives under strain-controlled loading conditions were obtained. Preliminary results of AM30 and AZ31 extruded alloys were used to calibrate the MSF model. The

MSF model could account for the influence of the manufacturing process of the strain-life behavior. Model development will be continued in Phase II of the program.

### **Presentations/Publications/Patents**

1. Y. Xue, M. Lugocamarena, M. F. Horstemeyer, and J. C. Newman Jr., *Multistage Fatigue Model for an Extruded AZ31 Mg Alloy*, TMS 2008.